

AD-A094 276

ILLINOIS UNIV AT CHICAGO CIRCLE DEPT OF PHYSICS  
TOPOGRAPHIC EXAMINATION OF SEMICONDUCTOR SYSTEMS, (U)

NOV 80 S SUNDARAM, P M RACCAH

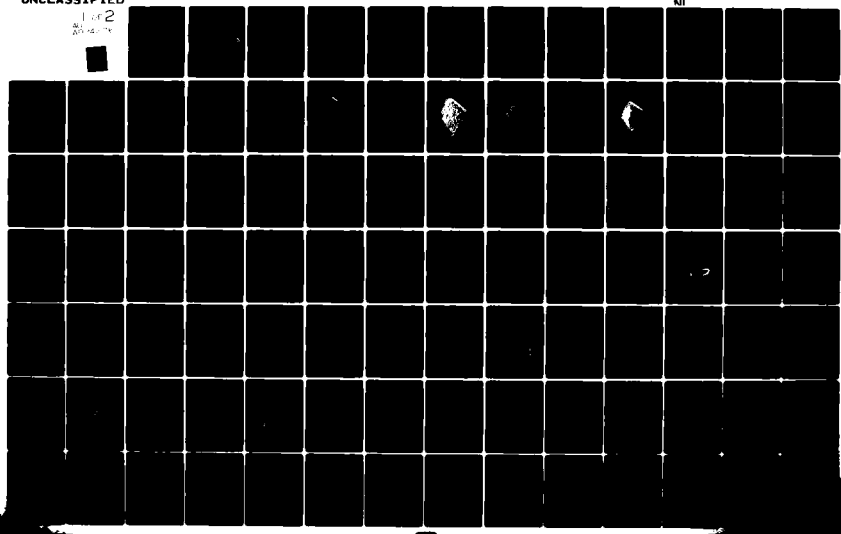
F/G 20/12

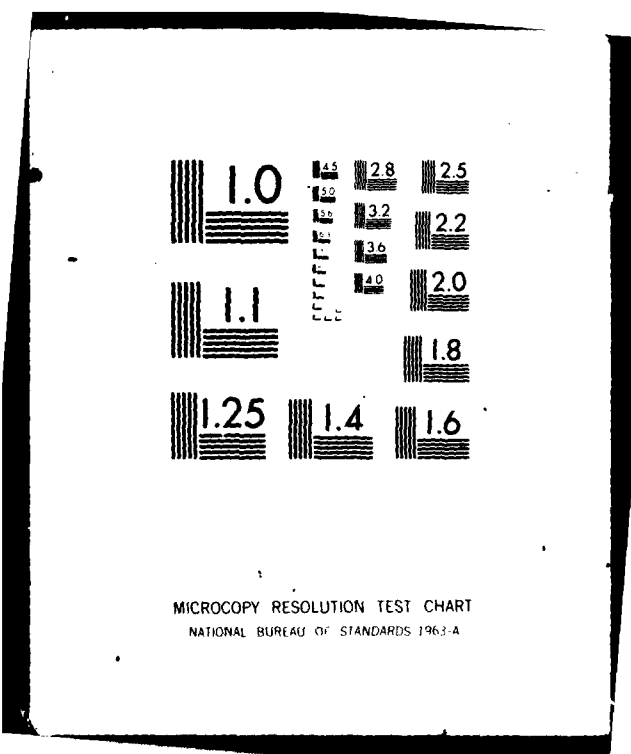
N00014-79-C-8n9

MI

UNCLASSIFIED

1 of 2  
20-14-79





AD A094276

LEVEL

①

TOPOGRAPHIC EXAMINATION OF SEMICONDUCTOR SYSTEMS

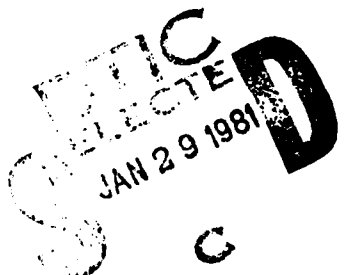
⑩ S. Sundaram  
P.M. Raccah

Department of Physics  
University of Illinois at Chicago Circle  
Chicago, Illinois 60680

⑪ Nov 1980

⑫ 1981

⑨ FINAL TECHNICAL REPORT  
Jun 1978 - Jul 1980



Prepared for

Naval Research Laboratory  
Electronics Material Technology Branch  
Washington, D.C. 20375

FILE COPY

U.S. ONR Contract No. N0001479C0809

⑩

DISTRIBUTION STATEMENT A	
Approved for public release; Distribution Unlimited	

81 1 28 018

1

TOPOGRAPHIC EXAMINATION OF SEMICONDUCTOR SYSTEMS

S. Sundaram  
P.M. Raccah

Department of Physics  
University of Illinois at Chicago Circle  
Chicago, Illinois 60680

November 1980

FINAL TECHNICAL REPORT  
June 1, 1978 - July 30, 1980

DTIC  
SELECTED  
JAN 29 1981

C

Prepared for  
Naval Research Laboratory  
Electronics Material Technology Branch  
Washington, D.C. 20375

U.S. ONR Contract No. N0001479C0809



20 (continued)

materials growth technology program at NRL, the modulation EER technique is shown to be a very unique and sensitive method for the optical characterization of the III-V semiconductors and their alloys.

## CONTENTS

ABSTRACT -----	(i)
INTRODUCTION -----	1
PART I: Topographic Study of Ion Implanted GaAs-----	3
PART II: Effects of Etching on Spectra of Ion Implanted GaAs -----	38
PART III: Topographic Examination of InP and InGaAsP -----	69
PART IV: Modified Schemes for Topographic Studies ---	85
PART V: Conclusions -----	97
ACKNOWLEDGMENTS -----	99
TABLES -----	100
REFERENCES -----	102
CAPTIONS FOR FIGURES -----	103
DISTRIBUTION LIST -----	108

Accession For	
NTIS GRA&I	<input checked="" type="checkbox"/>
DTIC TAB	<input type="checkbox"/>
Unannounced	<input type="checkbox"/>
Justification	
By _____	
Distribution/ _____	
Availability Codes	
Avail and/or	Special
Dist	
A	

## ABSTRACT

Using the techniques of modulation spectroscopy, a systematic investigation and characterization of Gallium Arsenide, Indium Phosphide, and quaternary alloys of InGaAsP have been completed. The effective tool for the topographic examination of implanted materials is the electrolyte electroreflectance (EER) method. The spatial distribution of carrier concentration, the effects of etching, implantation and anneal procedures on the transition energies have been studied. Besides providing the needed "feed back" information for the materials growth technology program at NRL, the modulation EER technique is shown to be a very unique and sensitive method for the optical characterization of the III-V semiconductors and their alloys.

## I. INTRODUCTION

The program described in this final report is part of a large scale and coordinated effort on the growth, processing, and thorough characterization of the III-V semiconductors of GaAs and InP for use in opto-electronic devices. The importance of proper characterization as an aid in materials growth and development of devices is well established. The studies included in this report are with the main objective of providing rapid "feedback" information to the Electronics Materials Technology Branch of the Naval Research Laboratory. Throughout these investigations, there was a very close coordination with the groups at NRL and all the materials except the quaternary alloys were from the above Branch at NRL. The report consists of five major parts dealing with the studies on ion-implanted GaAs, ion-implanted InP, quaternary alloys, and implanted samples of GaAs etched to different depths. The last part includes a brief description of alternative schemes for studying smaller areas of the electronic materials. This final report supplements our previous detailed report about a year ago wherein we have included many of the details of the unique characteristics of the instrumentation developed in our laboratory under this contract. While this report gives the results of our studies in a concise fashion, further information

on any of the specific topics included in this report may be obtained from the investigators. The results outlined in this report have been presented at professional meetings and published in professional journals. The studies on electro-reflectance of ion-implanted GaAs were presented at the meetings of the American Physical Society held in March 1979 and March 1980. The detailed paper covering our studies and the interpretation and explanation of the sensitivity as well as the potential of the modulation technique that we have used is to appear in the Journal of Applied Physics (1981). The studies on InP and the quaternary alloys InGaAsP were presented at the March 1979 meeting of the APS. These results are included in this report.

## PART I

### TOPOGRAPHIC STUDY OF ION IMPLANTED GaAs

In this phase of our studies, a systematic investigation of the electrolyte electroreflectance of GaAs with implanted Be, Se and Si ions has been made. Topographical maps of carrier concentration and of implant dependent modifications of the line-shapes have been obtained. The fluences for the implanted samples ranged from  $\sim 10^{13}$  to  $10^{15}$  ions/cm<sup>2</sup>. Using the  $E_0$  and  $E_1$  peaks, the lineshape variations have been mapped for the low as well as high fluence samples. The evidence suggests that at high fluence the extreme structural damage, resulting from implantation, generates an amorphous layer which upon annealing recrystallizes by a mechanism similar to liquid phase epitaxy. Depending on the fluence of the implant, apparent peak shifts of as much as 80 meV have been observed. These are explained as definitely not due to gross changes in the  $E_1$  and  $E_1 + \Delta_1$  transitions but rather either due to a modification of the simple parabolic band model or due to a definite folding of one of these structures with a third, probably of excitonic origin and analyzed here for the first time. Moreover, the study of GaAs with Be and Se implants proved that electro-reflectance is an unusually sensitive tool for the study and characterization of inversion layers.

## I. INTRODUCTION

Semiconductor properties can be conditioned by ion implantation and the performances thus obtained have great current technological significance. The properties affected include the carrier concentration and velocities as well as interband transition energies. The carrier distribution across the surface of a sample may become non-uniform as a result of the conformation of the implantation beam and the redistribution of the implant after anneal. We present here results for GaAs samples implanted with Be, Se, Si or a combination of Be and Se. The study was performed using low field electrolyte electro-reflectance<sup>1,2</sup> (EER) as it has been shown earlier<sup>3,4</sup> that both the defects density and the way they affect the electron energy band states can very effectively be mapped out with this technique. We have used the  $E_1$  structure (around 2.9 eV) to probe the topography of our samples. The topographic part of our study will be discussed in Section III. It presents evidence for a pseudo liquid phase epitaxy (PLPE) mechanism. The lineshape analysis part of our work is discussed in Section IV and shows the existence of an additional structure, probably of excitonic origin whose behavior is studied here for the first time. This structure varies greatly with implantation and can become folded into the  $E_1$  structure thereby generating considerable lineshape distortions. Finally, new results discussed in Section V illus-

trate the sensitivity of EER spectroscopy to the sign of the minority carriers and show it to be a convenient tool in the study of inversion layers.

## II. METHOD

In this study an electrolyte was used to apply the electric field. The usual experimental arrangement is shown in Fig. 1(a). Since the interface region, across which the electric field is applied, is of the order of microns or less in thickness, the applied voltage need only be 1 to 10 volts in order to generate a field of  $\sim 10^6$  volt/cm<sup>1,4</sup>. In most electrolyte cell arrangements, electric contact is made to the electrolyte by immersing a platinum wire into the bath, while contact to the sample is established by soldering a wire to the rear surface, and insulating, by means of paint or wax, all surfaces except the area to be probed. For completely nondestructive testing the method shown in Fig. 1(b) is preferable. Two separate baths are used, with the sample providing the electrical continuity between the two. A voltage is applied between the two baths, thus resulting in a high electric field across both surfaces of the sample. This technique also ensures that the field is spatially homogeneous across the sample surface. The schematic arrangement of the total system is shown in Fig. 2. The AC and DC components of the detected signal are separated and the ratio taken. This signal (pro-

FIG. 1 (b)

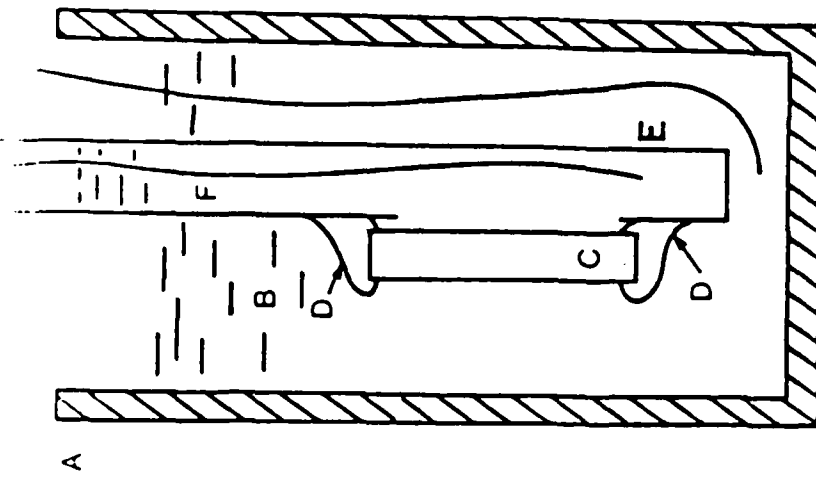
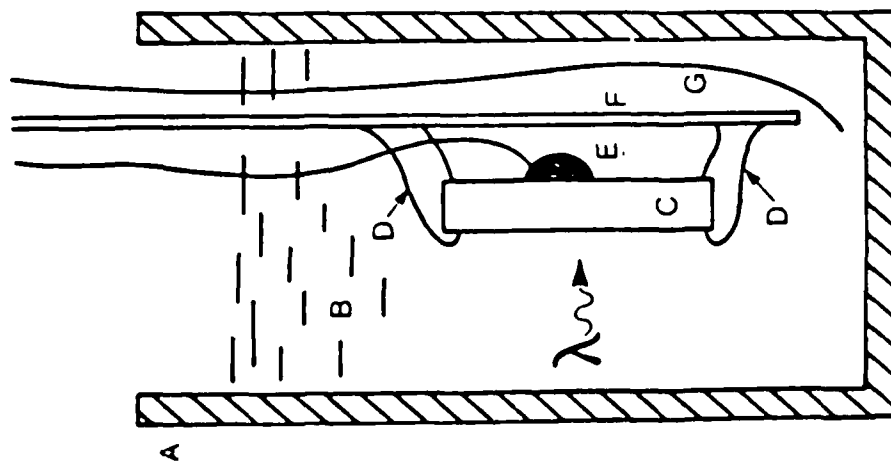


FIG. 1 (a)



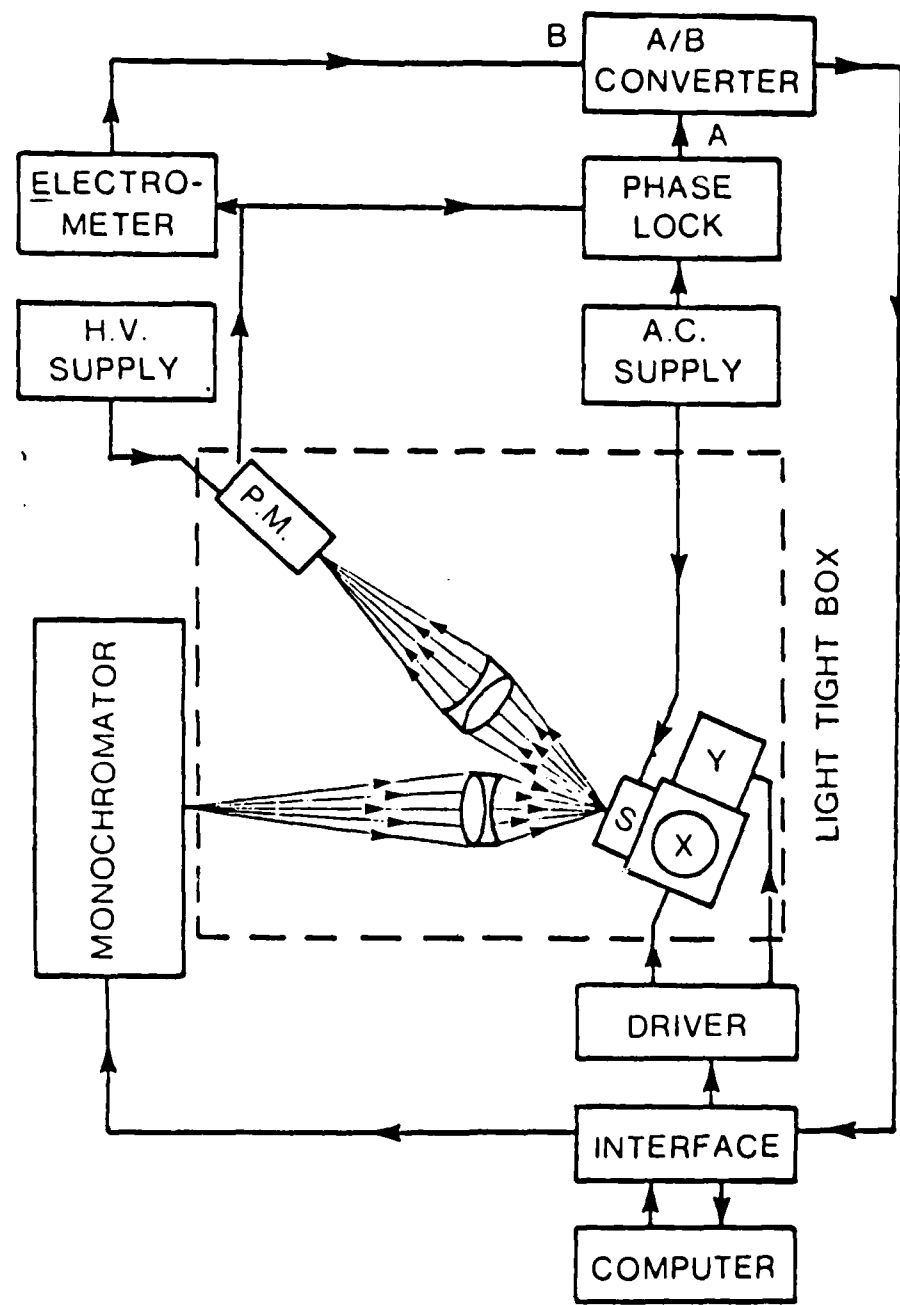


FIG. 2

portional to  $\Delta R/R$ , i.e., the normalized differential reflectance) is converted to digital form and stored. The lineshape of the spectrum thus obtained has the general form

$$\Delta R/R \propto V n L(\lambda, m^* E_g, \dots) \quad (1)$$

where  $V$  is the applied voltage (presumably constant over the area of the sample),  $n$  is the carrier concentration (quite likely to vary over the sample area) and  $L$  is a lineshape function which is dependent on wavelength, effective masses, energy gap, broadening, etc.<sup>2,5</sup> Information obtainable from the lineshape, is of great interest and will be discussed later in this article.

The incident light is focussed to a 100  $\mu\text{m}$  spot on the sample surface. By scanning this spot across the surface it is possible to map  $\Delta R/R$  vs  $(x,y)$  position on the surface. Either the amplitude at fixed wavelength or the wavelength of a selected feature of the spectrum can be mapped out. It is important to point out that the  $\Delta R/R$  signal detected is a property of the bulk electron states. This is because the incident light is reflected by the crystal after having penetrated depths varying from several hundredths of a micron to several microns, depending on the wavelength of the incident light. In the case of GaAs, for example, if the incident light is 4160  $\text{\AA}$ , the depth of penetration is  $0.03\mu$ . For 8660  $\text{\AA}$  light, the depth increases to  $2.25\mu$ .<sup>6</sup> It therefore stands to reason that the electroreflectance signal will depend entirely on bulk states. The surface

conditions play a role mostly because an amorphous layer can form which will result in a weakening of the signal and a broadening of its features. As shown in a theory due to Aspnes,<sup>2</sup> among the various amplitude factors of the lineshape function, one has

$$\frac{\Delta R}{R} = \text{Re} \left[ \frac{1}{(E+i\Gamma)^2} \int_0^\infty dz e^{-2ikz} \frac{\xi(z)^2}{\xi(0)} \dots \right] \quad (2)$$

where  $k$  is the optical absorption index,  $z$  is the axis normal to the surface of the sample, and  $\xi(z)$  is the applied electric field as a function of depth (surface at  $z = 0$ ). The integral restricts the volume of the sample that is probed by electro-reflectance. The surface treatment then changes the results in that a semi-amorphous layer may be formed which will affect both  $\Gamma$  and the extent of the electric field. Therefore, the amplitude will be reduced by both the  $1/(E+i\Gamma)^2$  factor and the field factor in Eq.(2). In fact, if the amorphous layer is sufficiently thick the signal might simply be unobservable. This turns out to be the case of certain implanted and unannealed materials. In addition, increasing  $\Gamma$  will also directly increase the spacing of the EER peaks.<sup>5</sup>

### III TOPOGRAPHIC STUDIES

The characteristics of all the samples on which we are reporting here are listed in Table I. The substrates used for

the samples in this study were semi-insulating (100) GaAs and the implantations were done at room temperature. Scanned beams of 100 keV were used for Be, 400 keV for Se, and 170 keV for Si implantations to fluences ranging from  $5 \times 10^{12} \text{ cm}^{-2}$  to  $1 \times 10^{15} \text{ cm}^{-2}$ . The samples with Be implant were encapsulated with pyrolytically deposited  $\text{SiO}_2$  and annealed at  $800^\circ\text{C}$  for 30 minutes. The ones with Se and Si implants were encapsulated with plasma-deposited  $\text{Si}_3\text{N}_4$  and annealed for 30 minutes at  $850^\circ\text{C}$  and  $800^\circ\text{C}$  respectively. The samples were all annealed in flowing gas environment. Figure 3 is a graph of the  $E_1$  spectrum of an unimplanted sample (5-9L) and an implanted sample (2185). The unimplanted sample exhibits the well known structure reported in the literature<sup>1</sup> while the implanted sample (Be at a fluence of  $10^{15}$  ions/cm) shows a shift of the structure. In that sample, the  $E_1$  (2) peak (which is tabulated in Table II for all of the samples) exhibits an apparent shift of 80 meV towards the high energies. This interesting shift turns out to decrease with lower implantation fluences. Furthermore, in the samples which were implanted with low fluences, the shift varies from place to place on the sample. It must be noted, however, that this does not necessarily point to a spatial dependence of the band gap energies, as the lineshape may be modified by other effects. In Fig. 4 we show a plot of the magnitude of  $\Delta R/R$  vs  $(x,y)$

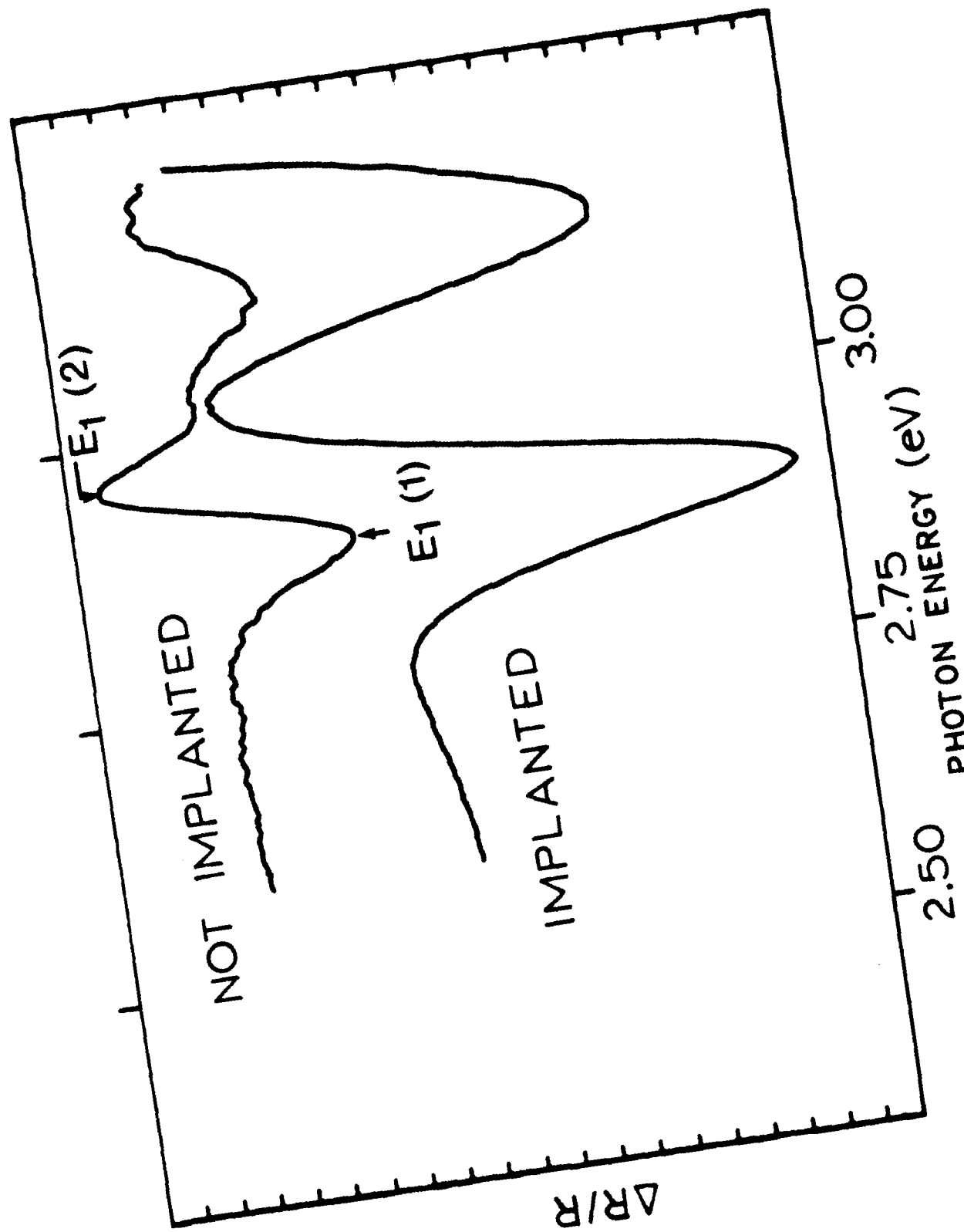


FIG. 3

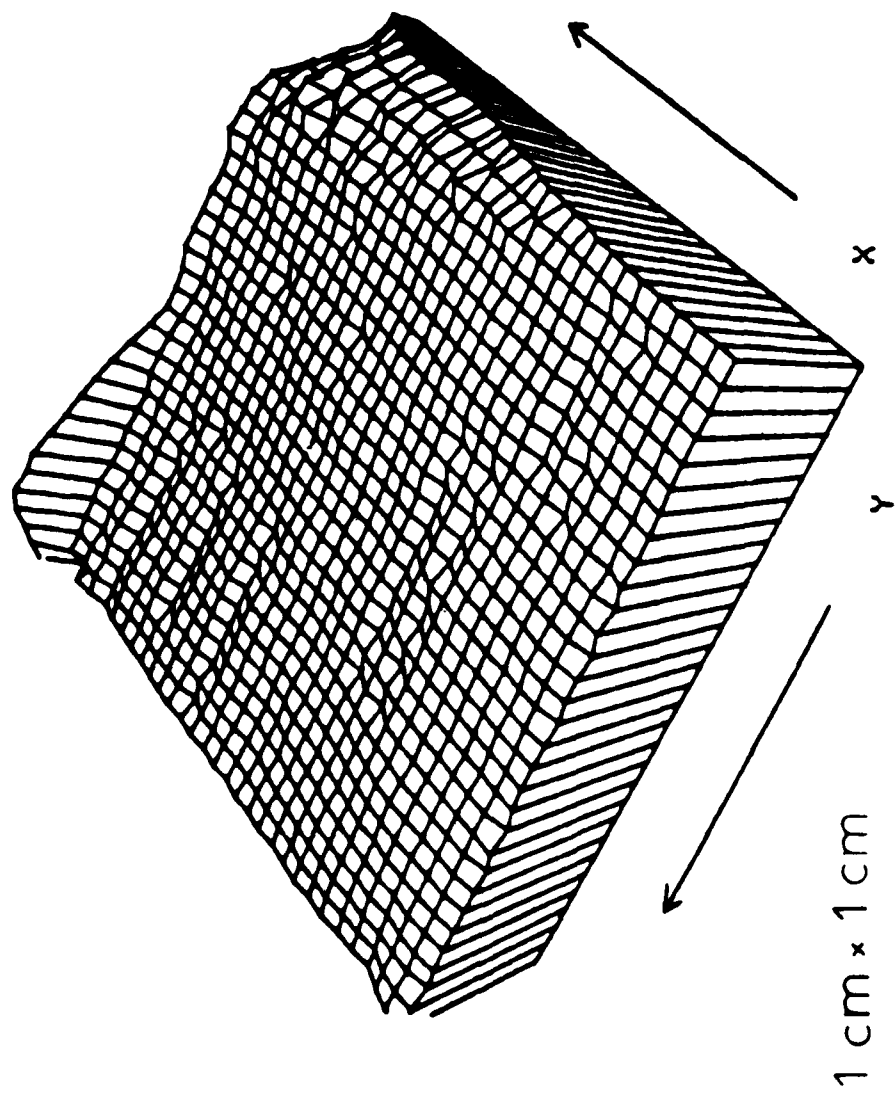


FIG. 4

coordinates on the sample surface, for the unimplanted sample (5-9L). As can be seen the topography is lacking strong features. The slight rise from one edge is most likely due to the usual variations in doping which generally follow the Czochralsky whirls thereby more or less mapping out the stress fields generated during growth. In contrast, as seen in Fig. 5, the topography for sample 2186 (with Be at  $2 \times 10^{14} \text{ cm}^{-2}$  fluence) is extremely rough. Clearly in such a case the irregularities do not result solely from variations in the carrier concentration. When the lineshape function  $L(\lambda, E_g, \dots)$  is conserved from place to place on the sample, the scans of  $\Delta R/R(x,y)$  can be performed at a fixed wavelength corresponding to a peak in the electro-reflectance spectrum and then fairly reflect variations in carriers concentration. However, in sample 2186, the electronic mechanisms evidently have a topographic  $(x,y)$  dependence thus inducing an  $(x,y)$  dependence of the lineshape function  $L(\lambda, E_g, \dots)$ . A much more meaningful test, under these circumstances, is to plot the energy position of a selected part of the spectrum at a given energy  $E$  vs  $(x,y)$ .<sup>3</sup> It was convenient, for automation purposes, to use a zero crossing, specifically the one between the  $E_1(1)$  and  $E_1(2)$  peaks, for this test. Figure 6 displays the results obtained for sample 2186.

In this case as in all others the variations in  $E(x,y)$

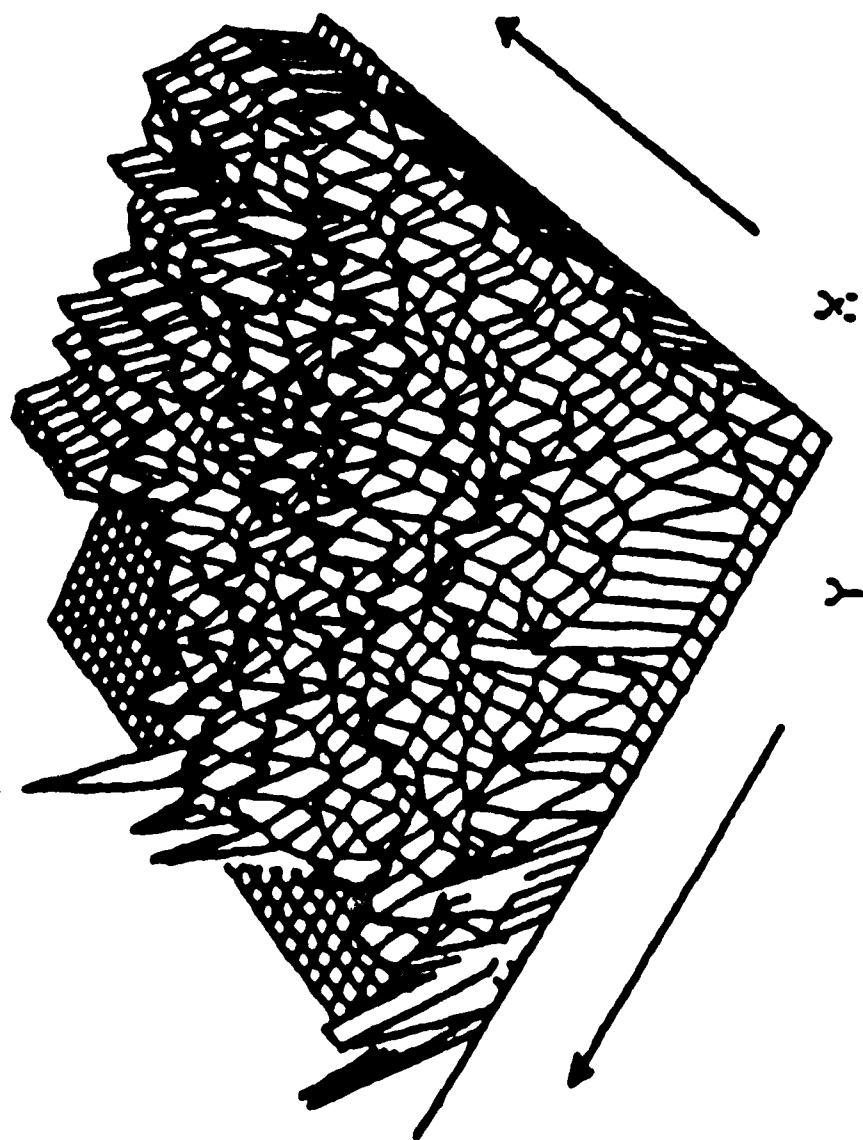


FIG. 5

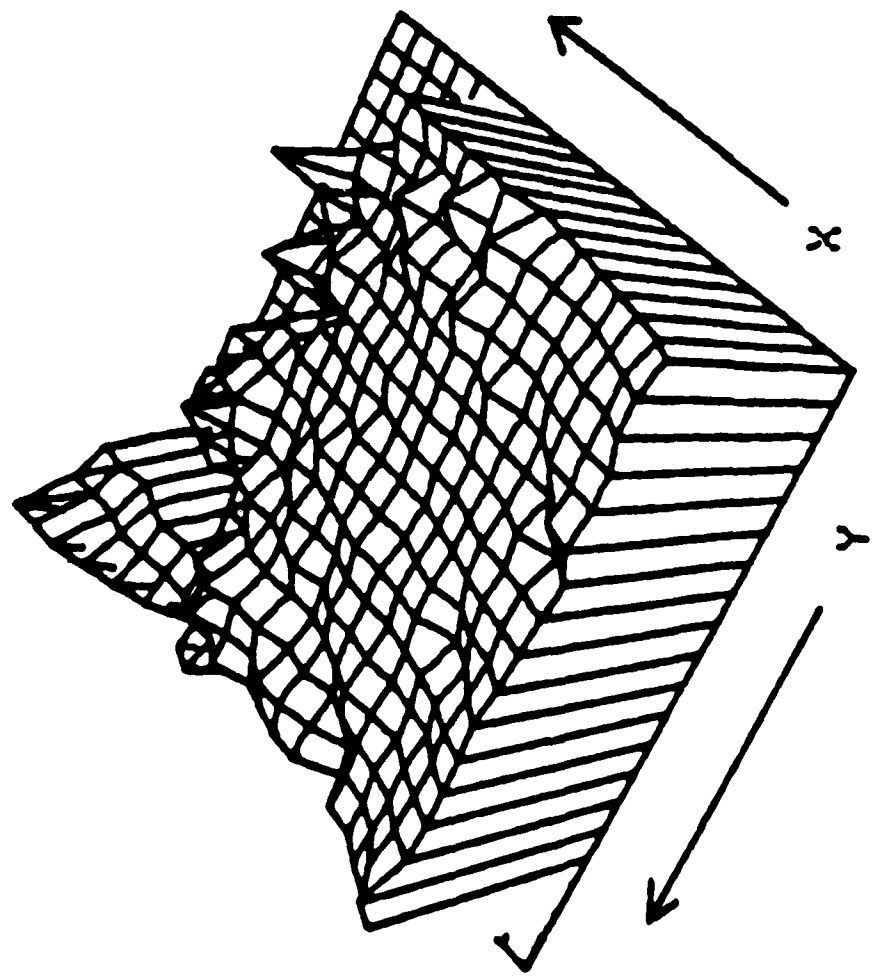


FIG. 6

were found to increase with decreasing implant fluence, while the largest shifts, with respect to the spectra reported in the literature, occurred for the larger fluences. For example, sample 2186 (fluence of  $2 \times 10^{14} \text{ cm}^{-2}$ ) with a maximum shift of +30 meV for the  $E_1(2)$  peak, has considerable (x,y) variation, whereas as shown in Fig. 7 sample 2185 ( $10^{15} \text{ cm}^{-2}$  fluence) with its large shift of +80 meV exhibits almost no (x,y) variation. Moreover, within the same sample the larger the energy variation the quieter the topographic landscape, as seen in Fig. 6.

These observations raise two questions.

- 1) Whether these effects are solely due to unannealed lattice damage as seems commonly believed or whether they are due to other causes;
- 2) Whether the apparent  $E_1(2)$  energy shifts are real.

In order to resolve the first question, two molecular beam epitaxy (MBE) grown samples of GaAs:Be were examined. In both of these samples, large positive shifts of the  $E_1(2)$  peak were observed. Since MBE grown samples are fairly free of lattice damage it is clear that the analogous changes observed in the  $E_1$  spectrum of Be implanted samples cannot be due to it. It would seem that the shifts have rather similar causes to those observed earlier on samples with various doping concen-

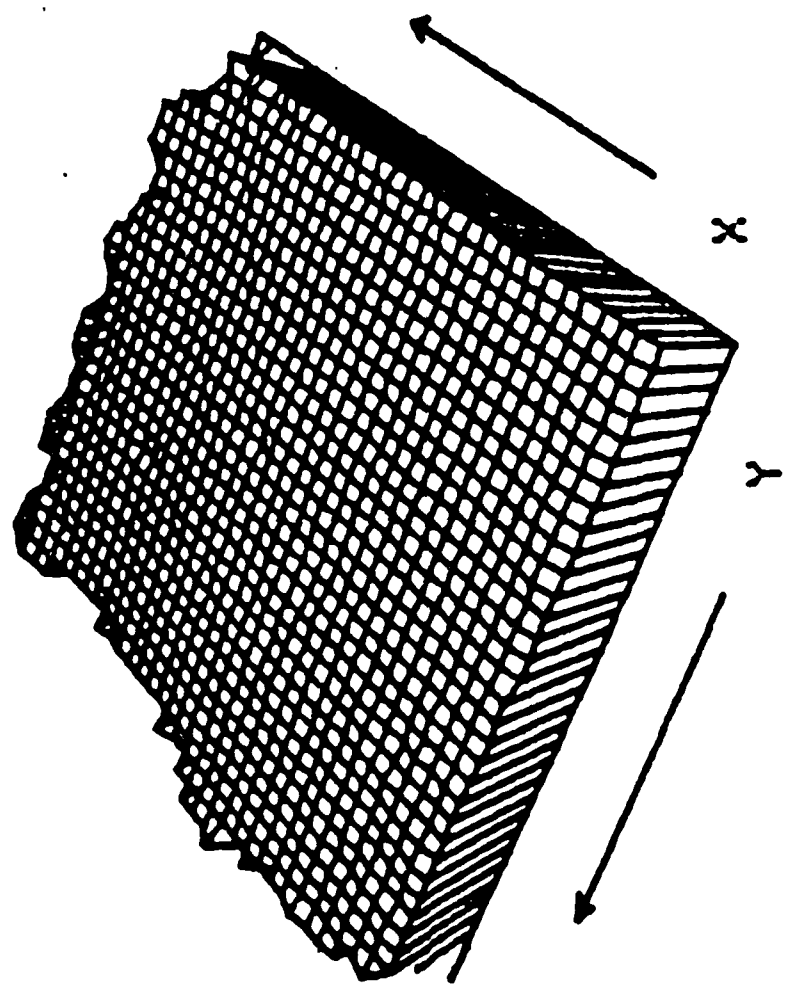


FIG. 7

trations.<sup>4</sup> In effect they result from impurity modifications of the band structure.

Generally, it appears that if the lattice is allowed to be mechanically damaged to any great extent, the electro-reflectance signal rapidly becomes unobservable due to reductions in amplitude. This was borne out by the absence of signals from either Ar bombarded or Se or Be implanted samples that were unannealed. In one case, however, that of a very low fluence ( $10^{13} \text{ cm}^{-2}$ ) Be implanted unannealed GaAs sample we did obtain a signal, and could compare it to that of an identical annealed sample. These two samples are designated 9127G and 9127F respectively and their spectra are displayed in Fig. 8. Note that the unannealed sample had a response magnitude which is 1/20 of that of the annealed sample. There are appreciable lineshape changes but the energy shifts are similar ( $\sim 20$  meV). Virgin substrate material from the same crystal from which the above two samples were cut, was also examined and the observed peaks were in agreement with those reported in the literature.<sup>1</sup> This further confirms that the observed shifts are due to impurity effects rather than to unrecovered mechanical damage. A plausible interpretation of our results appears to be the following.

The process of implantation and the resulting distribution of ions give rise to an amorphous layer (on a single

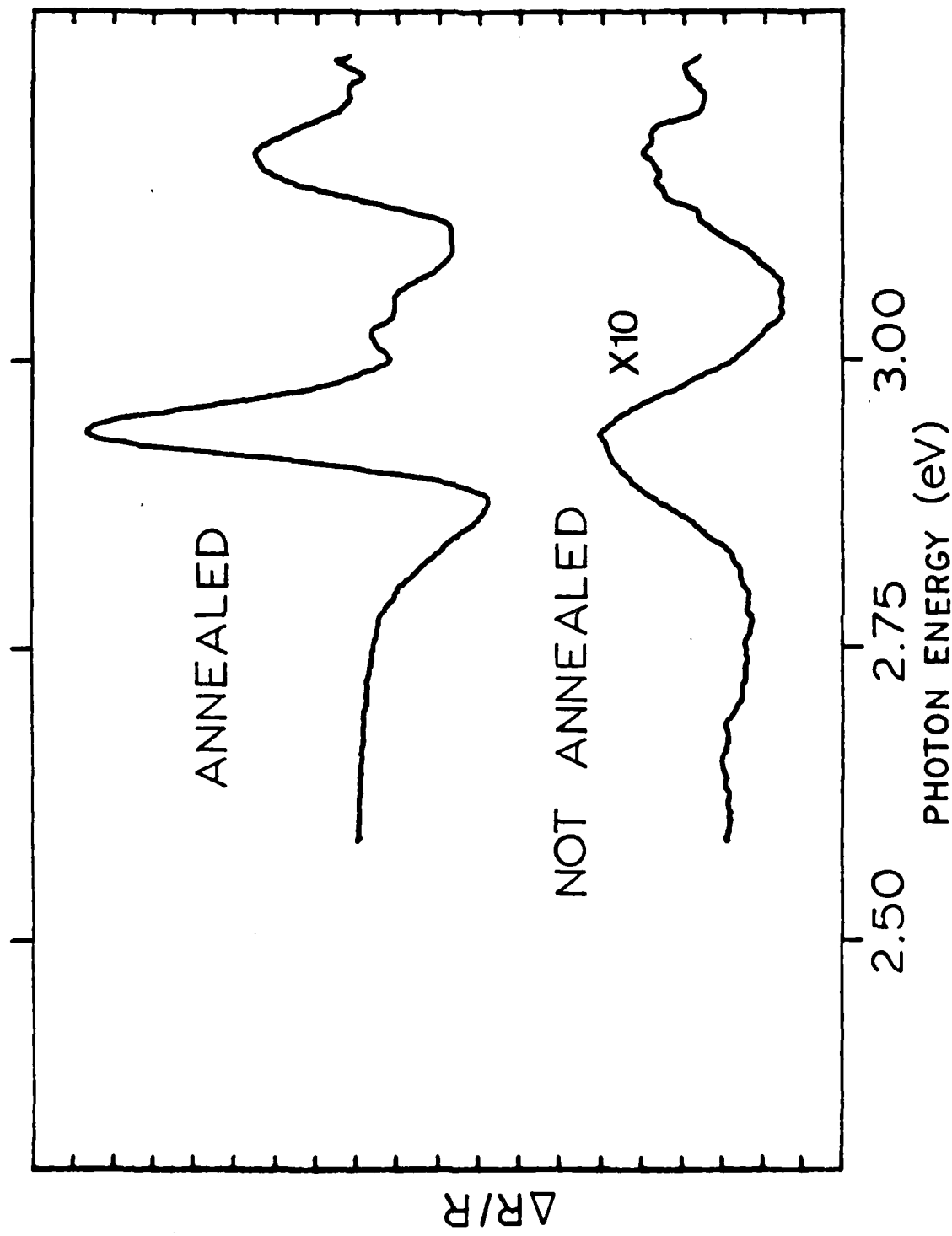


FIG. 8

crystal substrate) whose depth or thickness depends, among other factors, on the beam energy, the mass of the implanted ions, etc. The post-implantation anneal converts this amorphous layer, via the recrystallization process, into a crystalline layer on the undisturbed substrate. Since the beam penetration does not vary greatly with fluence, the greater the fluence the more amorphous the implanted layer and the cleaner the interface with the rest of the crystal. At low fluences the implanted layer is not so much amorphous as it is fractured and the interface to the rest of the crystal is very rough. (Hence the inverse relation between uniformity and fluence, which we have observed.) In a sense, the epitaxial layer thus generated results from pseudo liquid-phase-epitaxy. It has been pointed out to us<sup>8</sup> that there appears to be no evidence for solid state recrystallization in GaAs and these results may be the first indication that such a process is possible. Certainly further study would be necessary to ascertain such a possibility. In situ electroreflectance during anneal would be an ideal approach. The low field electroreflectance from such a "pseudo LPE layer" (when fully annealed) exhibits noticeable changes in lineshapes and apparent shifts in the positions of the optical transition energies. Anderson, Douglas, and Park have reported<sup>7</sup> that for samples annealed at lower temperatures (400 - 600°C) than usual ( $\sim 800^\circ$ ) the

electroreflectance lineshape is insensitive to impurity type or to fluence and actually reflects mechanical damage. In definite contrast, our studies of fully annealed samples have established that the changes in the EER spectra are determined by the nature of the impurity ions as well as by the beam fluence used.

#### IV LINESHAPE ANALYSIS

Turning now our attention to the second question, we list in Table I actual data on GaAs samples that were implanted with Si and with Se. The observed shifts in the  $E_1(2)$  peak are all of the same order as in the samples discussed above. To our knowledge there is currently no clear interpretation for these apparent energy shifts (or lineshape modifications) or for comparable ones previously reported in the literature.<sup>4</sup> What is intriguing is the fact that we are not dealing here with the direct gap but with higher order interband transitions for which such mechanisms as the Burstein shift or impurities band tailing cannot be invoked. This leaves excitonic effects as a possibility and indeed such effects were postulated recently in order to explain the stress dependence of the  $E_1$  transition in GaAs. Given the impurity induced distortion in the low field electroreflectance spectrum of ion-implanted GaAs as a full lineshape analysis imposed itself in order to investigate the possi-

bility of excitonic mechanisms and determine accurately the effects of implantation on interband transition energies, broadening factors, etc.

The third derivative lineshape model<sup>2,9</sup> due to D.E. Aspnes is appropriate to describe low field electroreflectance spectra and was used here. Its derivation is rather complex but Aspnes<sup>2</sup> has shown that one can arrive at a relatively simple expression describing the electroreflectance spectra of a single interband transition:

$$\frac{\Delta R}{R} = C \operatorname{Re} e^{i\theta} (E - E_g + i\Gamma)^{-n} \quad (3)$$

where  $E$  is the incident photon energy,  $E_g$  is the interband transition energy,  $\Gamma$  is the joint band width,  $C$  and  $\theta$  are amplitude and phase factors which are only weakly dependent on  $E$ , and  $n$  is an exponent determined by the dimensionality of the critical point involved.

The data obtained from an unimplanted sample was used to determine  $\theta$  and  $n$ .  $\theta$  turned out to be small and have little influence on the overall fit but it was maintained in subsequent fits because of its finite statistical significance. As for  $n$ , the dimensionality of the critical point involved in the  $E_1$  transition imposed a value of 3 for which we did get the best fit to our data. In our fits to experimental results obtained from all other samples  $n$  and  $\theta$  were fixed to these values while  $E_g$

and  $\Gamma$  were allowed vary.

We have shown in Fig. 9 a comparison of the optimal lineshape with the data. Since there are two interband transitions,  $E_1$  and  $E_1 + \Delta_1$  two lineshapes  $L_1$  and  $L_\Delta$  were used. As can be seen, the fit is rather good everywhere except around 3.05 eV where a clear feature of the experimental spectra cannot be accounted for. Since this feature subsists at very low applied electric field, it cannot be subsidiary Franz-Keldysh oscillation. At these energies it might very well be due to an exciton. Previous reports<sup>10,11</sup> have indicated the existence of a room temperature excitonic contribution to the  $E_1$  and  $E_1 + \Delta_1$  structures, but it appears probable that these are unrelated to the feature (which will hereafter be designated as  $L_3$ ) discussed here.

In order to account for this additional structure, we tried to add a lineshape and set  $n$  equal to 2, as suggested by Aspnes for an excitonic contribution, but our data turned out to be more amenable to fitting by a simple Lorentzian derivative. The calculated lineshape is compared to the data in Fig. 10 and one can see that the fit is excellent.

Just as good an agreement was obtained with a sample which was implanted with Se at low fluence ( $5 \times 10^{12}$  ions/cm<sup>2</sup>). This type of implantation induces a change in the sign of the carriers and the sample was n-type. As expected, the  $E_1$  and

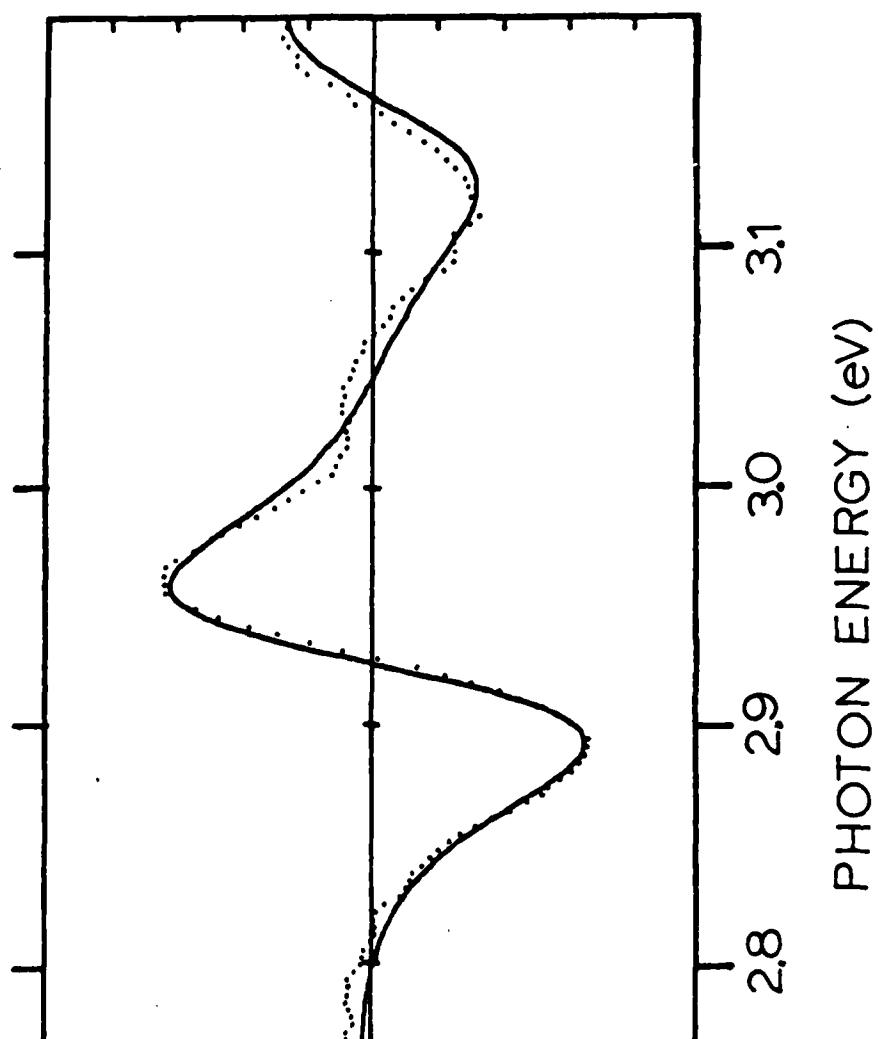


FIG. 9

$\Delta R/R$

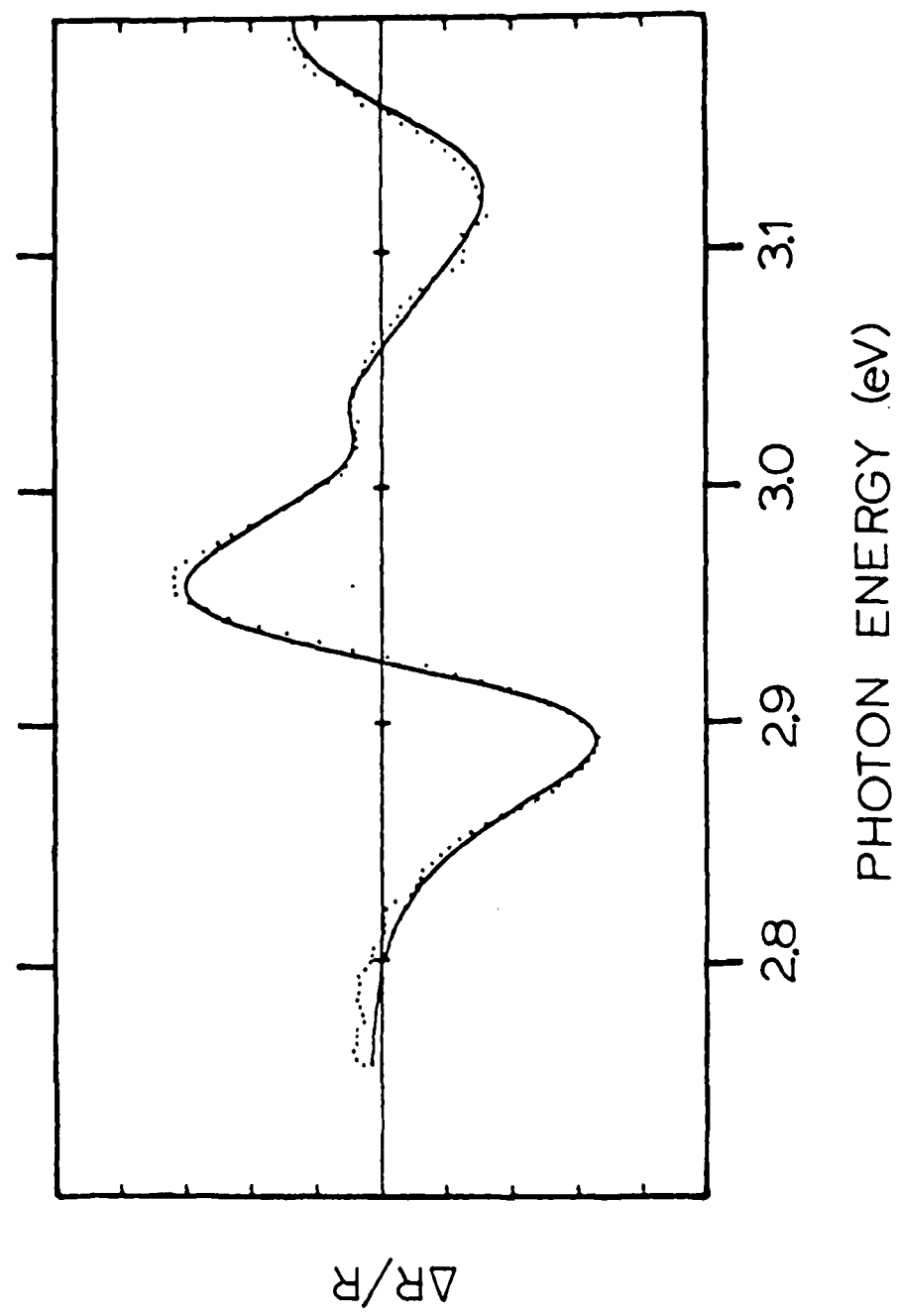


FIG. 10

$E_1 + \Delta_1$  structures in Fig. 11 are inverted with respect to their homologs in Fig. 10. Most significantly, however, the  $L_3$  is not inverted. This can easily be verified by comparing Figs. 12 and 13 in both of which the  $E_1$  and  $E_1 + \Delta_1$  structures only have been fitted. The  $L_3$  contribution to the experimental data then stands out and can clearly be seen to have the same phase in both samples. In other words, the  $L_3$  lineshape is independent from the sign of the carriers which is certainly consistent with it being associated with a quasi particle having no net charge such as an exciton.

In samples implanted with higher ion concentrations  $L_3$  starts overlapping with  $E_1$  and no longer stands out. Importantly, however, it was not possible to obtain the best fit to the data without the additional  $L_3$  lineshape even though it cannot be resolved. Since one can always obtain a better fit by adding parameters, we are listing in Table II the standard deviations along with the values of each of these individual parameters. As can be seen, they all have a convincing statistical significance. Such an interpretation is of necessity very preliminary. Conceivably, there may even be no additional structure. Our inability to fit the lineshape in the region between  $E_1$  and  $E_1 + \Delta_1$  may simply be due to a breakdown of the parabolic band approximation upon which the model we are using is based. Some of the results have been plotted versus carrier concentration in

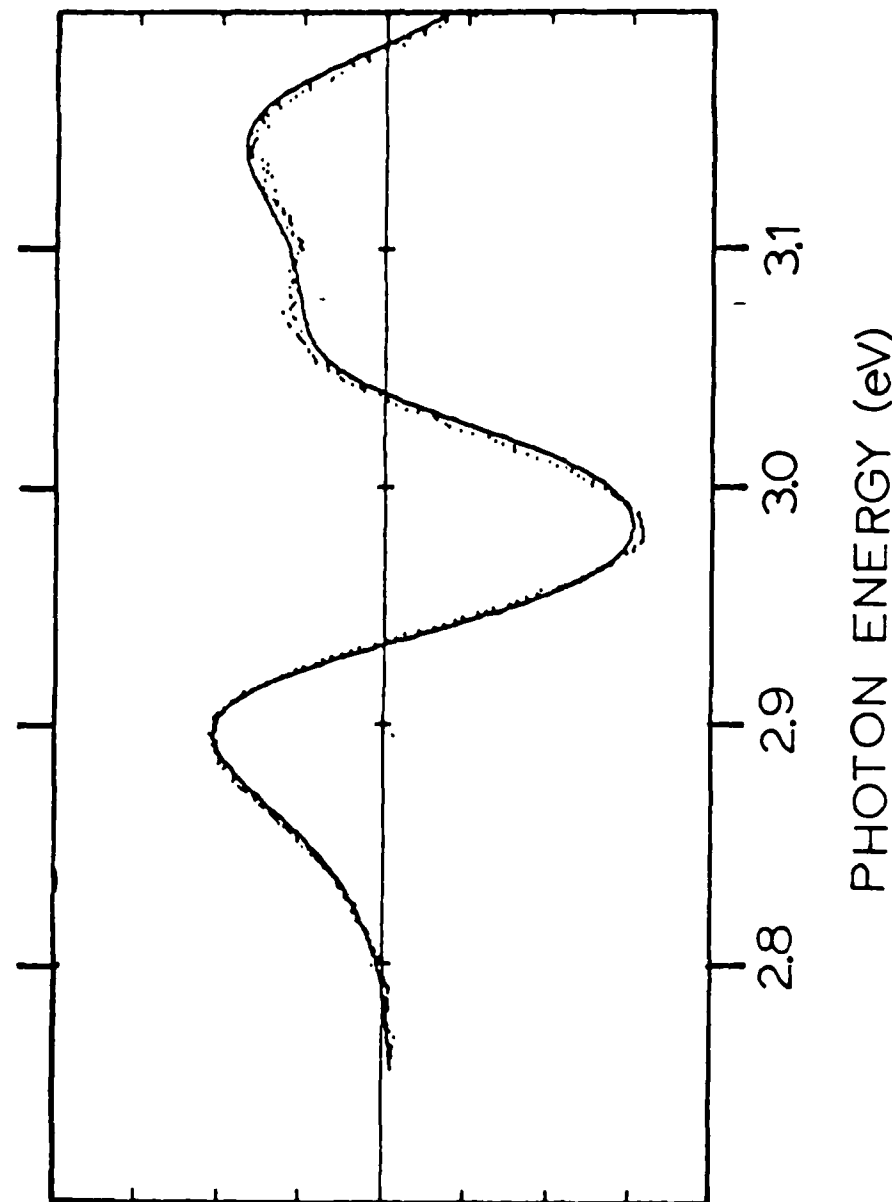


FIG. 11

$\Delta R/R$

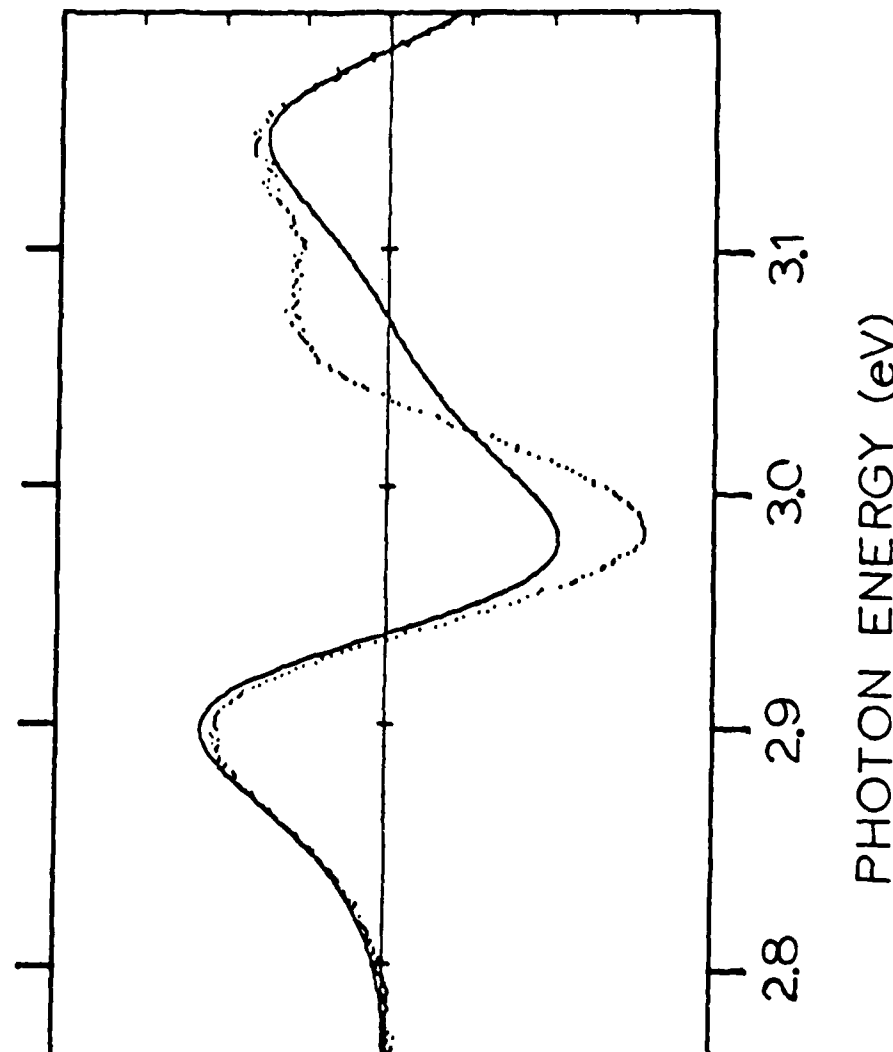


FIG. 12

$\Delta R/R$

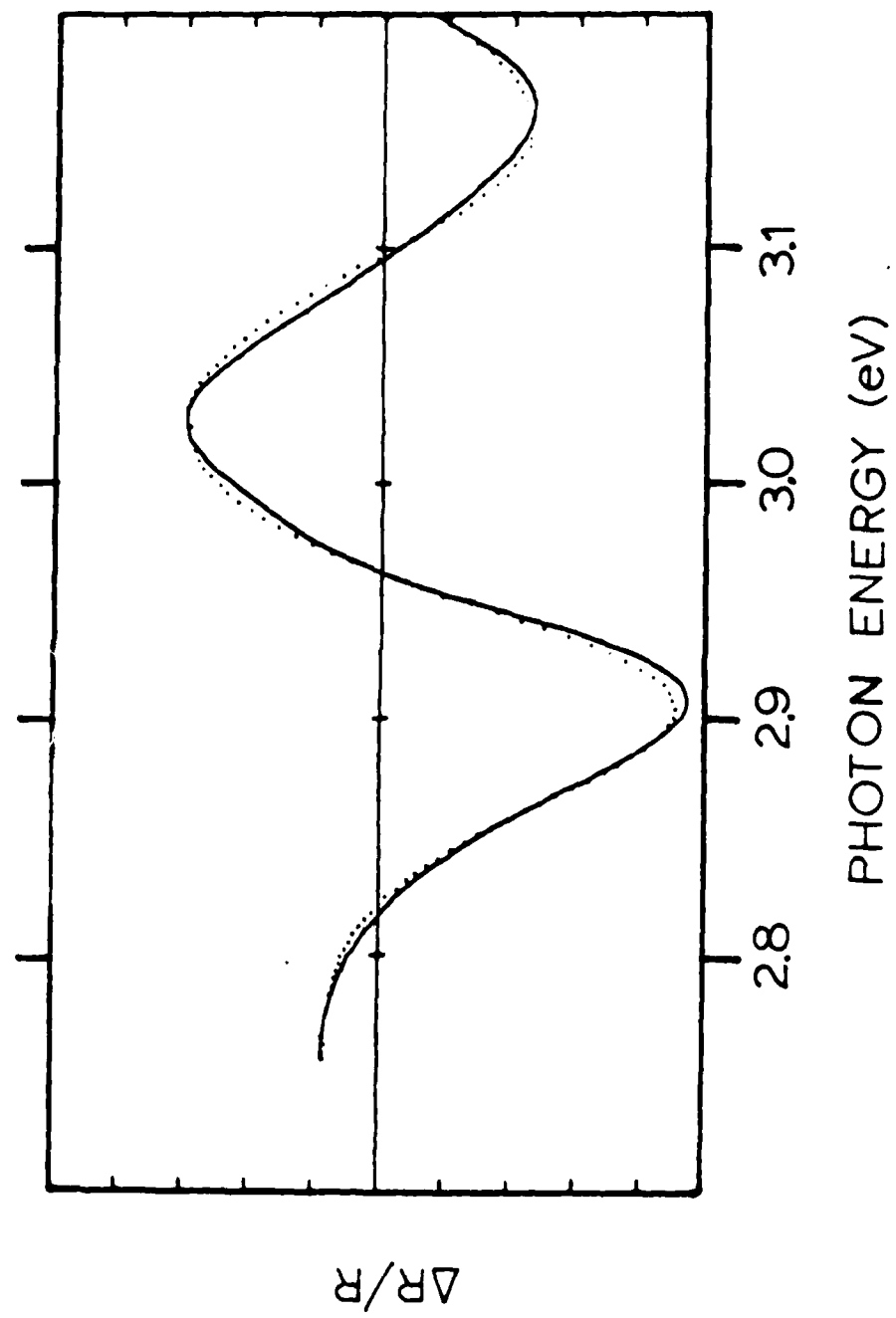


FIG. 13

Fig. 14.

The results in Table II and Fig. 14 show that the  $E_1$  and  $E_1 + \Delta_1$  interband transition energies vary little as compared to the changes in the  $E_1(2)$  peak, which indicates that most of the overall lineshape changes are due to overlap of the  $E_1$  with the  $L_3$  structure. Nonetheless, these changes, while small ( $\sim 20$  meV), are real (the bars do not represent errors but the broadening parameter  $\Gamma$ ) and deserve some consideration. The results reported in the first sections clearly show that mechanical damage incurred during implantation and unrecovered by anneal cannot be invoked as a cause for the observed energy shifts. This is confirmed here by the fact that the  $\Gamma$ 's do not change significantly as they would for mechanical damage. The remaining possibility is that these real energy shifts result from lattice deformations around substitutional impurities. A cluster calculation could verify this assumption and would be quite interesting.

Turning now our attention to the  $L_3$  structure, one can see in Fig. 14 that its energy first mirrors the changes in  $E_1$  and  $E_1 + \Delta_1$  but then rapidly falls off and broadens. We believe that this may be due to free electron screening to which the assumed exciton should be quite sensitive. A study of the stress dependence of  $L_3$  would do much to inform us on its origin and symmetry and this is under way.

#### V INVERSION STUDY

Another interesting result of this investigation is that

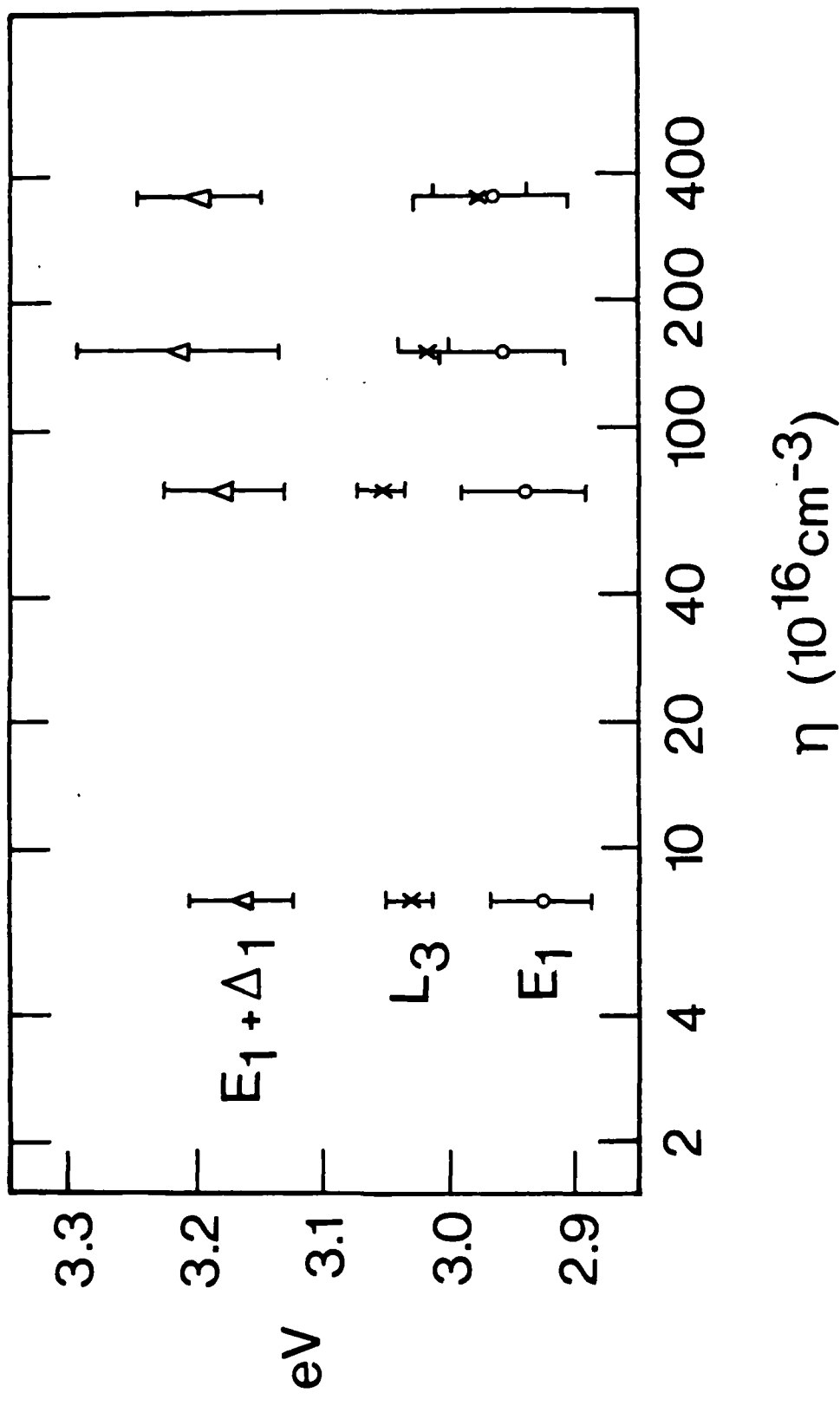


FIG. 14

in certain samples evidence was found that indicates that the inhomogeneity of the implantation had resulted in the formation of p-n junctions in the sample. The power of the electro-reflectance technique to characterize the presence of such configurations is a feature of significance for device development. This effect was observed in only two of the series of samples in the present studies. The first of these was the unannealed sample with  $10^{13} \text{ cm}^{-2}$  Be implant. The  $\Delta R/R(x,y)$  surface of this sample is shown in Fig. 15. The shape is crater like, with a center where the phase of the  $\Delta R/R$  signal is the inverse of the phase of the edges. Fig. 16 illustrates the effect further. Here are shown three traces, taken from points only 0.75 mm apart along the surface of the sample. Since these traces were taken at points of low electroreflectance amplitude, the S/N ratio is small. Nevertheless, the phase inversion noticed as the examined region is moved toward the center of the sample is dramatically clear for the  $E_1$  spectrum. This is not observed in the corresponding annealed sample and so the effect is undoubtedly due to a macroscopic clustering of the Be which is normally smoothed out by annealing.

A similar effect can also be observed as a function of depth. As mentioned earlier, the incident light will penetrate  $0.3 \mu$  into the sample for wavelengths corresponding to the  $E_1$

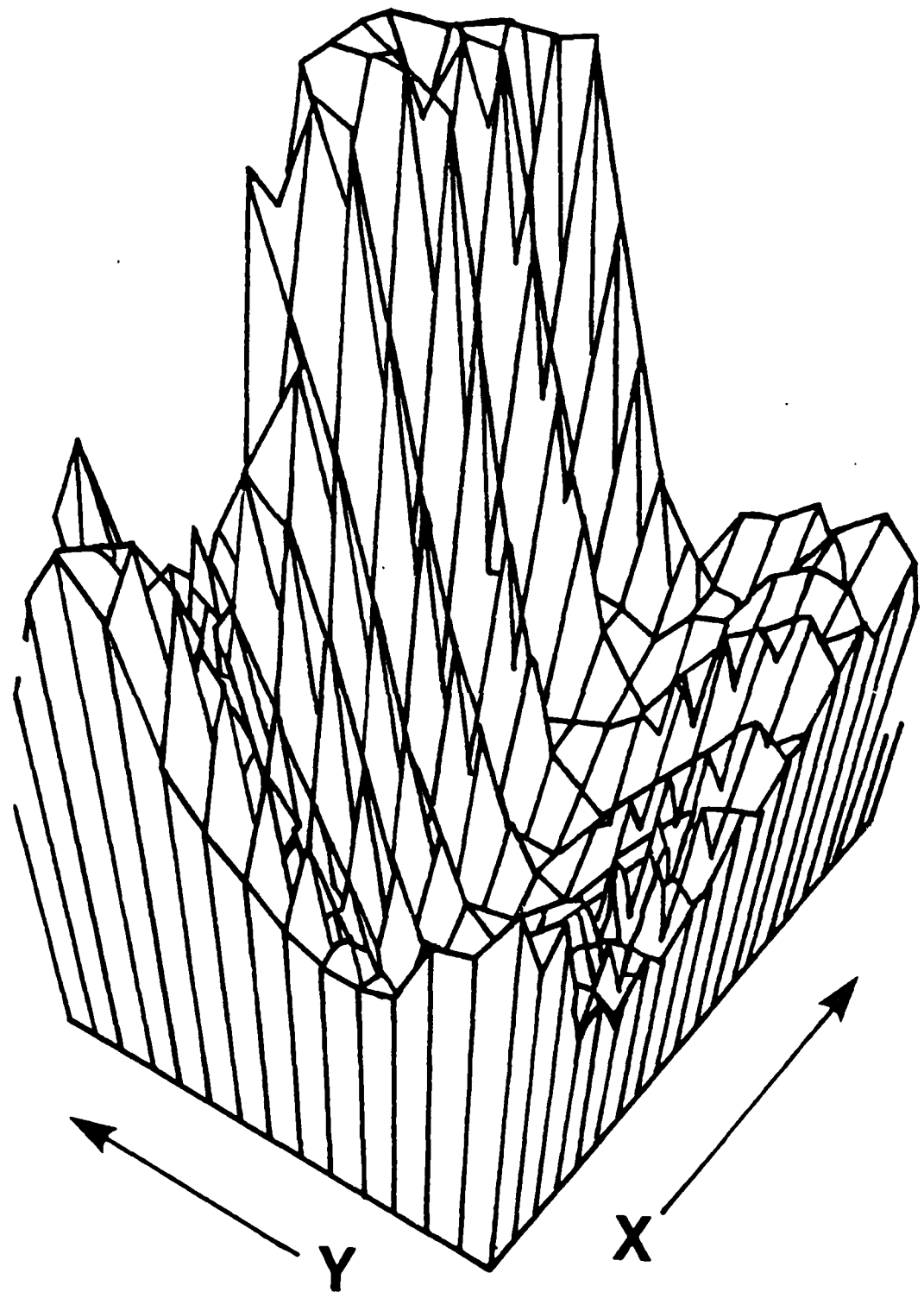


FIG. 15

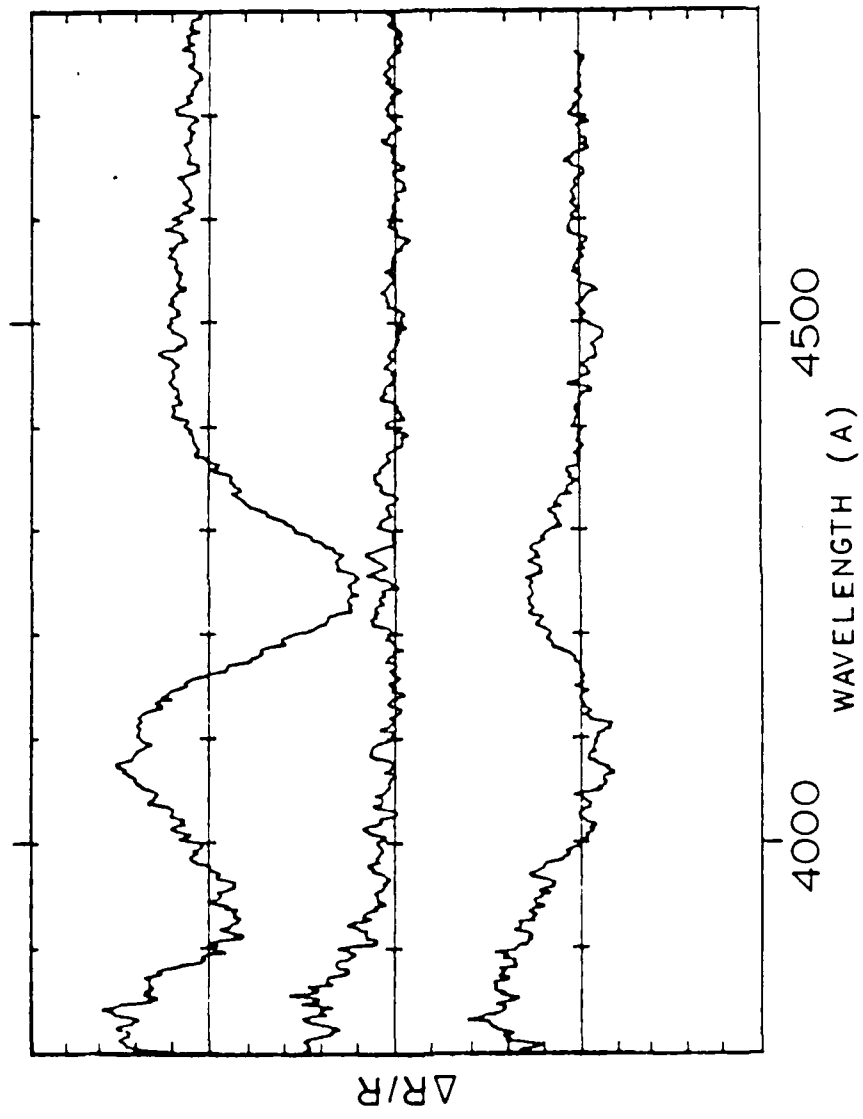


FIG. 16

transition and will penetrate  $2.25 \mu$  for wavelengths corresponding to the  $E_0$  transition. This range of depths corresponds to the distribution in depth of the Be ions after annealing.<sup>12</sup> A GaAs sample which was implanted with  $5 \times 10^{12} \text{ cm}^{-2}$  of the acceptor Be and  $1 \times 10^{13} \text{ cm}^{-2}$  of the donor Se has been investigated. This sample was annealed so that the more mobile Be ions (being less massive than the Se) were distributed closer to the surface. A continuous trace was made of the spectrum covering both the  $E_1$  and  $E_G$  energies. When compared to unimplanted GaAs (as in Fig. 17) it is found that the phase of the  $E_0$  signal is inverted from that of the  $E_1$ . Therefore, the existence of a p-n junction with depth has been inferred.

#### VI SUMMARY

We have shown that the effects of implantation are strongly related to implantation energy when annealing is complete and procedures are kept constant. This is probably because of a pseudo liquid phase epitaxy effect.

It would appear as if it is possible to measure quantitatively the potential modifications resulting from lattice relaxations around the substitutional impurities. A cluster calculation would be most useful to further our understanding of these results.

The apparent peak energy shifts in the low field electro-reflectance spectra, which have been observed earlier<sup>4</sup> in highly

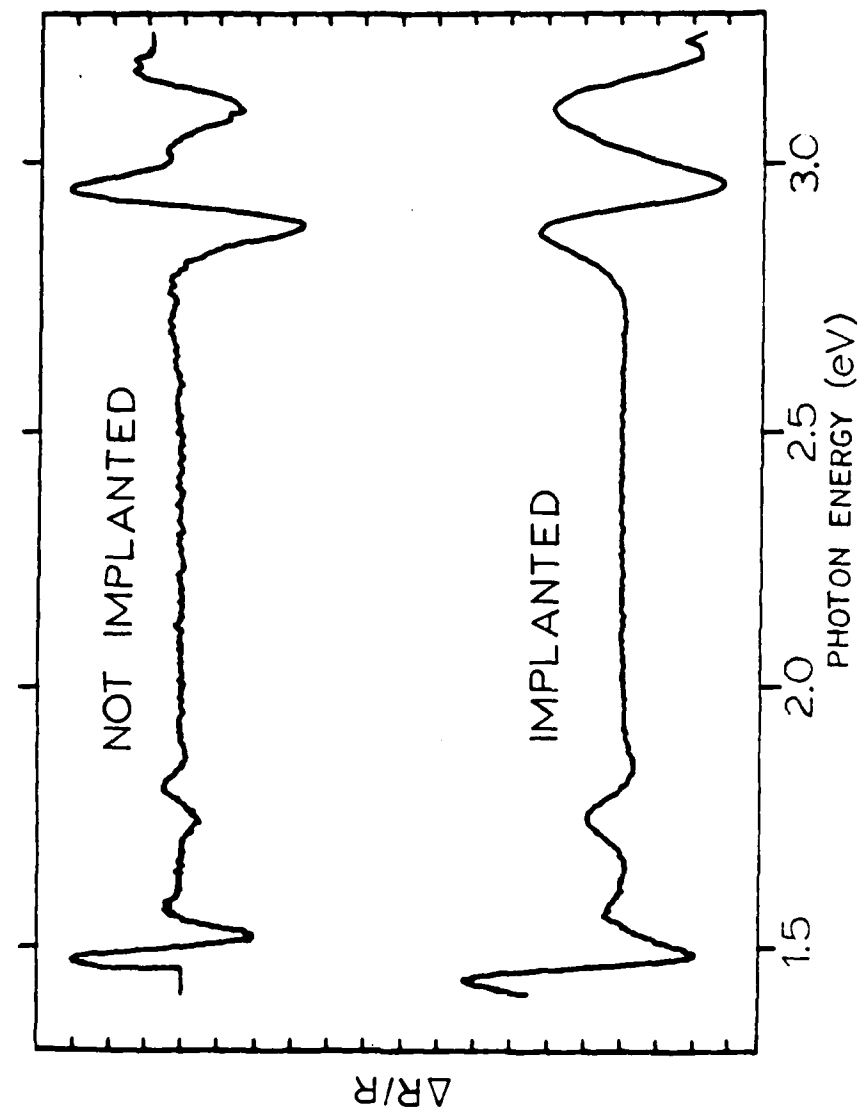


FIG. 17

doped GaAs, but were unexplained, turned out to be mostly due to folding of the  $E_1$  structure with a sharp structure ( $L_3$ ) which appears excitonic in nature (Shifts in the  $E_0$  structure can be explained differently as discussed earlier<sup>4</sup>). A systematic study of the effects of uniaxial stress on  $L_3$  is under way and should inform us on the symmetry of that assumed excitonic state as well as on its cause.

The sensitivity of the phase of the electroreflectance spectra to the sign of the minority carriers made it very easy to recognize the transition from a p to a n zone laterally or in depth. This result could be most useful in exploring inversion layers.

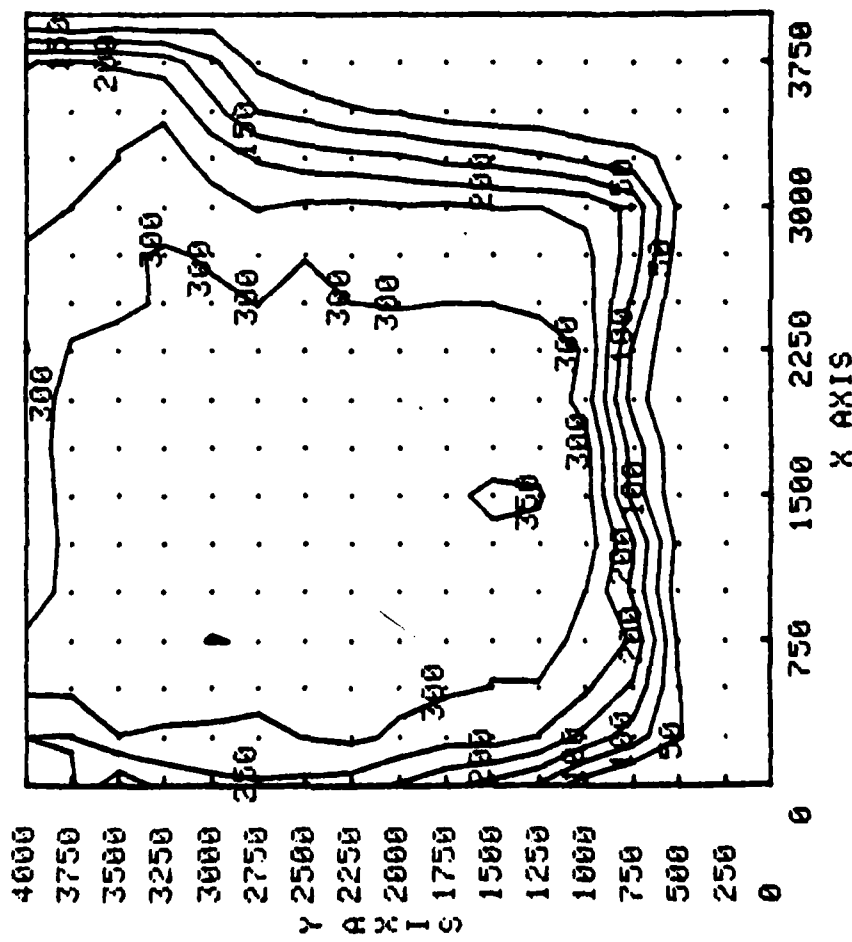
## PART II

### EFFECTS OF ETCHING ON SPECTRA OF ION IMPLANTED GaAs

This part of the studies also relates to ion-implanted GaAs particularly to investigations on the depth distribution of the implanted ions and the influence of etching. A whole series of samples of GaAs implanted with Be to a fluence of  $1 \times 10^{15} \text{ cm}^{-2}$  were studied. The samples were implanted in the usual manner described in Part I, then they were etched to depths of 1550 Å, 4250 Å, 6300 Å, 9200 Å, 10750 Å, and 13500 Å, and annealed at 800°C for 30 minutes. The etching was done by partly masking the sample and then the depths of etch steps were measured. The entire series was studied using the electrolyte electroreflectance technique described earlier. Fig. 18 shows the carrier distribution as revealed by the topographic scan of the unetched sample. As one would expect from a study of similar samples in earlier investigations the topographic scan reveals a fairly uniform distribution with a maximum of variation of 20%. The contour diagram in Fig. 18 and the three dimensional representation in Fig. 19 show such a feature for the unetched sample.

The sample with an etch step of 1550 Å gives the contour diagram and three dimensional characteristics shown in Figs. 20 and 21 respectively. There appears to be a considerable variation

Grav:Be (1\*10<sup>-15</sup>/cm<sup>3</sup>) L79 (unetched from stepped series)



Gage:Be (1x10<sup>-15</sup>/cm<sup>2</sup>) L79 (unetched from stepped series)

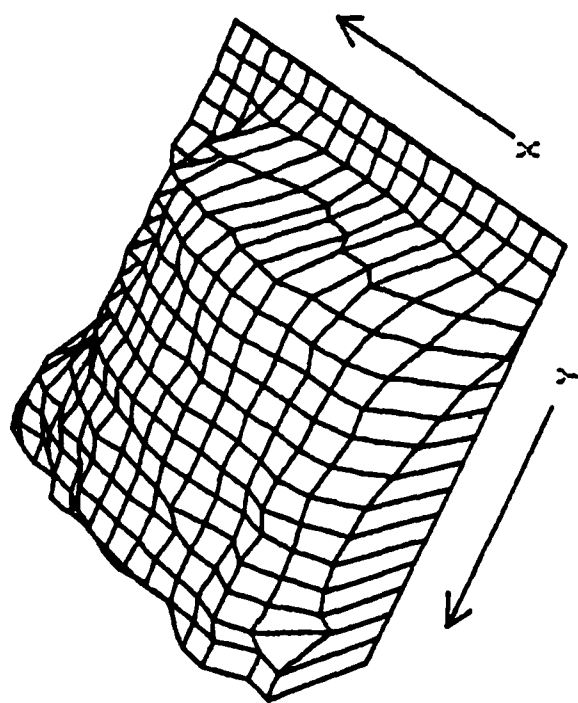


FIG. 19

step etched GaN/Be (110+115 nm) 1550 Å step -- L80

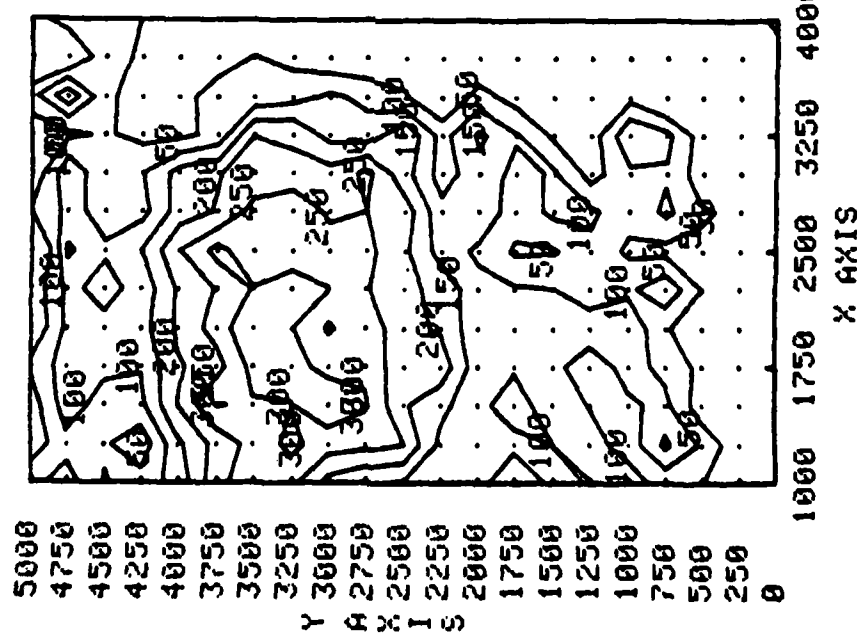


FIG. 20

Step etched GaN/Be (110115/cmcm) 1550 Å step -- L30

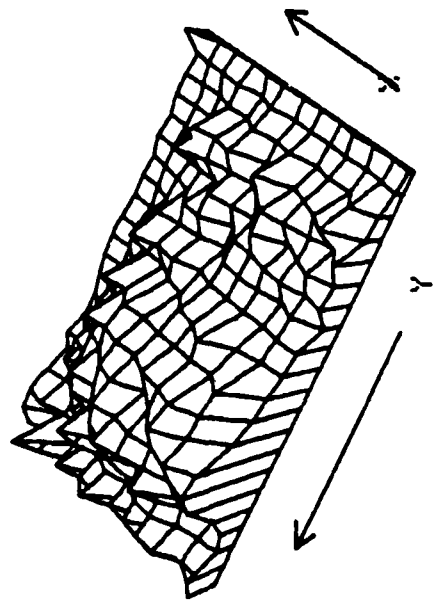


FIG. 21

in carrier concentration from a low of 50 to a high of 300 in relative units. Such a characteristic may be due to the surface degradation resulting in a nonuniformity of the electric field. This observation is in definite contrast to the features observed for the next sample in the series with an etch step of 4250 Å and shown in Figs. 22 and 23. This sample exhibits a "flat" contour with a slight slope towards the etch line as revealed also in Fig. 23. The most noteworthy are the features observed for the remaining samples in the series with etch steps from 6300 Å to 13500 Å. The observations for 6300 Å step sample are shown in Figs. 24 - 26. The two three dimensional characteristics shown in Figs. 25 and 26 are obtained for two different configurations of the sample by rotating the sample by 90°. There is a clear demarcation region with nearly 50% decrease in carrier concentration (300 vs 700 in relative units). While, as mentioned above, the same contrasts in the distribution of carrier concentration are observed in the case of samples with etch steps of 9200 Å, 10750 Å, and 13500 Å, for the sample with 10750 Å step two steps were observed in our experiments. These are shown in Figs. 27 and 28. In fact the visual examinations of the sample also confirmed the observation of this feature. For the sample with the etch step with maximum depth of 13500 Å, the contour diagram (Fig. 29) indicates a variation of carrier concentration from 50 to 350 in relative units and in this sense it is similar

step etched GaAs:Be (110115 cm<sup>-1</sup>) 4250 Å step -- 183

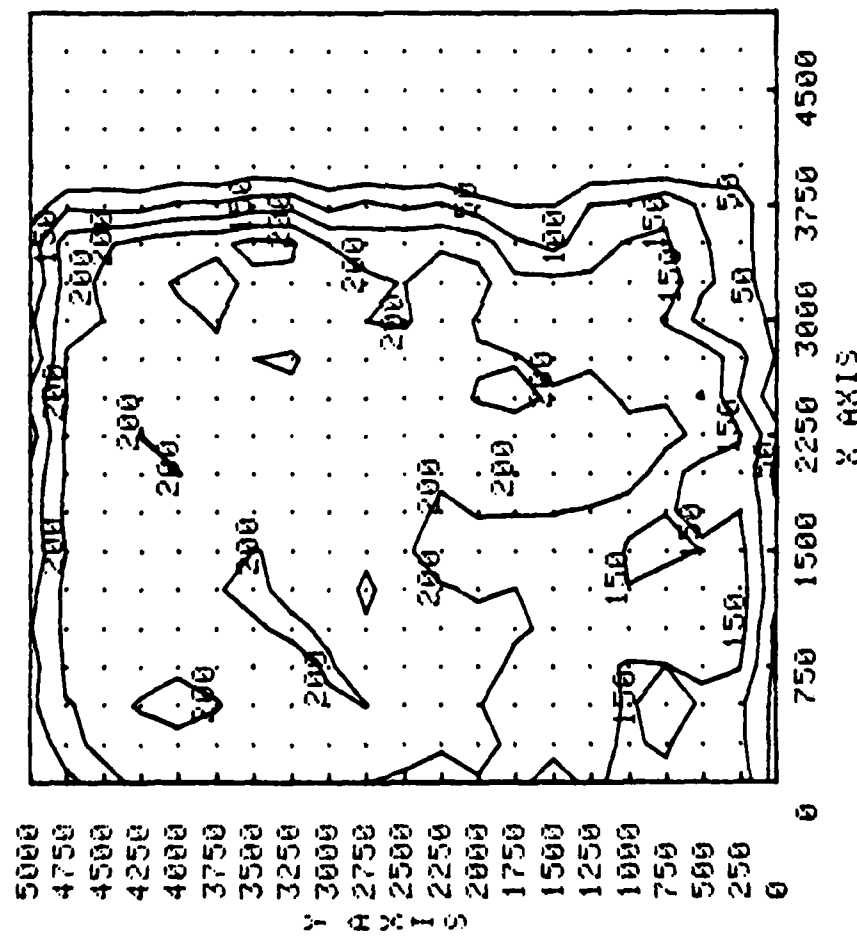


FIG. 22

Step etched GaAs:Be (110115/cm<sup>2</sup>) 4250 Å step -- L83

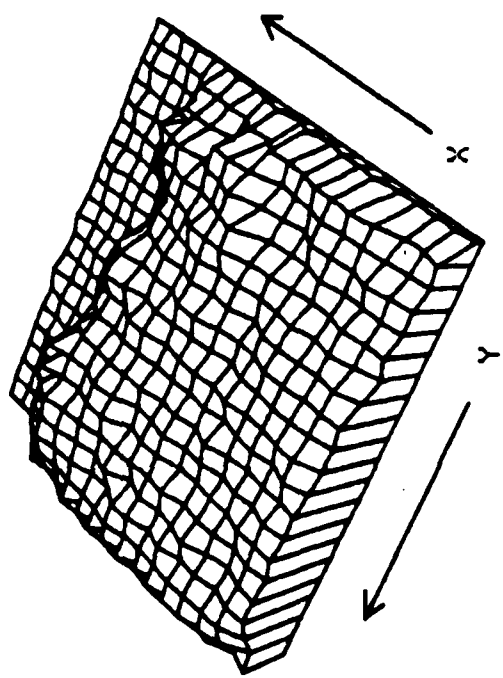


FIG. 23

step etched GaAs:Be (1110±15°/cm<sup>3</sup>) 6300 Å step -- L34

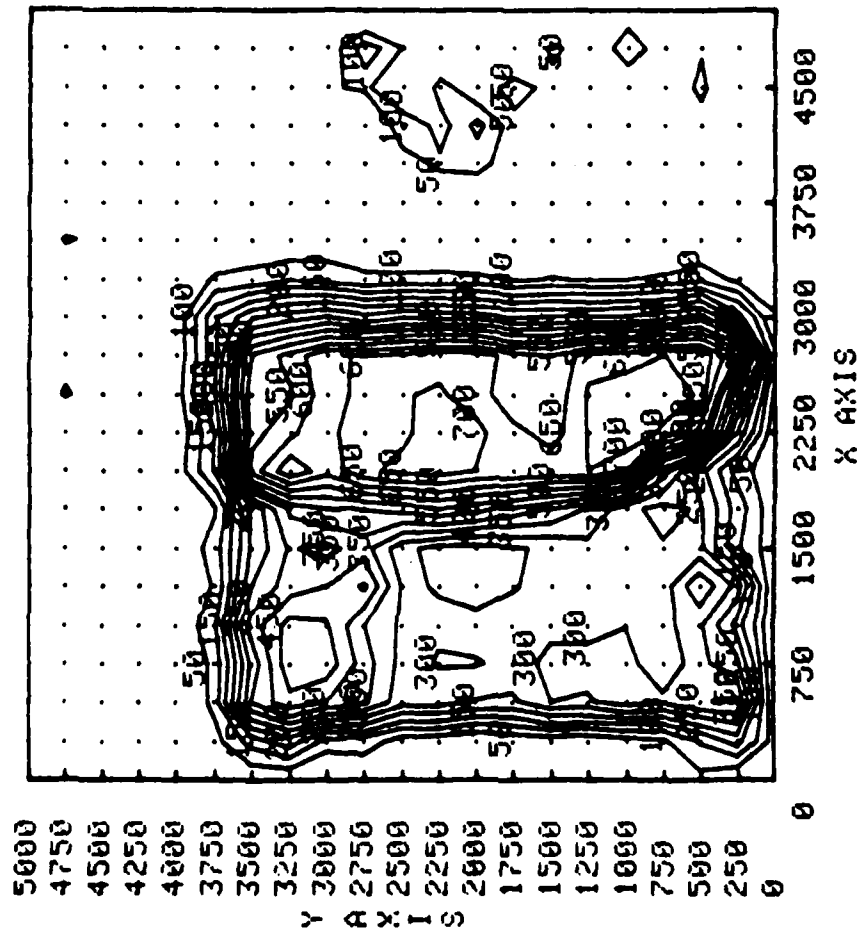


FIG. 24

step etched GaAs:Be (1x10<sup>-15</sup> cm<sup>-3</sup>) 6300 A step -- L84

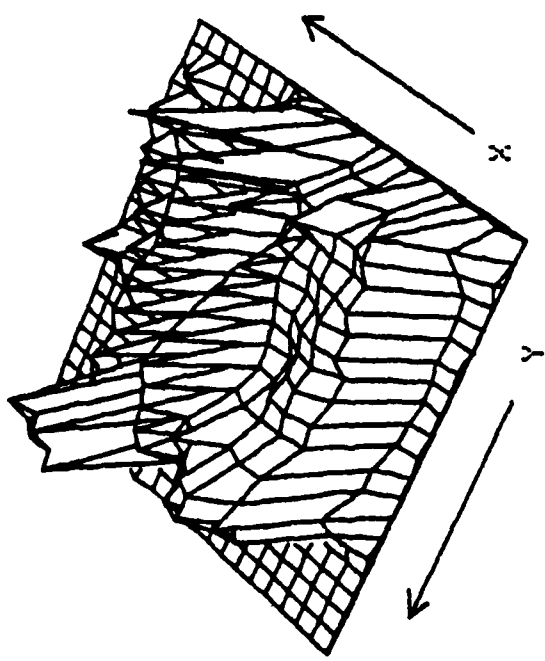


FIG. 25

After etched GaAs:Be (1x10<sup>-15</sup> cm<sup>-3</sup>) 6300 Å step -- L84  
quarter rotation

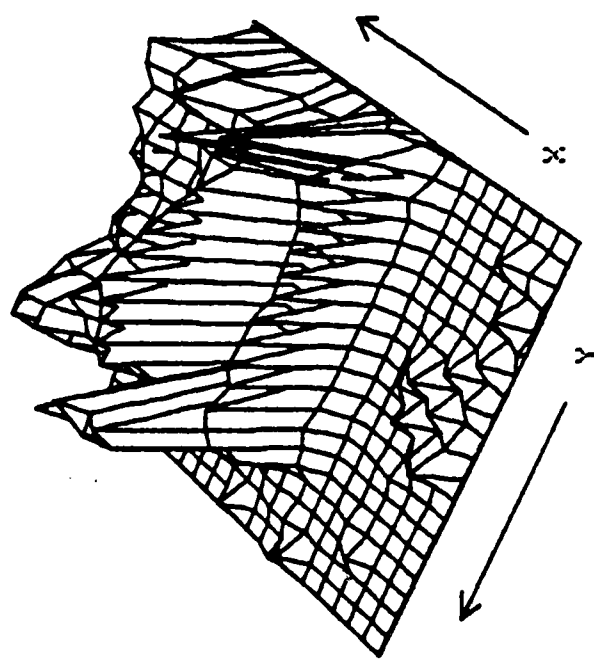
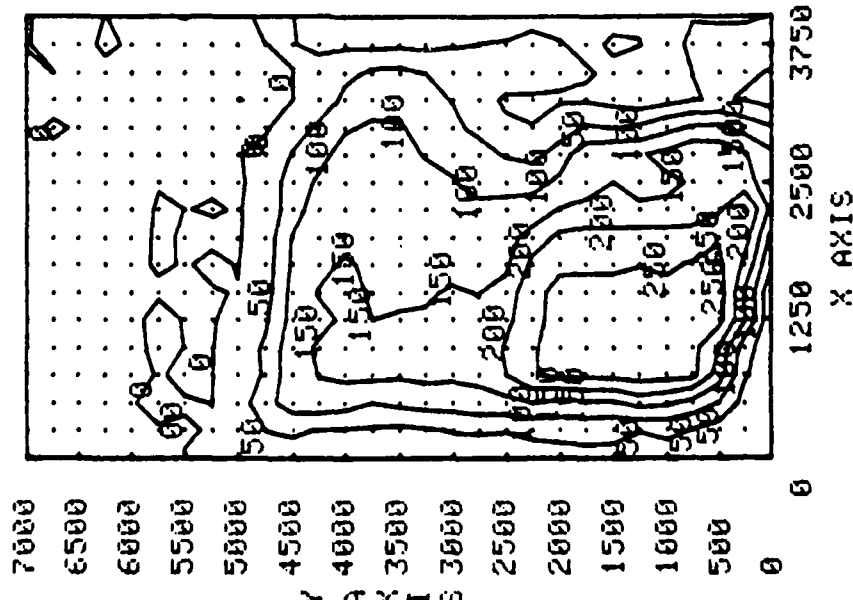


FIG 26

Etched Gates: Be (1\*10<sup>15</sup>/cm<sup>2</sup>) 10750 A step -- 182



Etched GaAs:Be (1x10<sup>-15</sup>/cm<sup>2</sup>) 10750 Å step -- 182

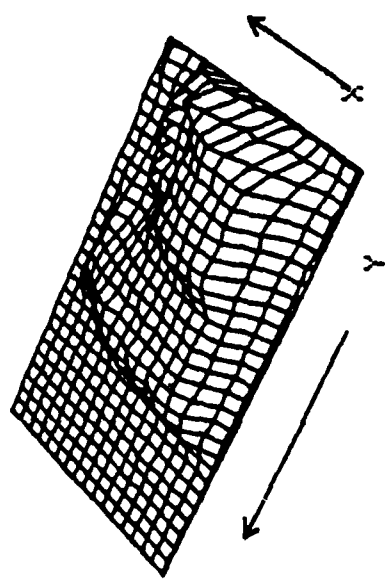
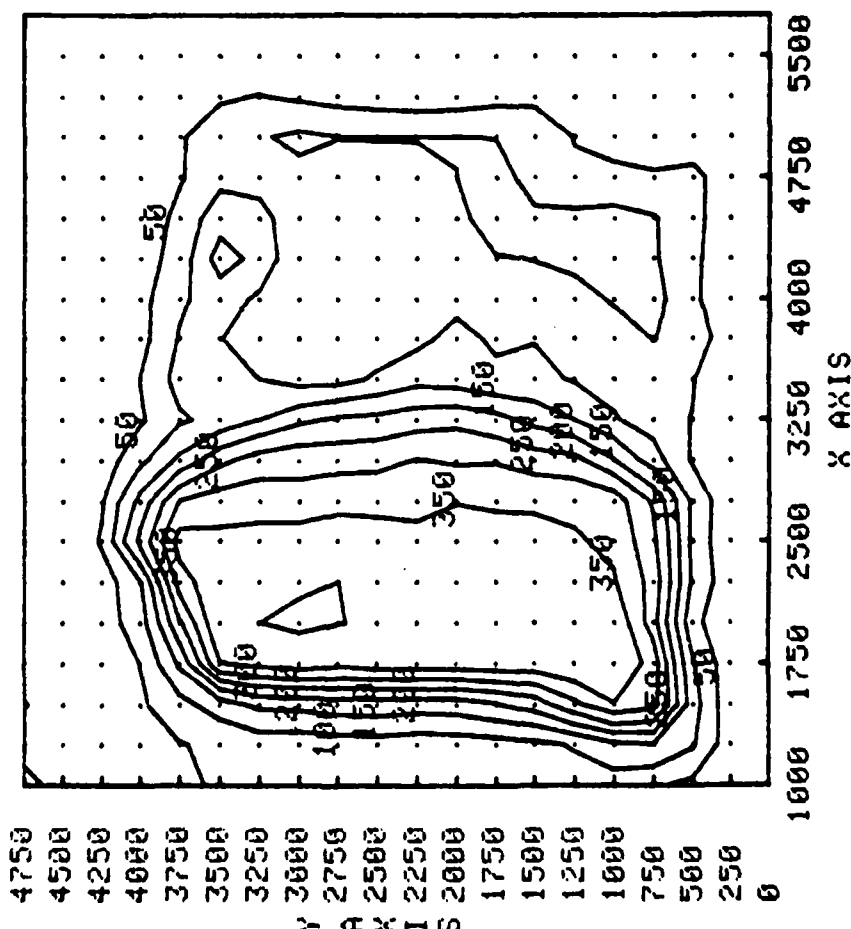


FIG 28

step etched GaAs:Be (1x10x15 μm<sup>3</sup>) 13500 Å step -- 178



to the characteristic exhibited by the sample with 1550 Å etch step. The three dimensional representations for two configurations of the sample obtained by rotating through 180° are also shown in Figs. 30 and 31 and one can notice the much sharper features indicating nearly 80% drop in the carrier concentration.

In a related set of experiments, we also examined another series of samples of GaAs with Be ions as implants at an energy of 250 keV to a fluence of  $1 \times 10^{15} \text{ cm}^{-2}$ . These samples also had two portions on each surface one unetched (by prior masking of the area) and the other an etched portion. The etched portions of three samples with etch depths of 3000 Å, 8500 Å, and 14000 Å were examined. For each sample two different points on the etched portion were chosen and the electroreflectance spectra were obtained. For the sample with 3000 Å etch step the spectra corresponding to two different points on the etched surface are shown in Figs. 32 and 33. They do show the usual energy shifts but a noticeable difference in the strength of the electroreflectance signal. Fig. 34 shows the topographical variation of the amplitude of the electroreflectance signal and an almost straight boundary separating two regions of different amplitude is indicated. However, as shown in the figure insert, this boundary does not seem to correlate with the boundary of the etch step. In Fig. 35 we

Step etched GaAs:Be (1x10<sup>15</sup>/cm<sup>3</sup>) 13500 Å step -- 178

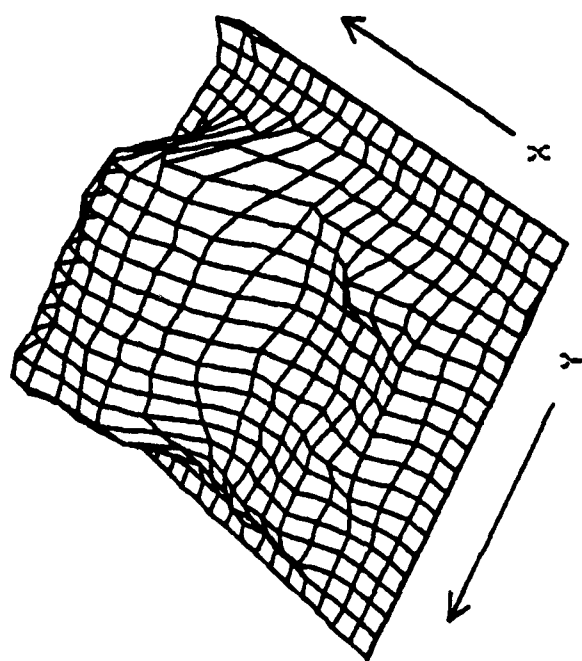


FIG 30

Step etched GaAs:Be (1\*10<sup>-15</sup>cm<sup>3</sup>) 13500 Å step -- 178

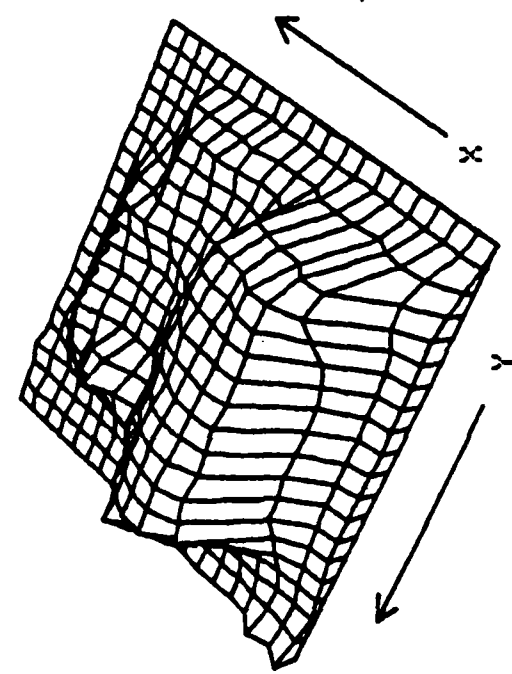


FIG 31

L33 Be<sub>2</sub>Ga<sub>5</sub> 6-60L 250 KeV 10<sup>11</sup>15 /cm/cm annealed, 3000 Å step

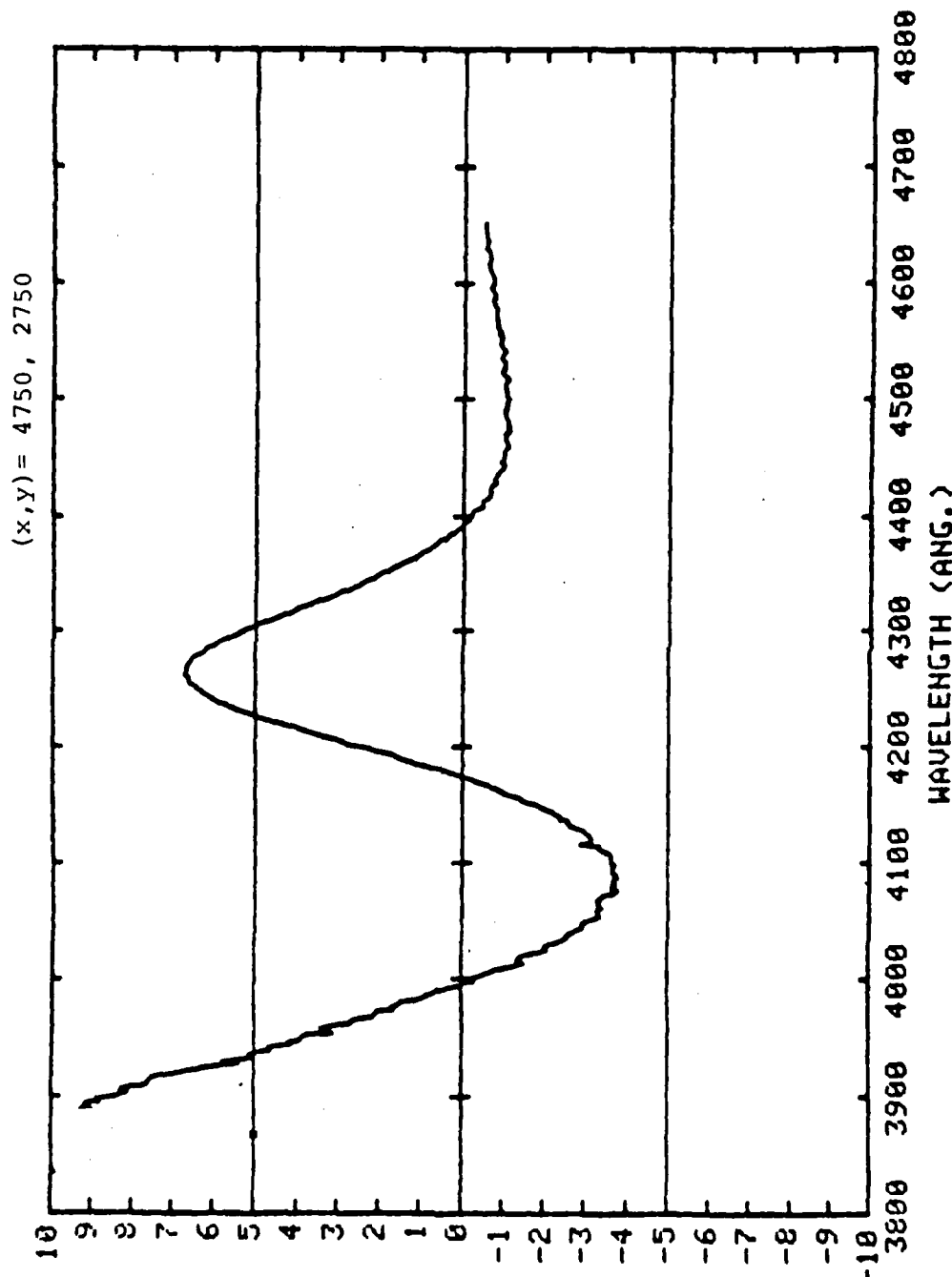
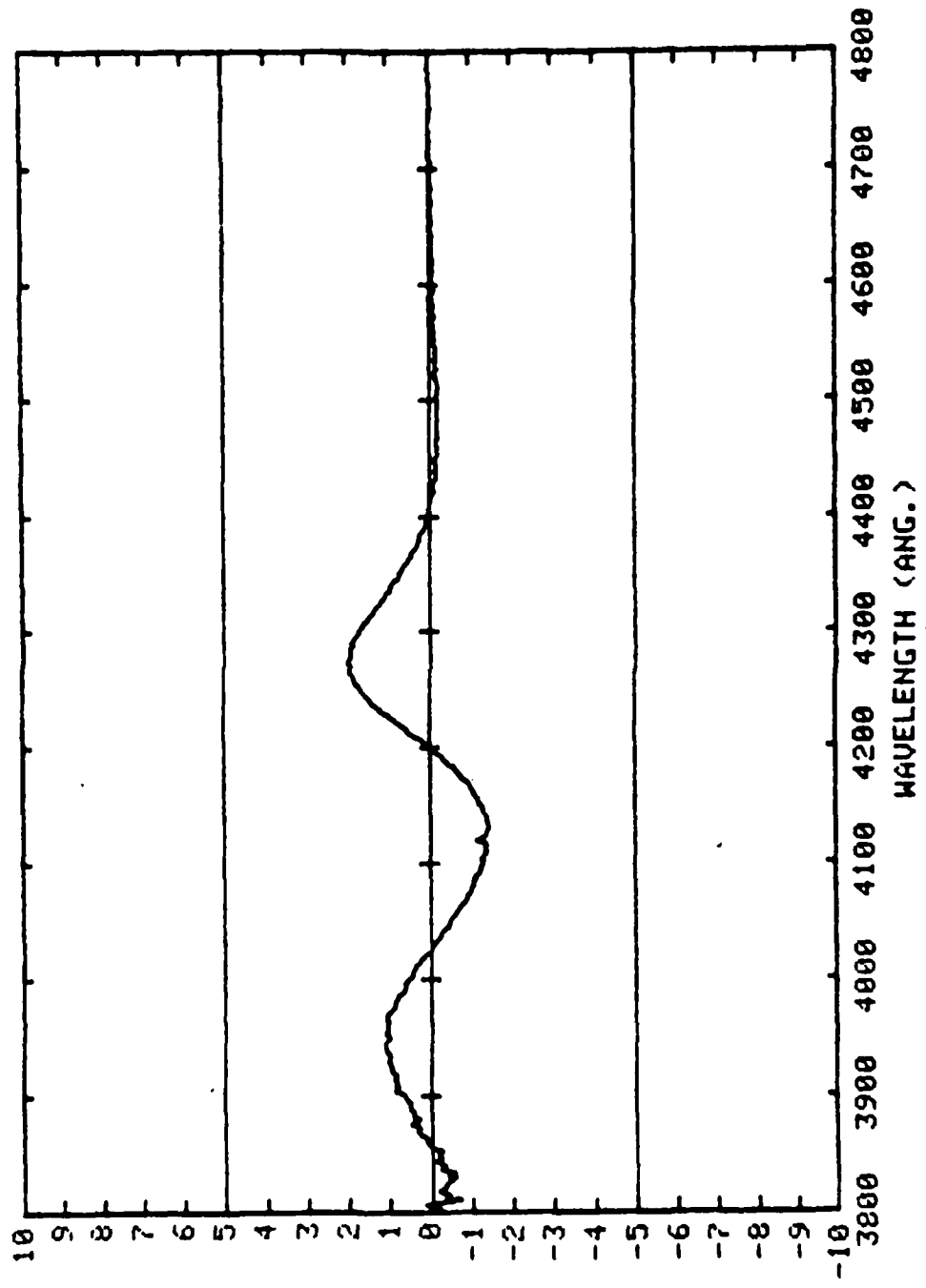
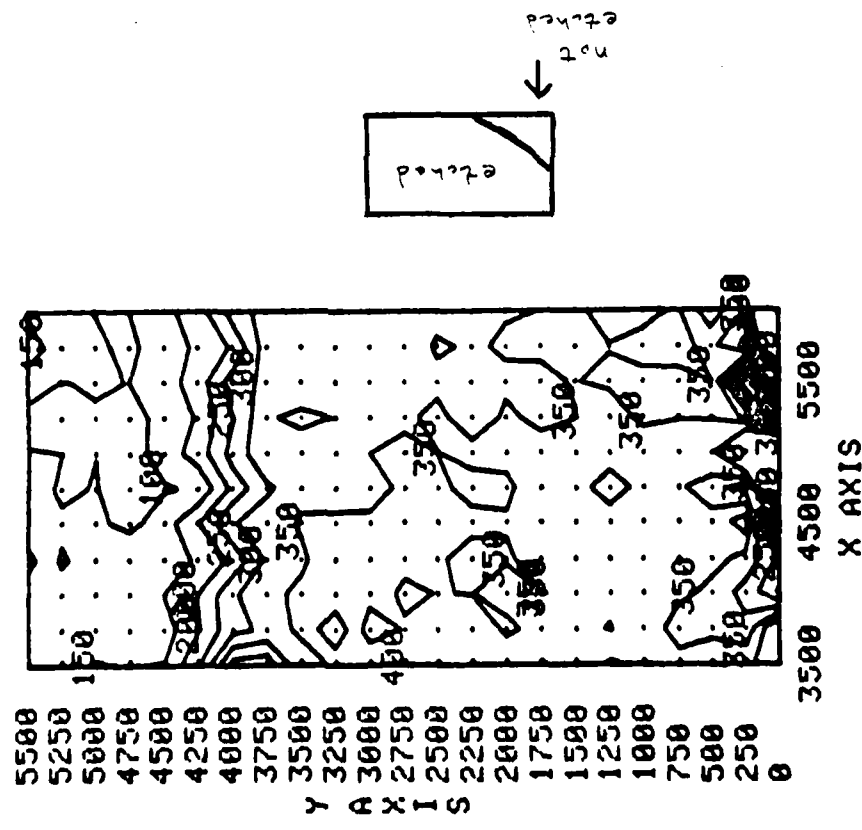


FIG. 32

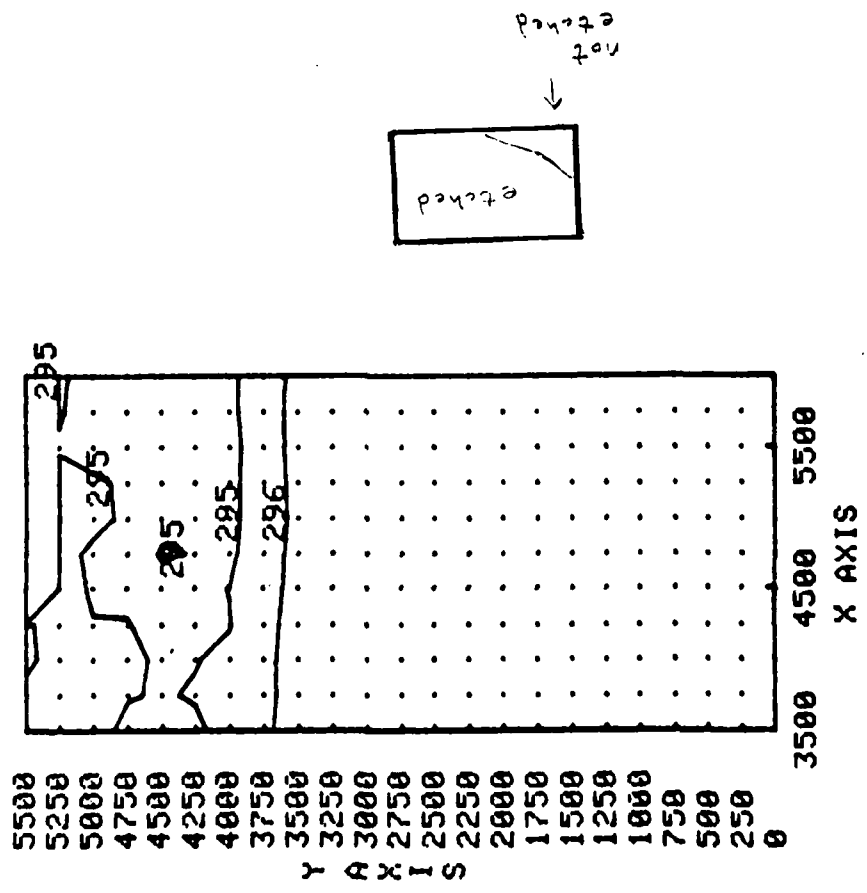
L33 Bi:Gauss 3000 Å step, spectrum taken at  $x, y = 4750, 5000$



L33 Be>GaAs 6-60L 250 KeV 10115 /cm/cm annealed, 3000 Å step



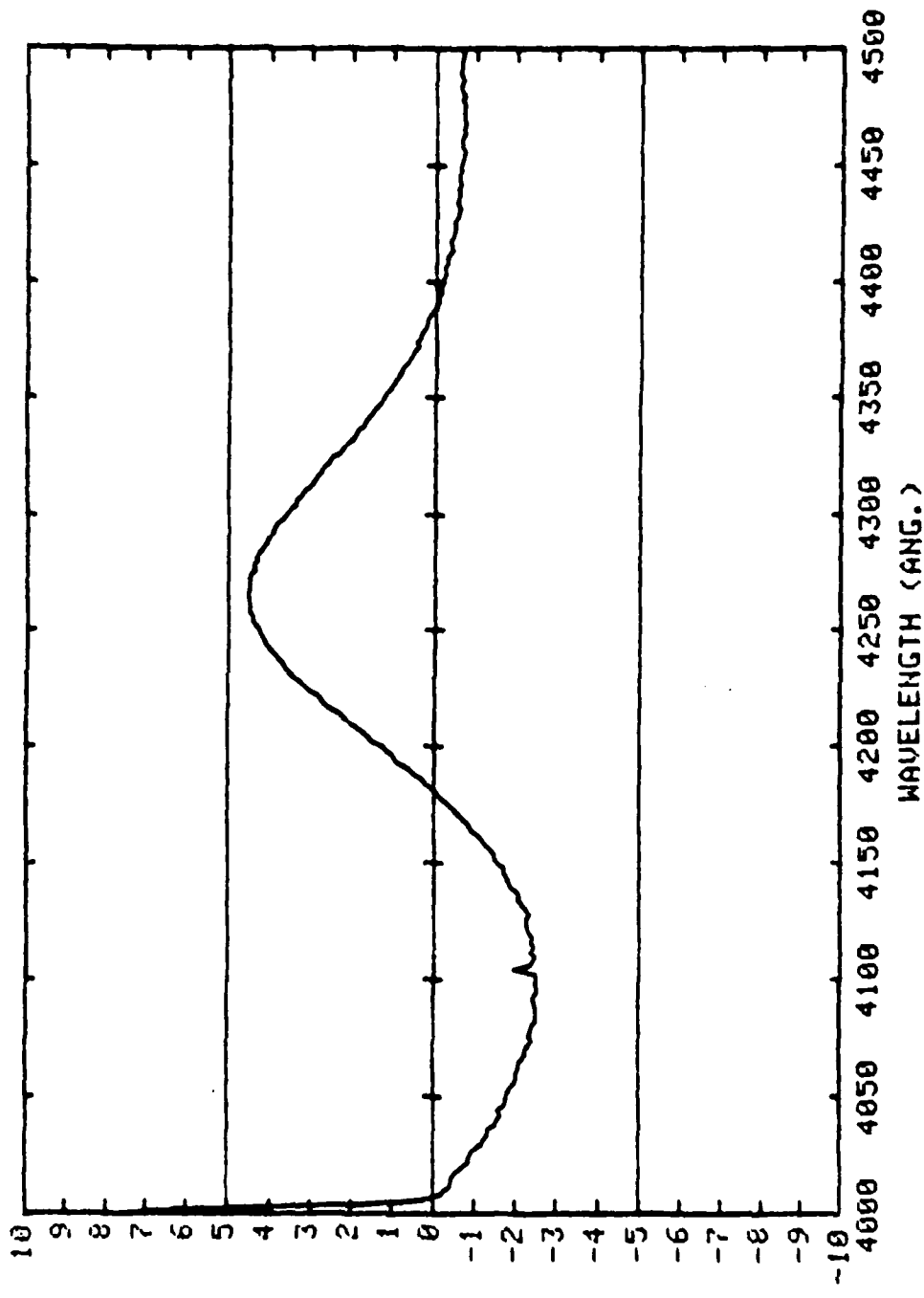
$E(x, y)$  L33 Be>GaAs 3000 Å step, zero near 3200 Å,



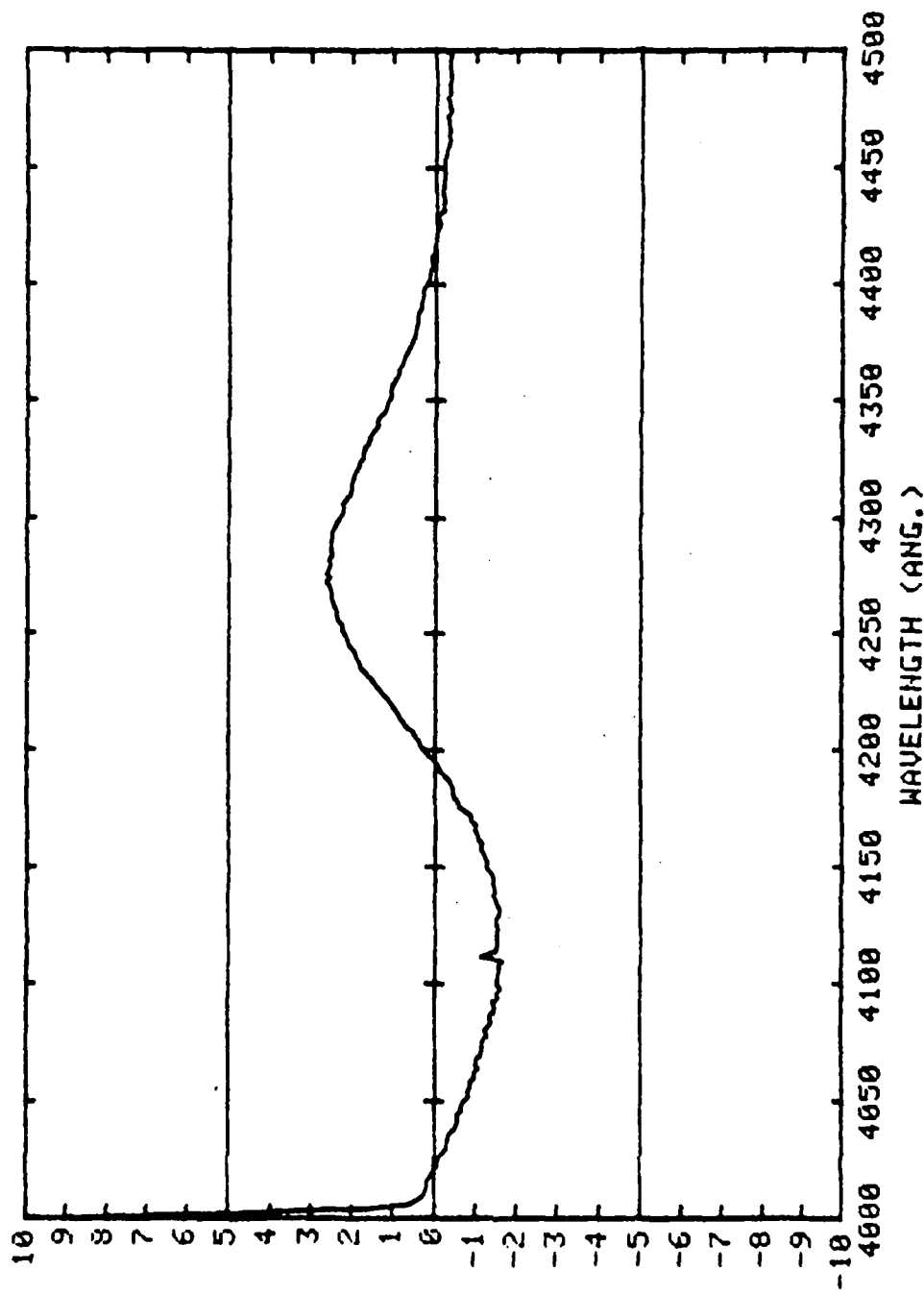
show the representation for the  $E_1$  zero crossing. A shift of nearly 10 meV was observed across the etch boundary. The behavior noticed in the second sample in this series with an etch step of 8500 Å shows some difference in comparison with the data on sample with 3000 Å step. Figures 36 and 37 correspond to the spectra and Fig. 38 shows the energy diagram where the boundary is the same as that of the etch step unlike in the previous case (Sample 1 of this series). Figs. 39, 40 and 41 show the spectrum, the amplitude diagram (carrier concentration profile) and the energy diagram respectively for the sample with 14000 Å etch step. The energy diagram shows a completely flat portion with no boundary as was observed in the first two cases. Finally, for comparison it was felt we should investigate a sample with very poor surface characteristics as revealed by visual observation. A sample of GaAs with Se implant was used for this purpose. In Fig. 42 and 43 are given the spectrum and the amplitude diagram respectively. It is worth noting that the spectral signal is very strong and there is a high degree of uniformity in carrier concentration (except near the edges). This observation indicates that the bulk characteristics are pretty good.

The above experiments were carried out to test the effects of the increases in the roughness of the surface with increasing depths of the etch step. More importantly, the significance of

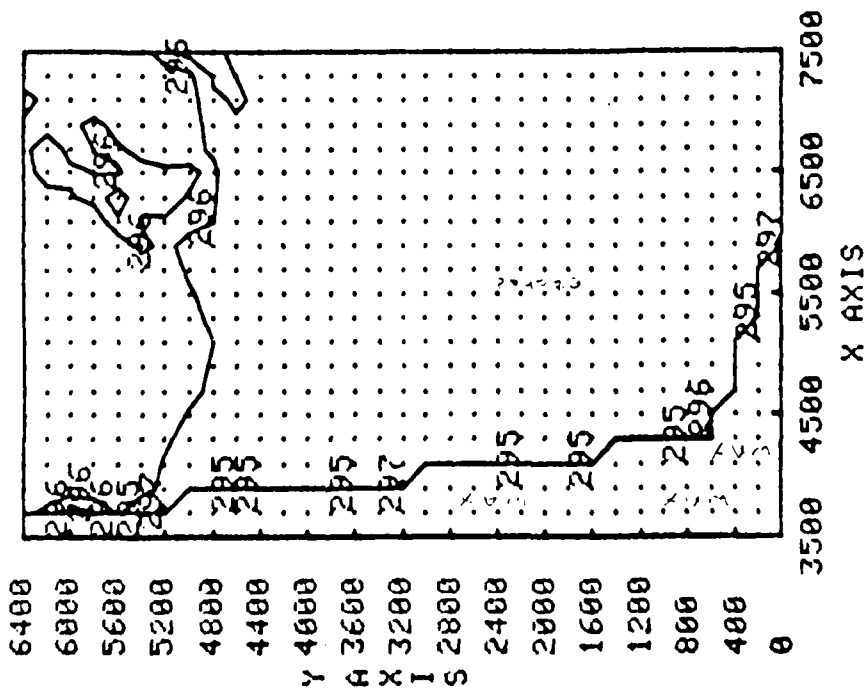
L34 Be'Gads 8500 Å step on surface, spect. at x,y=5500, 3250



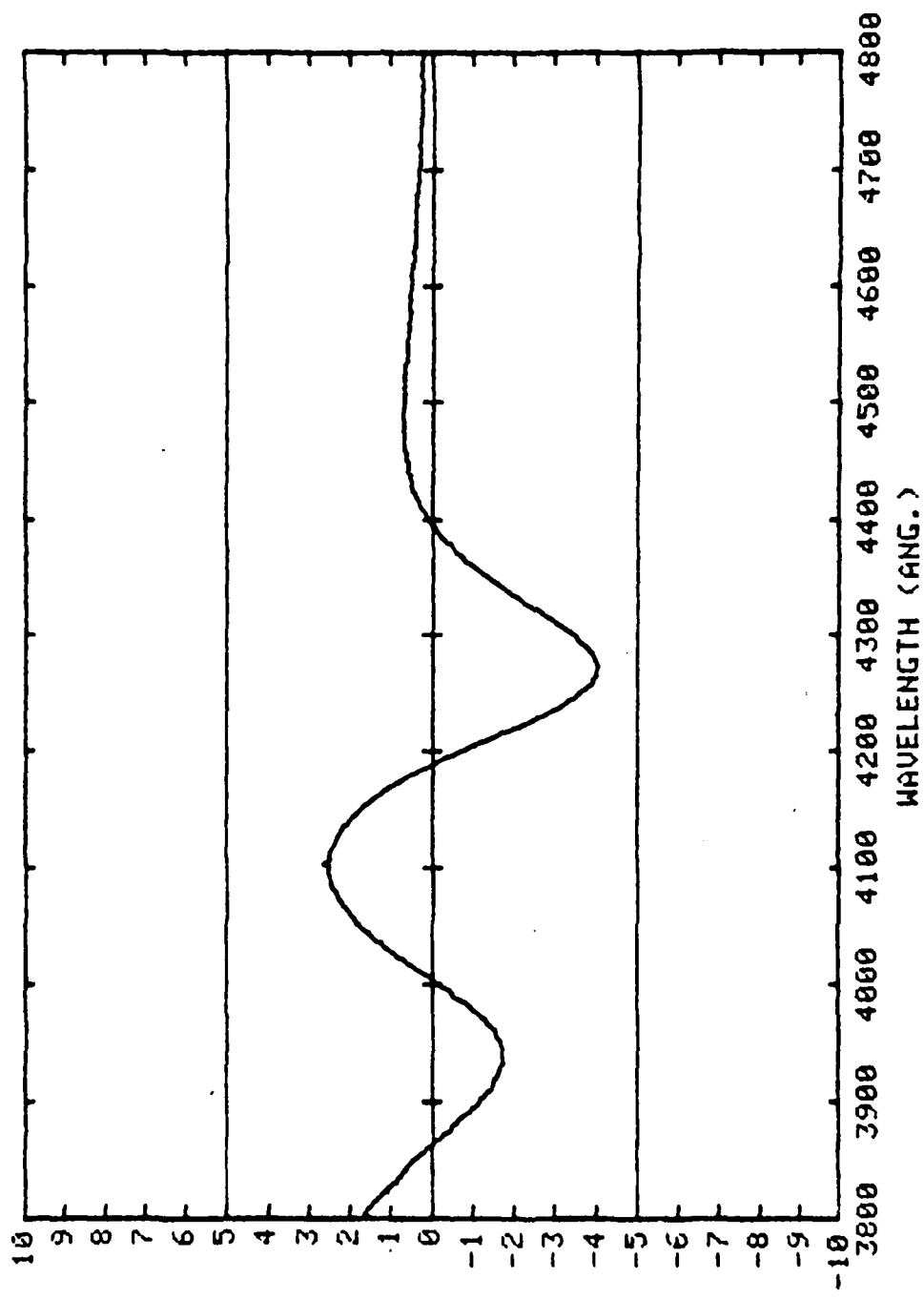
L34 Be<sub>2</sub>GaAs 8500 Å step on surface, spect. at x,y=5500,7000



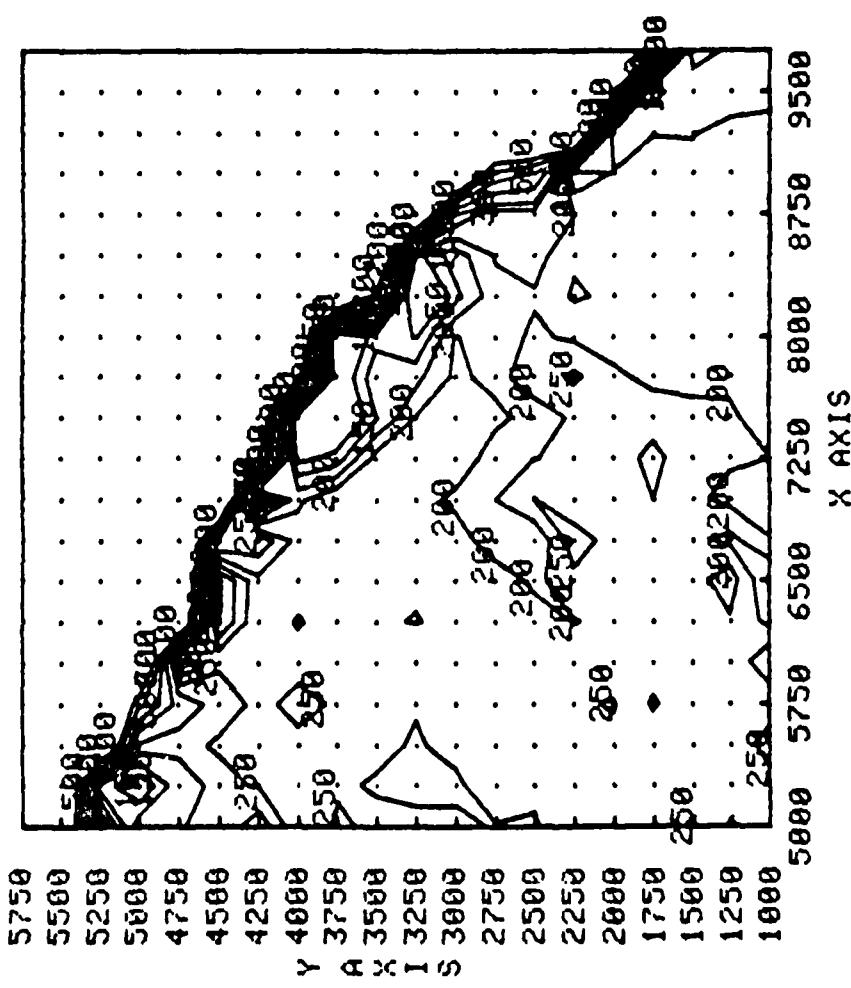
L34 Be:GaAs 8500 Å step on surface,  
 $E(x, y)$



L35 6-60L half etched with 14000 a step Be implant



L35 6-60L half etched with 14000 a step Be implant



L35 6-60L half etched with 14000 a step Be implant  
E (x, y)

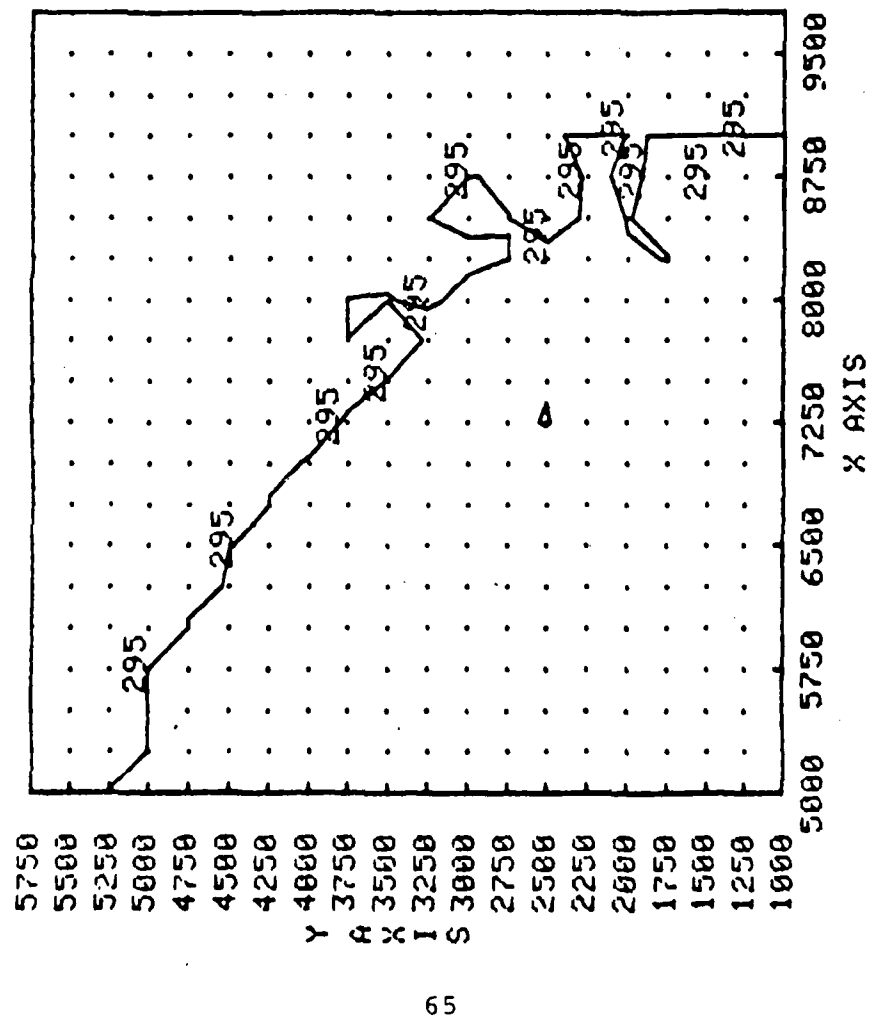


FIG. 41

L65 Se:GaAs(6-60L) 400 KeV, 5E14 /cm<sup>2</sup>cm, annealed 8 hours

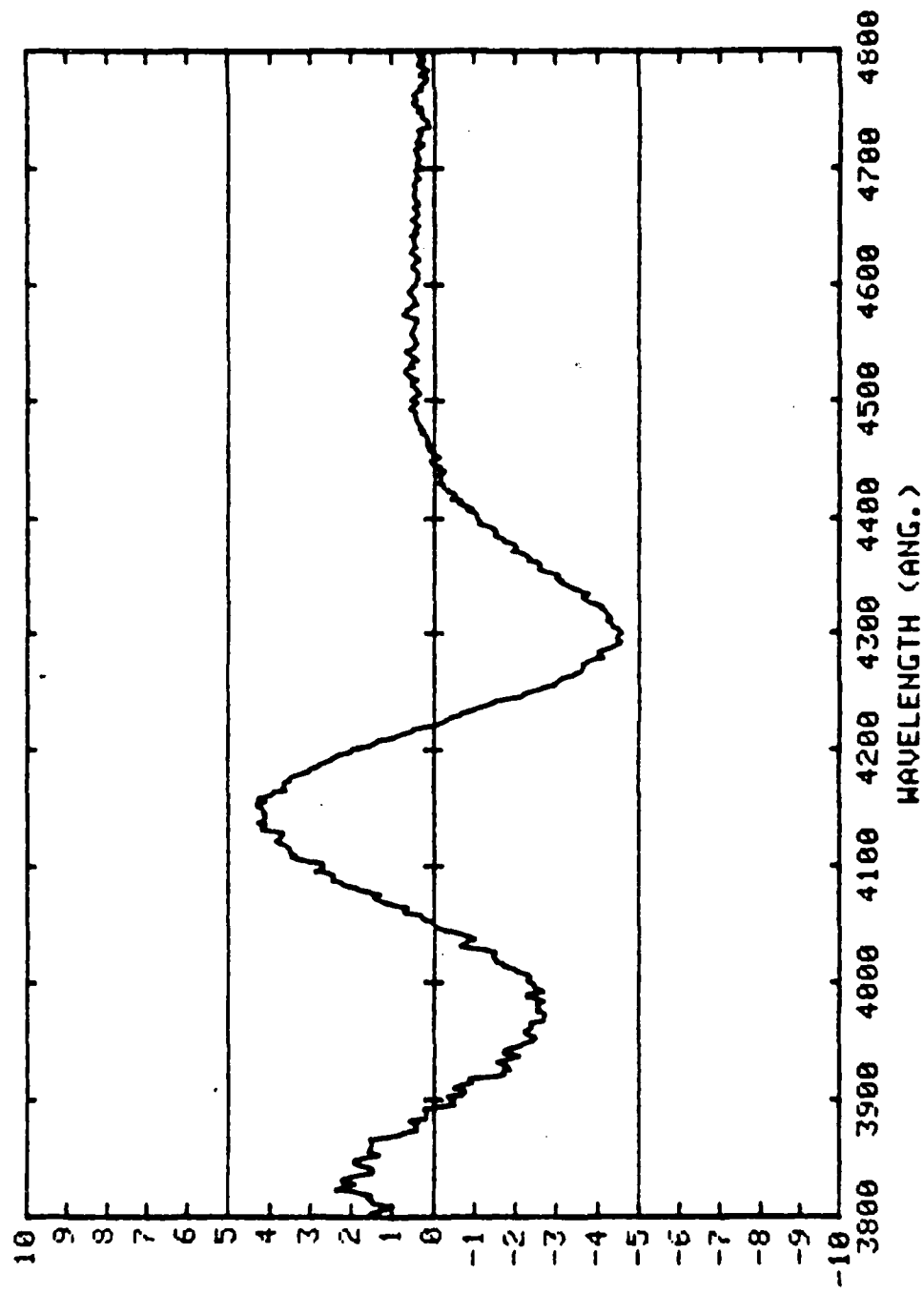
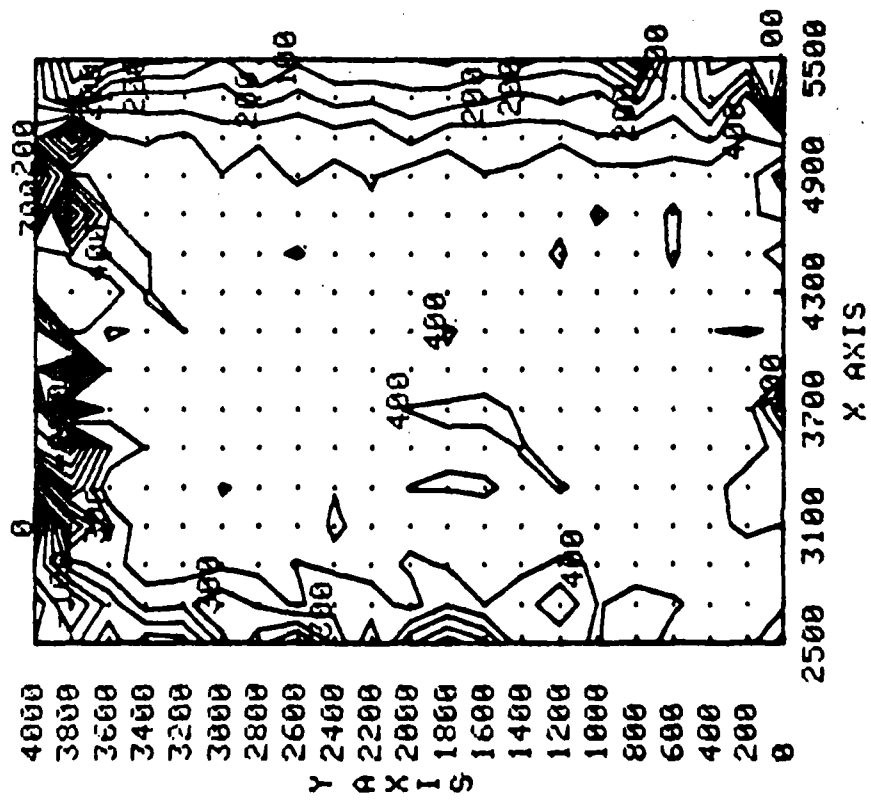


FIG.42

L65 Se<sub>2</sub>GeAs(6-60L) 400 KeV, 5E14 /cm<sup>2</sup>, annealed 8 Urns



the results observed in this series of investigations is that the method offers possibilities of profiling studies connected with implanted samples. From these one can develop models for redistribution of ions or variations in carrier concentrations.

### PART III

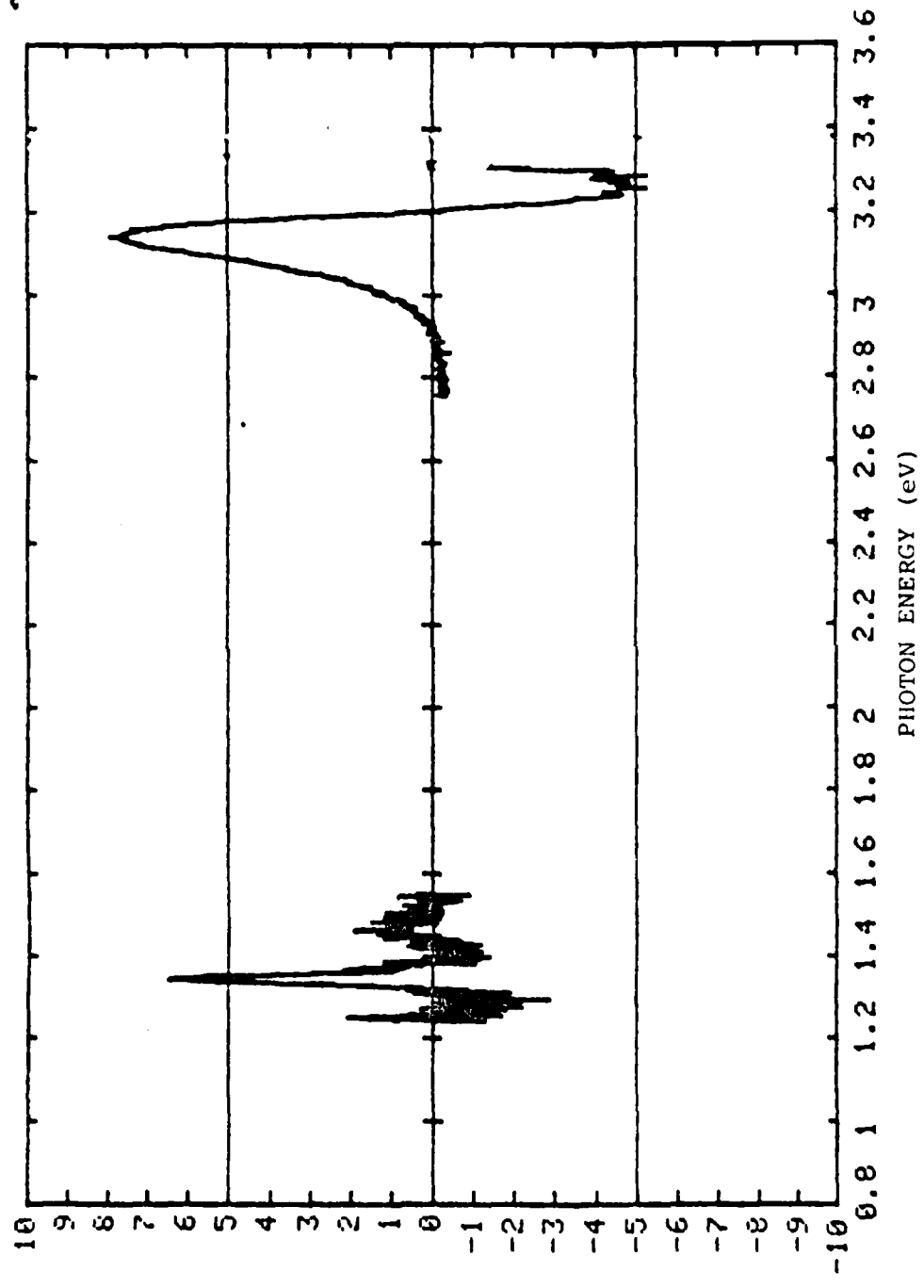
#### TOPOGRAPHIC EXAMINATION OF InP AND InGaAsP

The studies on the characteristics of InP consist of unimplanted samples and samples with Si implant. These samples were all grown at NRL and implanted by the ion-implantation group at NRL. The same electrolyte electroreflectance technique and the automated instrumentation developed in our laboratory were used for investigations of InP, InP:Si, and the quaternary alloy InGaAsP samples. The purpose of this phase of studies had the objectives of characterizing InP and also determining the transition energies as well as the behavior of quaternary alloys involving InP in view of the recent interest in these materials.

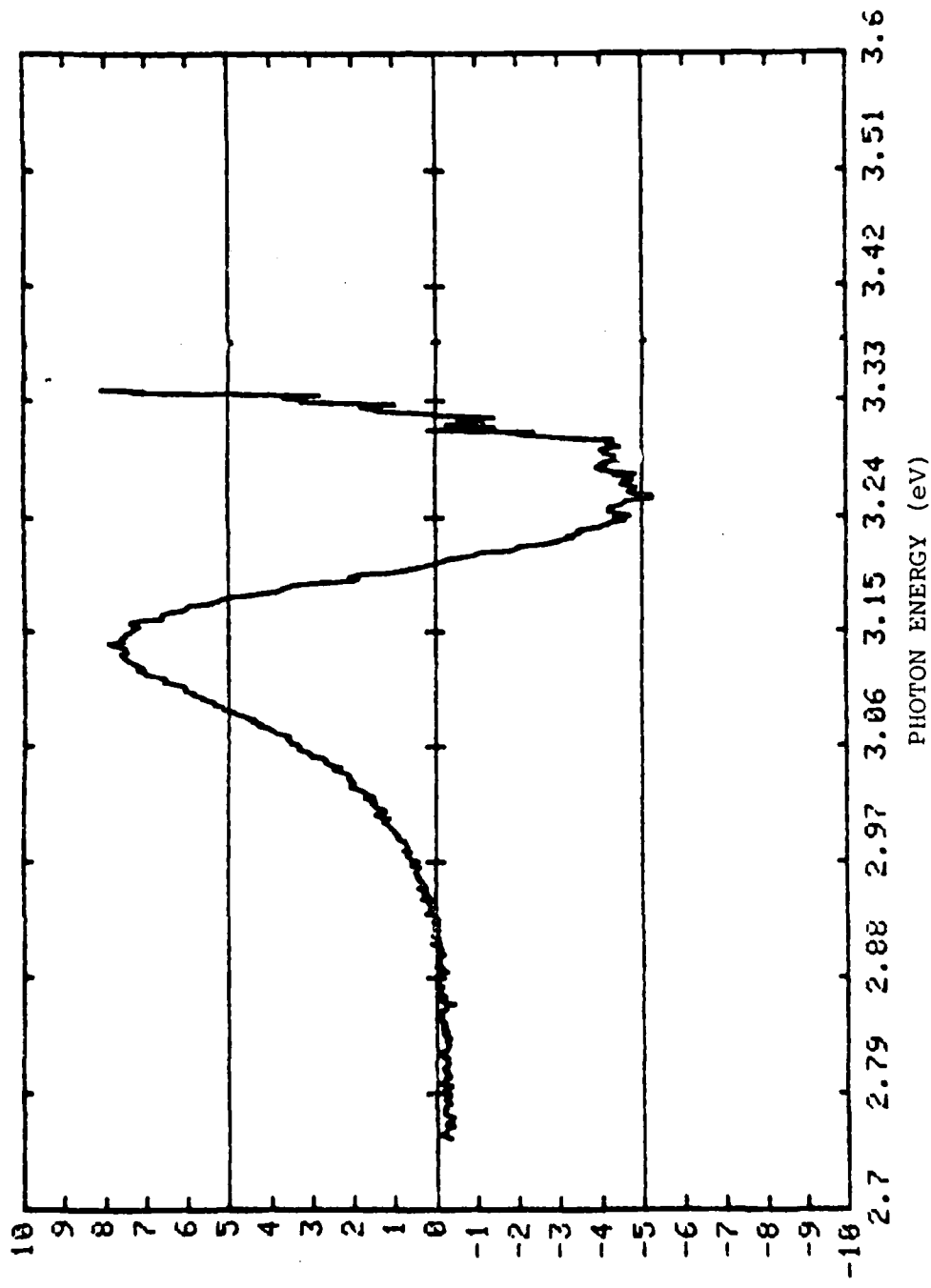
##### A. Unimplanted Samples of InP

The first unimplanted sample studied was labeled 1-81-H with Sn doping and Fig. 44 shows the peaks in the  $E_0$  and  $E_1$  regions. The positions of the peaks  $\sim 1.34$  eV and  $\sim 3.19$  eV agree with values reported in the literature by earlier authors. In Fig. 45 is shown the spectrum in 3.19 eV region. Very strong signal is obtained and the topographical scan of the surface indicated less than 3% spatial variation of carrier concentration. Using the peak  $\sim 3973\text{\AA}$ , the carrier concentration plot is illustrated in Fig. 46. Similar results have been obtained for another unimplanted sample of InP (marked as 2-13-H) with Sn and Fe doping.

Scan of InP 1-81-H



Scan of InP 1-81-H



Scan of InP 1-81-H  
3973 ang.

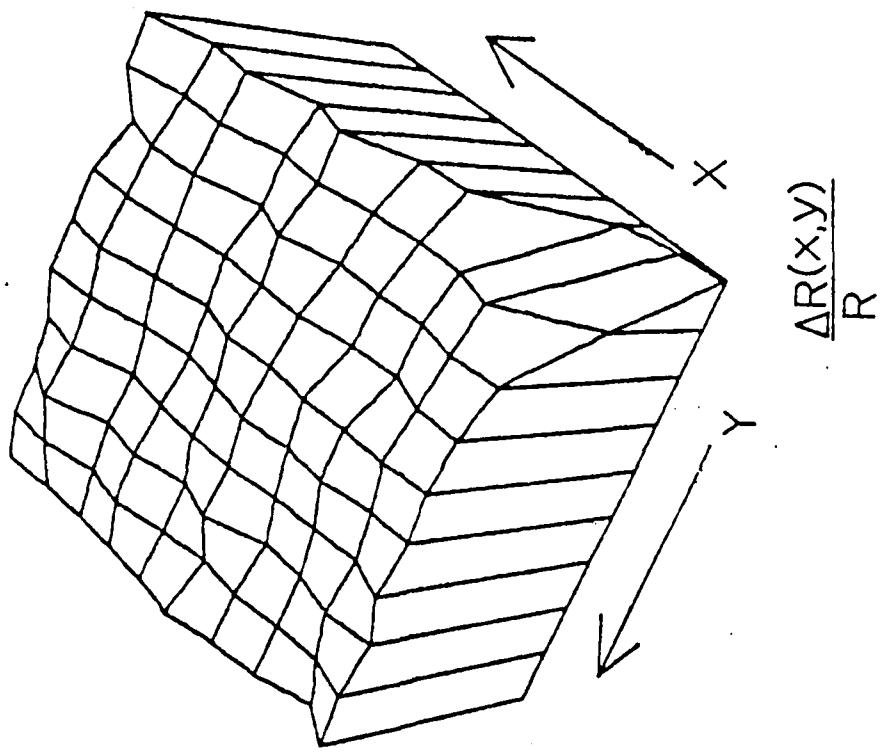


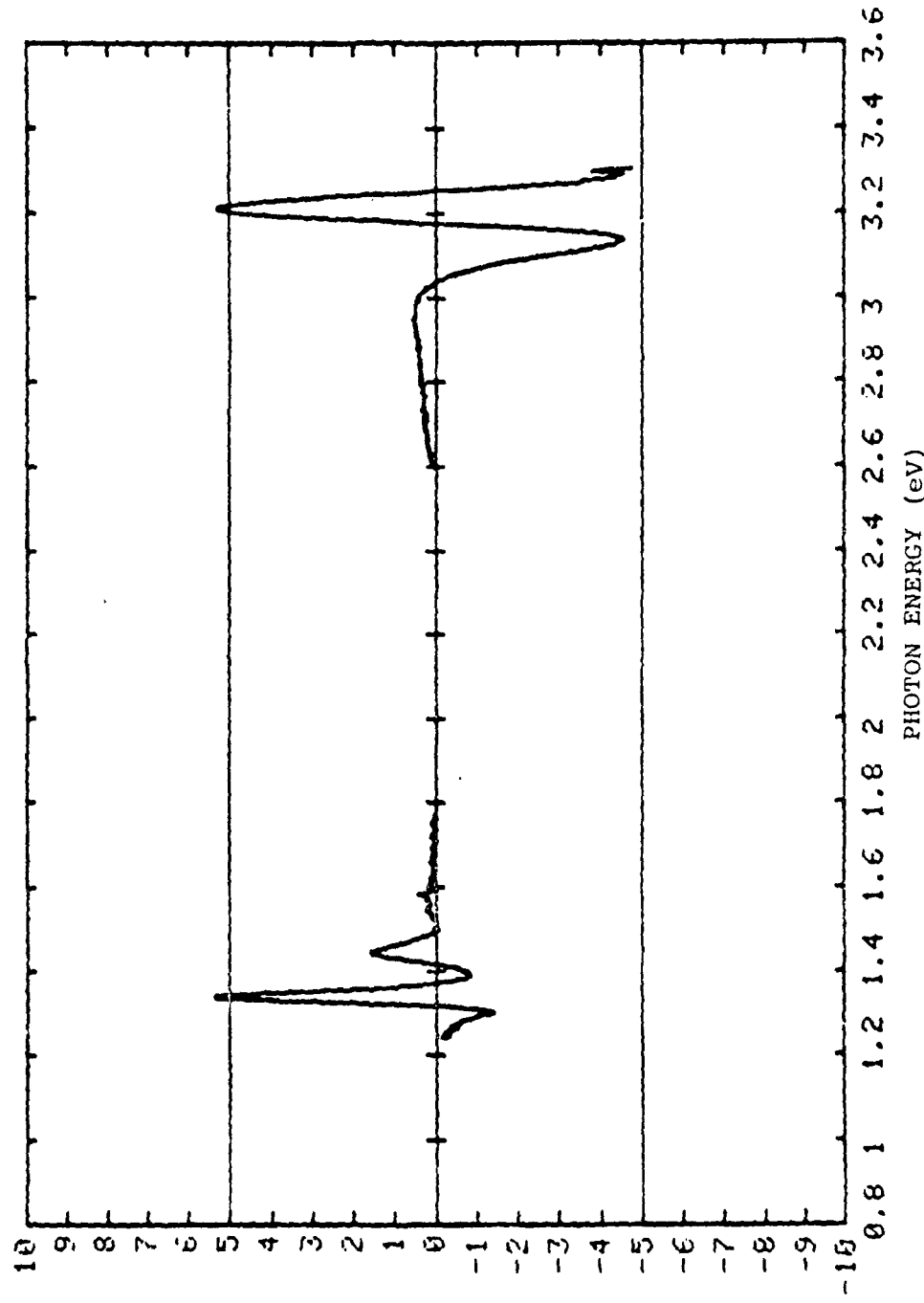
FIG. 46

Again  $\Delta R/R$  vs  $(x,y)$  is very uniform. The spectrum is shown in Fig. 47.

B. Implanted Samples--InP:Si

The studies on samples of InP implanted with Si are in the early stages and as such we have examined only a limited number of samples. The experiments on implanted but unannealed samples did not give a reasonable signal. In the case of implanted and annealed samples, it was possible to obtain enough signal. For the sample with  $5 \times 10^{14} \text{ cm}^{-2}$  fluence, the spectrum and the contour diagram for carrier concentration are shown in Figures 48 and 49 respectively. As in the case of GaAs:Si, there is a definite shift of the  $E_1$  peak by  $\sim 30$  meV. There are spatial variations of carrier concentration as exhibited by GaAs:Si samples. Further experiments in this series of implanted and annealed samples are continuing and the results will be compared with the data on unimplanted samples as well as data on implanted but unannealed samples if reasonably strong electroreflectance signals can be obtained. Just as we have presented detailed studies on implanted GaAs, we plan to analyze the results of these studies in a future phase of investigations and explain the shifts by nearly 30 meV. The data presented here are extremely significant to help in the understanding of the behavior of quaternary alloys involving InP.

Scan of InP ( Sn, Fe )  
( Sn, Fe doped ) 2-13-H



Scan of InP-Si implant  
L25 ( annealed )  
 $5 \times 10^{14} \text{ cm}^{-2}$

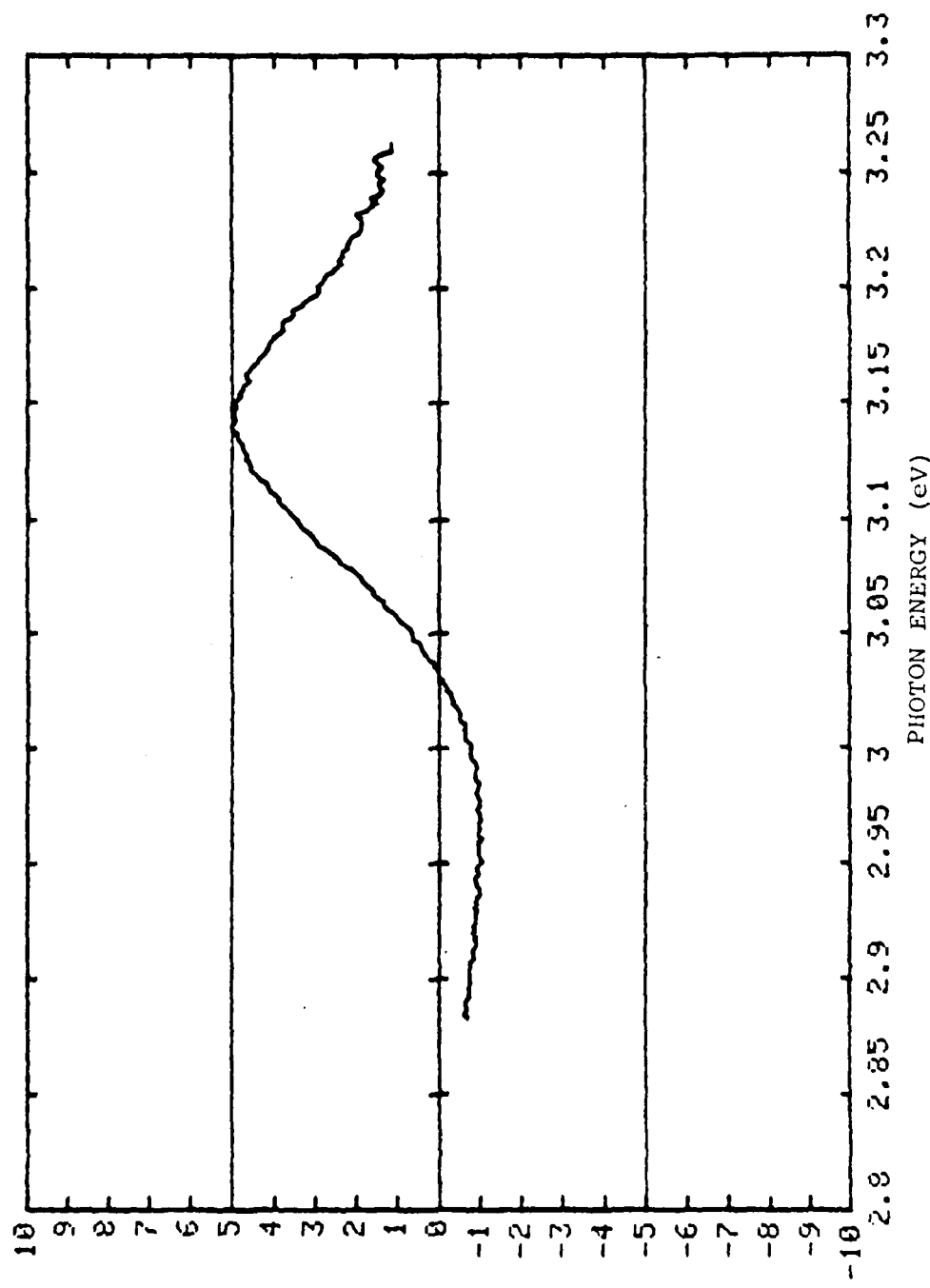
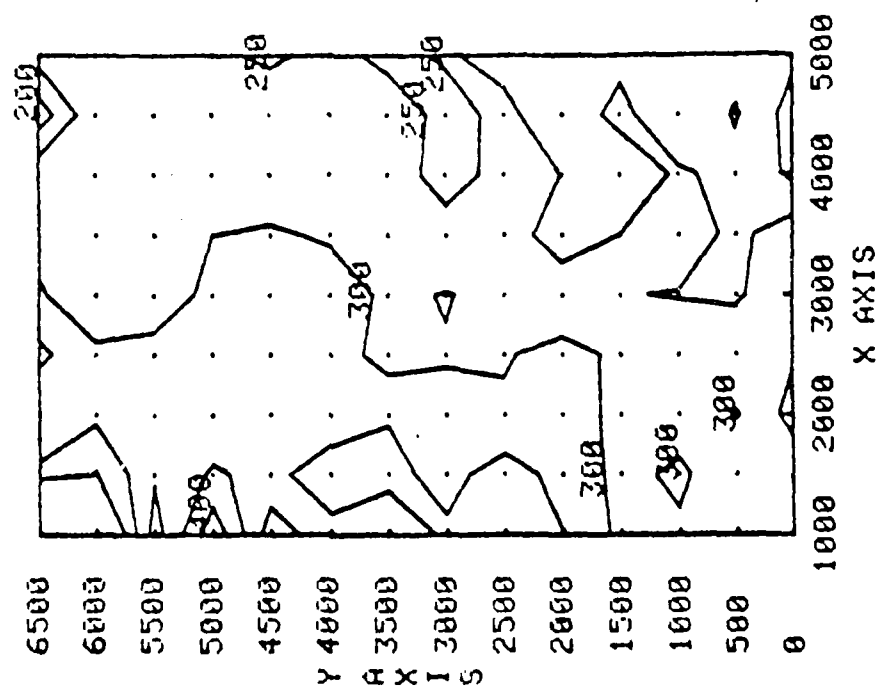


FIG. 48

InP-Si implant L25 3950 ang.  
 $5 \times 10^{14} \text{ cm}^{-2}$  ( annealed )



In another set of investigations, a series of InP samples with Be implant (provided by Dr. Comas) were also investigated. The fluences were  $5 \times 10^{12} \text{ cm}^{-2}$ ,  $5 \times 10^{14} \text{ cm}^{-2}$  and  $1 \times 10^{15} \text{ cm}^{-2}$ . In Figures 50 and 51 are shown the spectrum and contour diagram for the sample with  $5 \times 10^{12}$  fluence and Figures 52 and 53 give similar data for sample with  $5 \times 10^{14}$  fluence. For  $5 \times 10^{12}$  sample, the shift in energy is  $\sim 10 \text{ meV}$  compared with InP values and the contour diagram indicates a high degree of uniformity of carrier concentration. In the case of  $5 \times 10^{14}$  sample,  $E_1(1)$  is relatively unaffected while  $E_1(2)$  shifted by  $+100 \text{ meV}$ . The carrier concentration is not uniform (see Fig. 53). These results are very similar to our observations on implanted GaAs. For the sample with  $1 \times 10^{15}$  fluence, we were able to obtain only a very weak signal. Further experiments on implanted GaAs and InP are continuing.

### C. Quaternary Alloy InGaAsP

As part of our general objective to study the quaternary alloys of III-V semiconducting materials, we have made some preliminary measurements on two samples of InGaAsP (labelled 2-229 and 2-235) kindly provided by Professor Stillman at Urbana. These samples were grown on InP substrates. The spectral data have been obtained using our EER technique over the significant range of 0.9 eV to 3.6 eV. Both the front and back sides of the two samples have been examined and our results are shown in

L40a Be>InP 2-10-H 100 KeV 5E12 cm/cm<sup>2</sup> annealed, 8 Urns

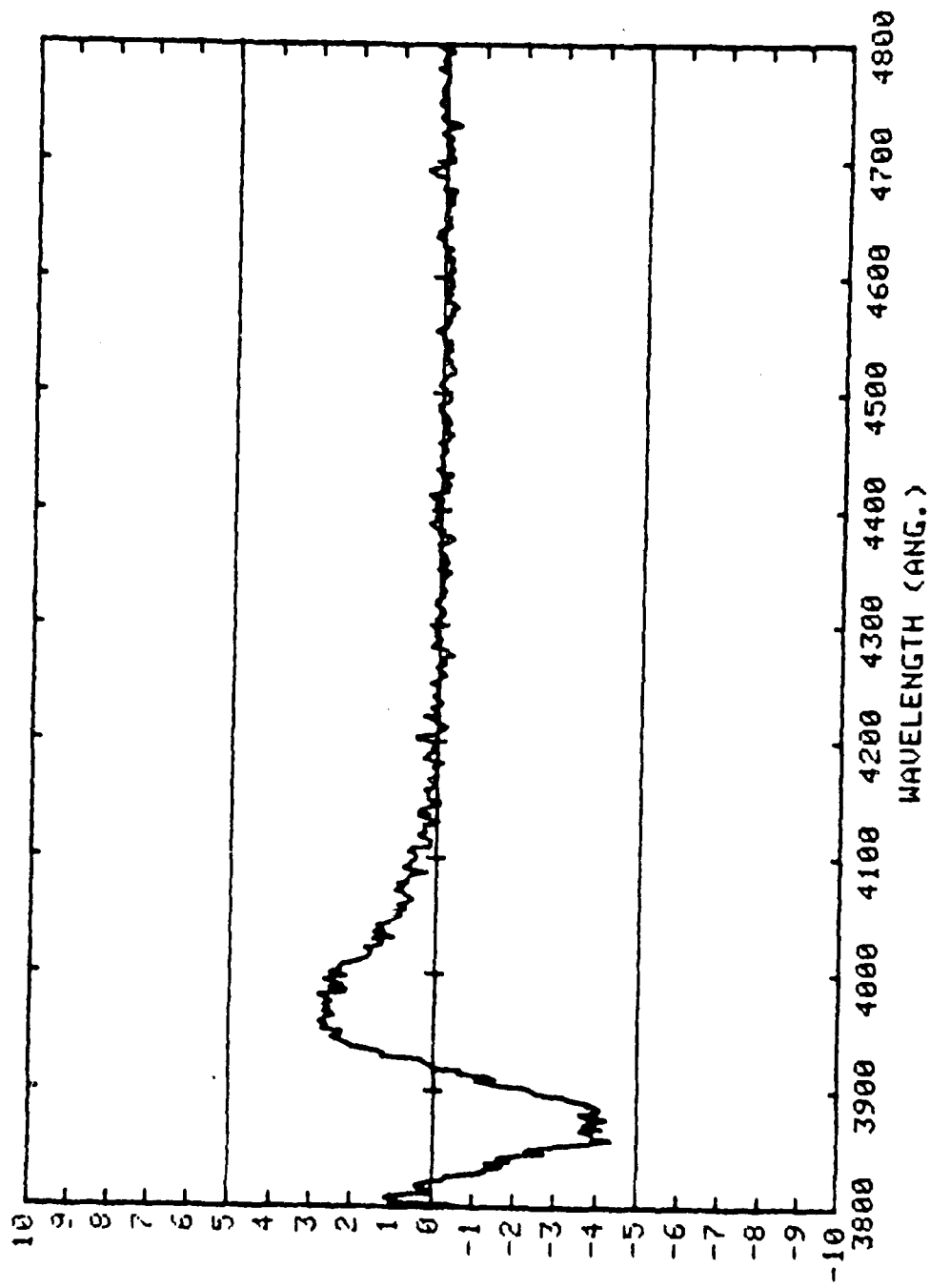
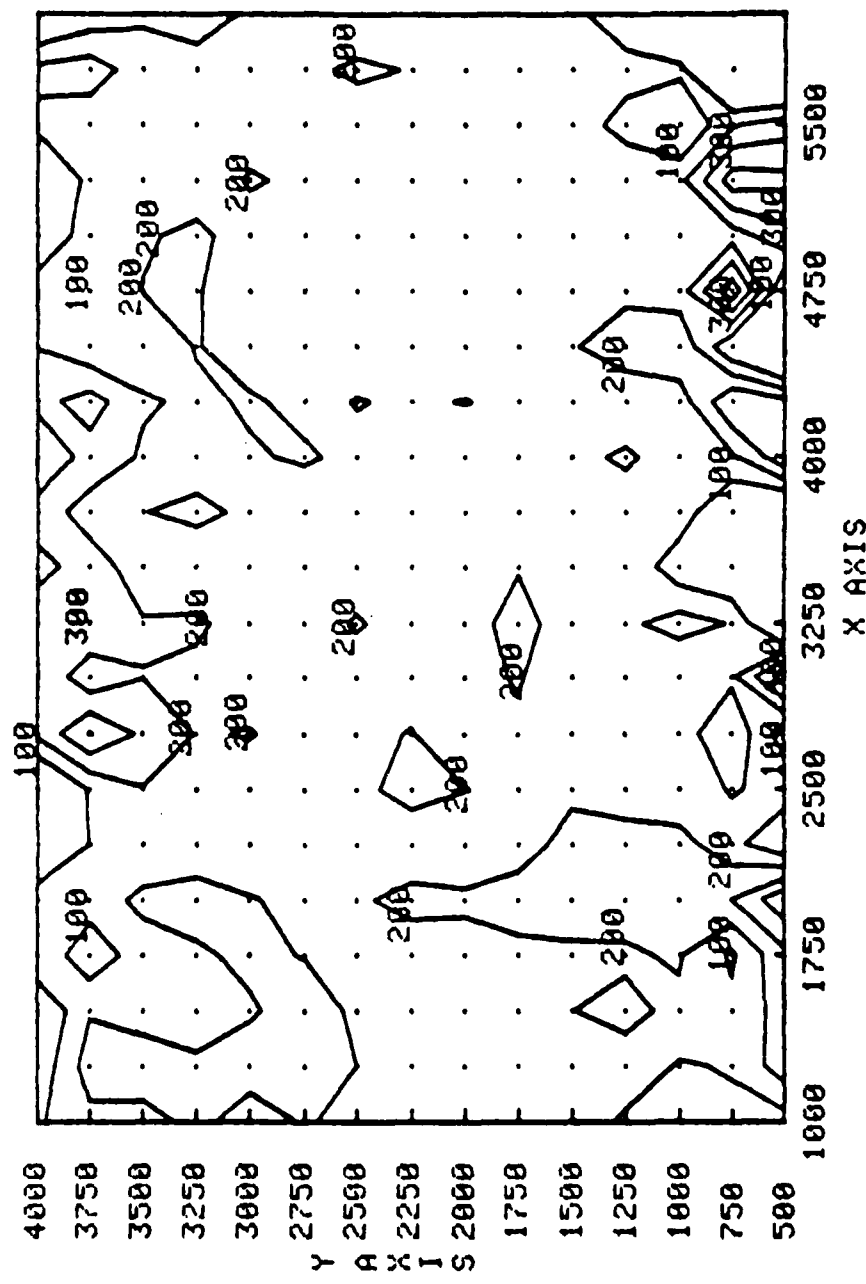


FIG. 50

FIG. 51



$\text{Li}_{40}\text{Be}_2\text{InP}_{2-10-\text{H}}$  100 KeV 5E12 /cm<sup>2</sup> annealed, 8 Urns

L42 62>InP 2-17-H SE14 /cm/cm annulled 3 Urns

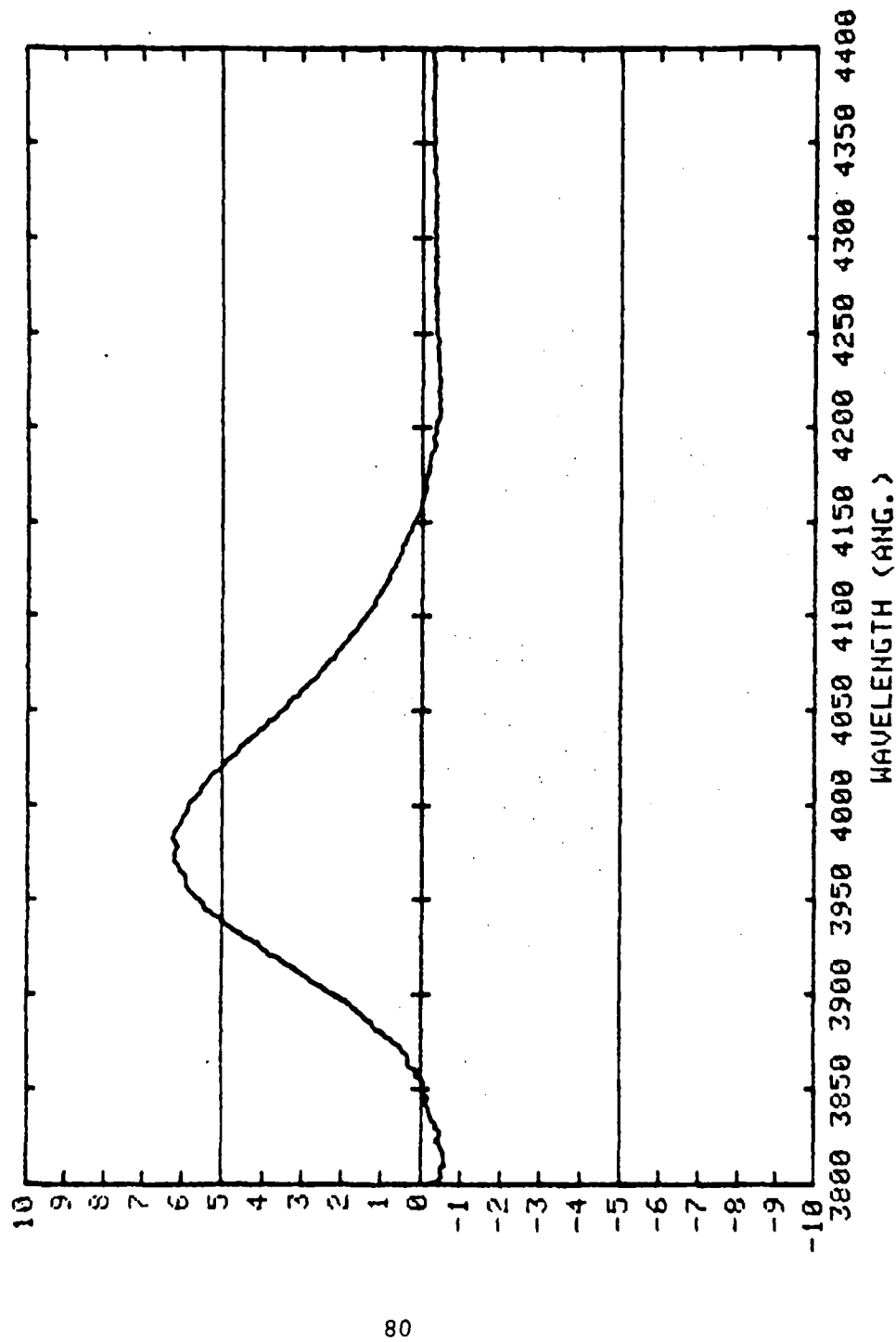


FIG. 52

L42 Be>InP 2-17-H 5E14 /cmcm annealed 8 Vrms

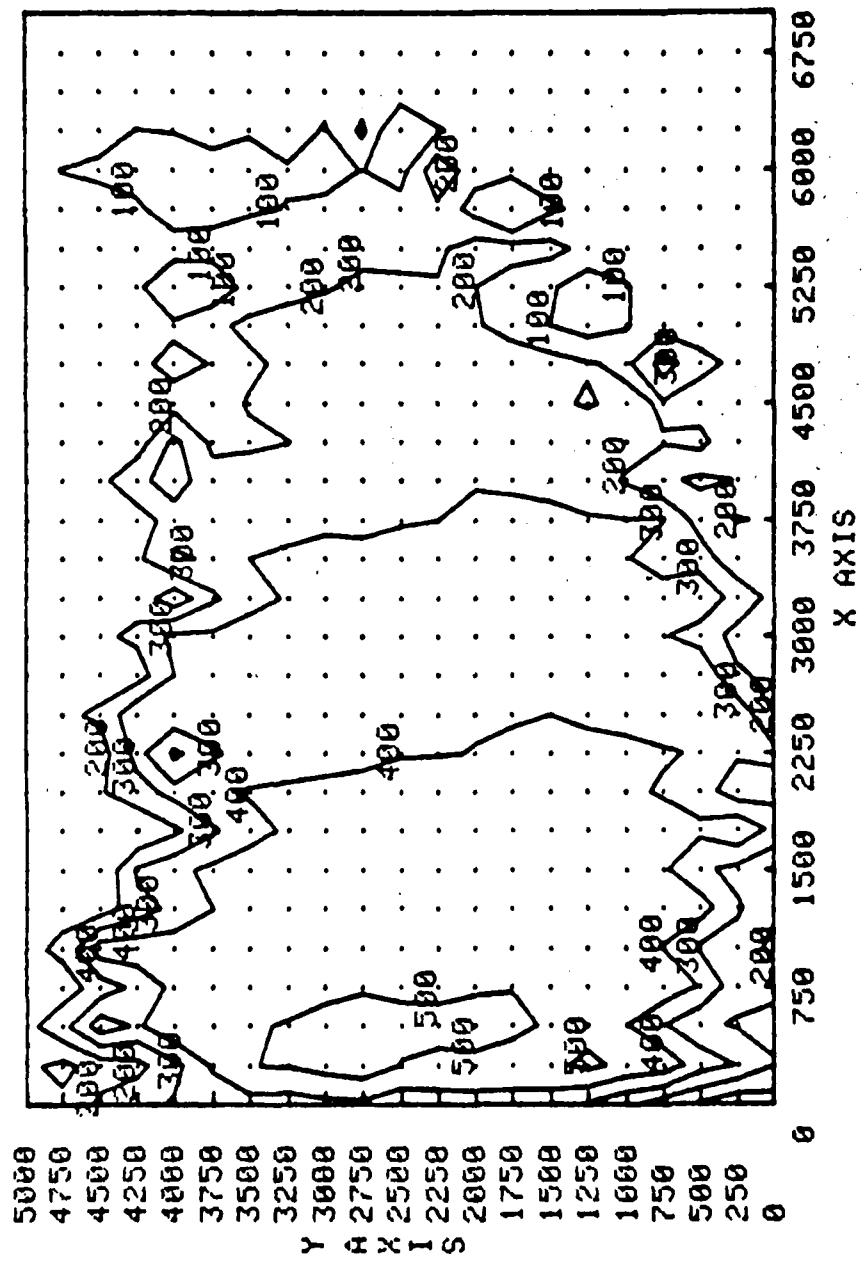


FIG. 53

Figures 54 and 55 respectively for the two samples. In a recent study on this quaternary alloy InGaAsP, Nishino et al.<sup>15</sup> report peaks at 1.07 eV, 1.1 eV, 1.17 eV, 1.25 eV, 1.32 eV, and 1.35 eV. Our present results show peaks at 1.075 eV, 1.1 eV, 2.82 eV, 2.92 eV, and 3.05 eV. The peaks at 1.07 eV and 1.1 eV are in excellent agreement with earlier results.<sup>15</sup> However, our experiments did not show any peak near 1.30 eV for the samples we have studied. The substrate side of our samples did show such a peak as one would expect for InP. Also, since the studies of Nishino et al.,<sup>15</sup> do not extend to such a wide range as we covered, no comparison beyond 1.30 eV region is possible. Also, it is important to point out that in such cases where there are several peaks at different energies, it is possible to probe different depths utilizing the different wavelength maxima. As shown earlier in our studies of GaAs, again this is a decided advantage of the powerful electroreflectance technique in the study of different layers of the semiconducting materials.

As mentioned earlier, the report presented in this section gives the preliminary but significant results that one can use to study in detail the quaternary alloys grown by different methods. It is our hope that in the near future we will have the availability of samples and the opportunity to investigate the different aspects of the implanted InP and the quaternary alloys.

InGaAsP 2-229

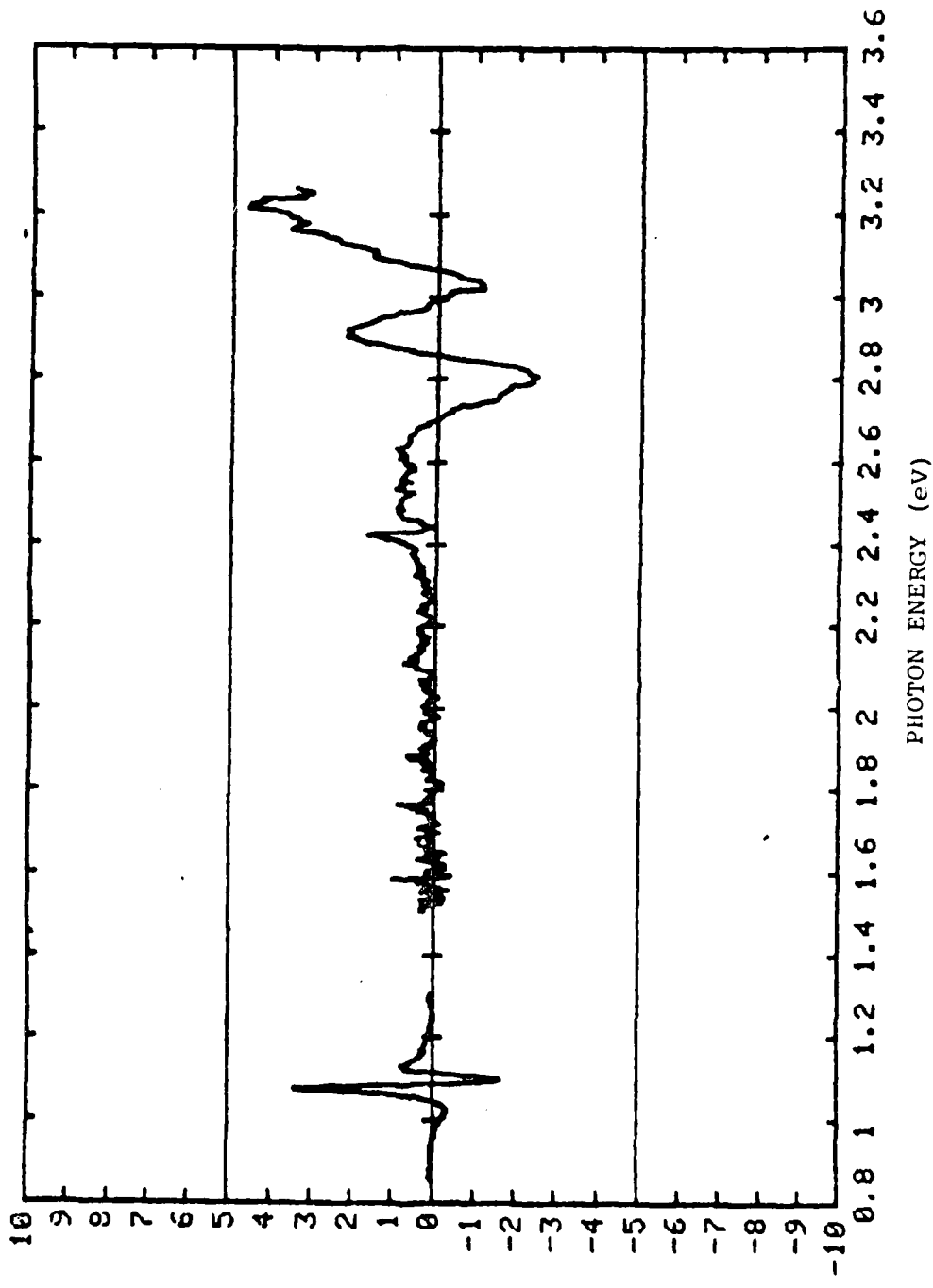
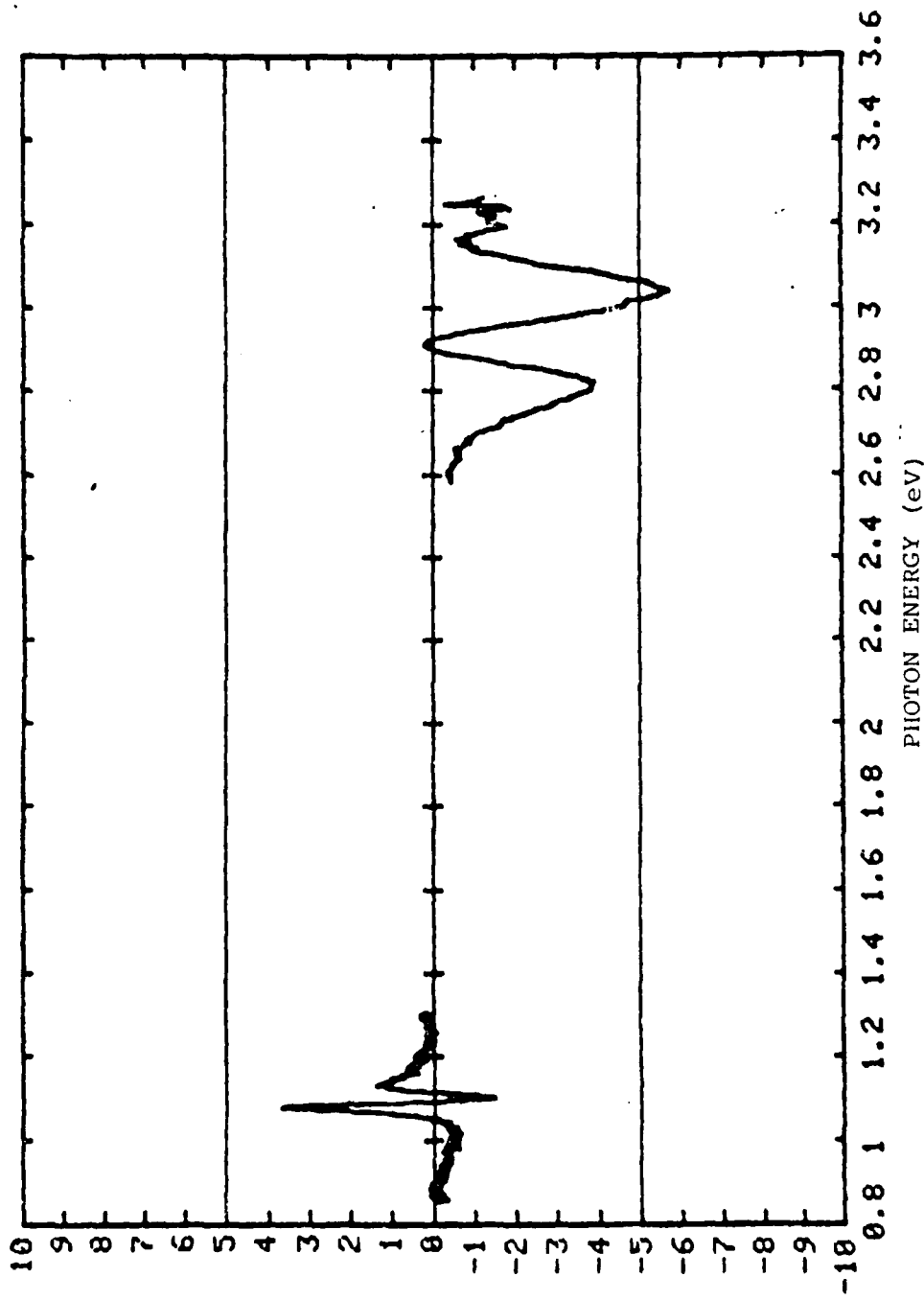


FIG. 54

InGaAsP 2-235



## PART IV

### MODIFIED SCHEMES FOR TOPOGRAPHIC STUDIES

As part of our continuing studies on the topographic examination of III-V semiconductors using electroreflectance and as part of our efforts to improve on the spatial resolution in modulation spectroscopy techniques in general, we have been investigating the possible alternatives to our experimental arrangement. The main aim of considering alternatives is to obtain by suitable modifications a spot size (on the sample to be studied) that can be varied conveniently and easily in the reflectance experiment. This part of the report briefly outlines the results obtained with GaAs and PbSnTe in our on-going studies of electroreflectance of semiconductor systems. It deals with our attempts to reduce the spot size of the incident radiation. As is well known, we can show that with suitable optics, it is only the diffraction limit that will be a major factor. Using laser radiation (instead of the conventional incoherent source), and focussing lens optics, the spot size has been reduced to  $20\mu$  diameter on the sample. With conventional sources and pinholes such a reduction would result in considerable loss of intensity. However, with a laser and a masking arrangement to block the flash lamp light, the beam is first slightly expanded and then reduced in size. Based on the beam size (2mm) and the f-number of the lenses system, it is possible

to reach the limit  $6\mu$  (three times diffraction limit). The present size of  $20\mu$  image (measured by manual stepping of a copper knife edge across the image and monitoring the PM output) can be improved by designing better focussing techniques.

The chief problem in these experiments is the availability of the suitable dye for the wavelength of interest and the sustaining of the chosen dye without degradation as it is pulsed. In order to obtain a convenient time interval for the electroreflectance scan, the dye has to withstand  $\sim 27000$  pulses without significant loss of energy. Our present efforts are directed towards minimizing this time so that the violet 2 dye can be conveniently used at  $E_1$  transition for GaAs. While we have not reached this limit for our sample of GaAs, we had success with PbSnTe sample using the orange 1 dye at  $5700 \text{ \AA}$ .

Figures 56 and 57 show the contour mapping and three-dimensional representations respectively for the sample of PbSnTe using  $100\mu$  spot size and the conventional sources. Spatial parameters for this experiment were  $\sim 3000 \times 3000\mu$  in steps of  $150 \times 150\mu$ . Figures 58 and 59 show the corresponding contours and three dimensional representations for an area approximately  $200 \times 200\mu$  in steps of  $10 \times 10\mu$ . The position is close to that shown in inset in Figure 56. This experiment showed that after twenty minutes (or 18000 pulses) the dye has

FIGURE 56. Effect of standard set-up on tritium-23

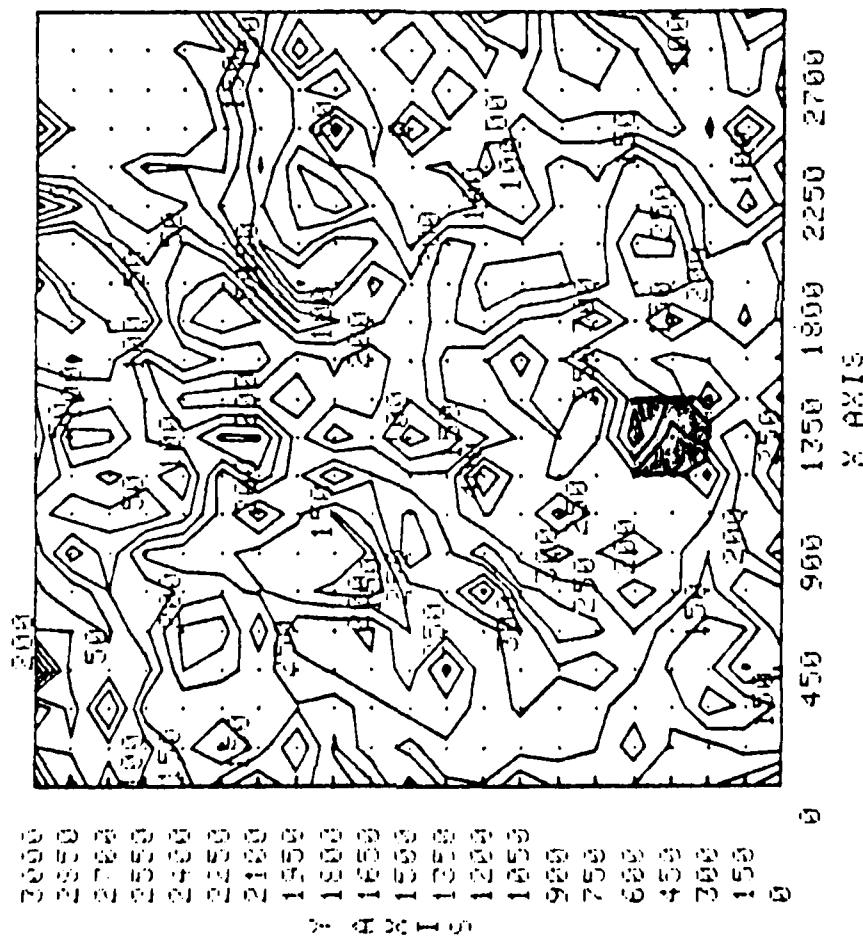


FIG. 56

FIGURE FIGURE standard setup 4 mm 5 12.30

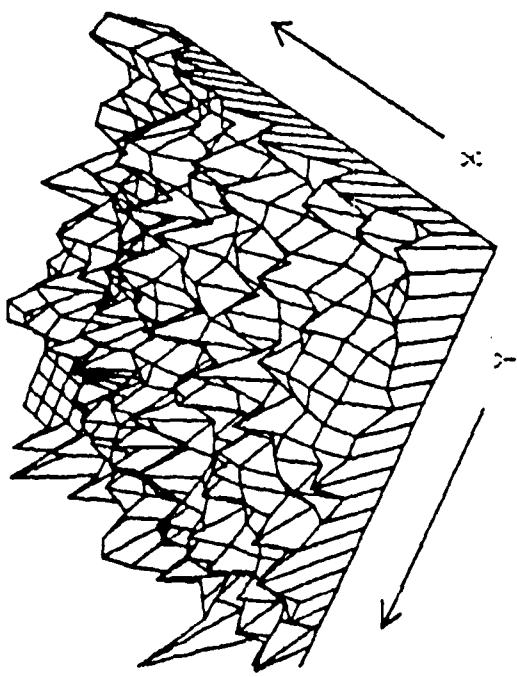


FIG. 57

FIGURE FIFTY-EIGHT      LASER SPOT      GRAYSCALE 1-255      4.0 RMS      5/19/89

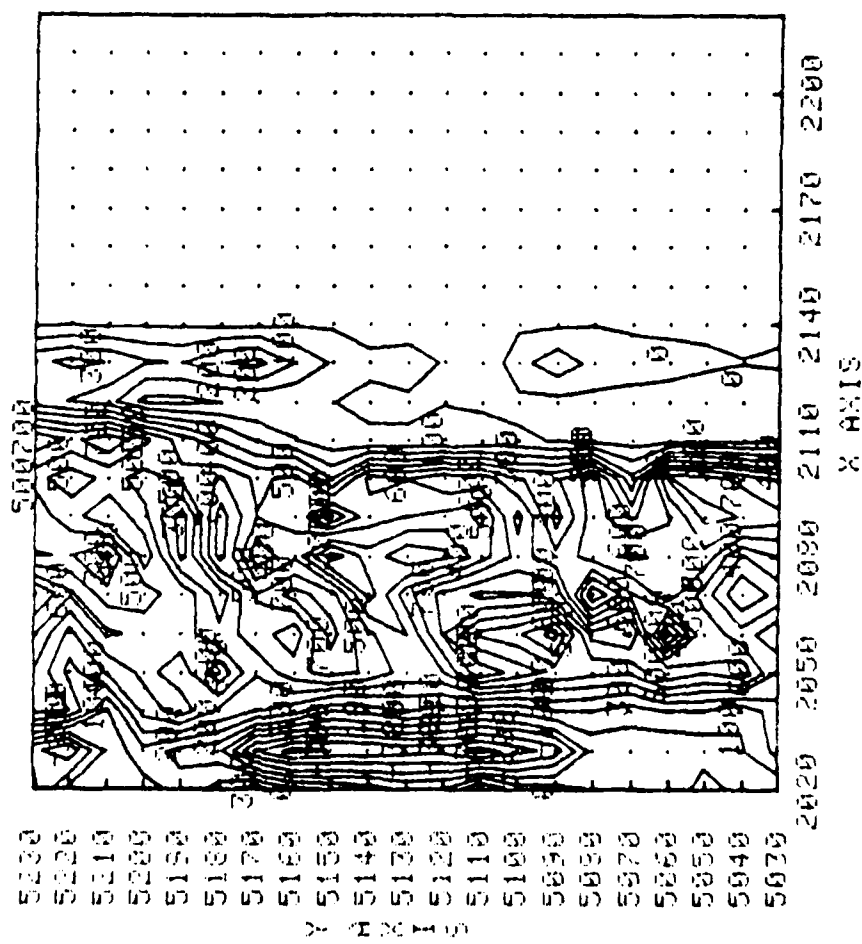


FIG. 58

FIGURE 59  
Laser Effect  
Ground 1 day  
4 hr 12 min 30 sec

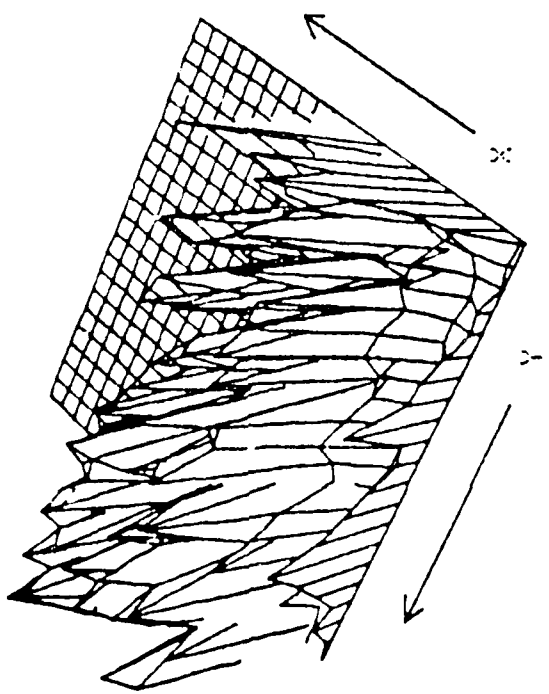


FIG. 59

AD-A094 276

ILLINOIS UNIV AT CHICAGO CIRCLE DEPT OF PHYSICS  
TOPOGRAPHIC EXAMINATION OF SEMICONDUCTOR SYSTEMS. (U)  
NOV 80 S SUNDARAM, P M RACCAH

F/G 20/12

N00014-79-C-809

UNCLASSIFIED

2  
B  
2

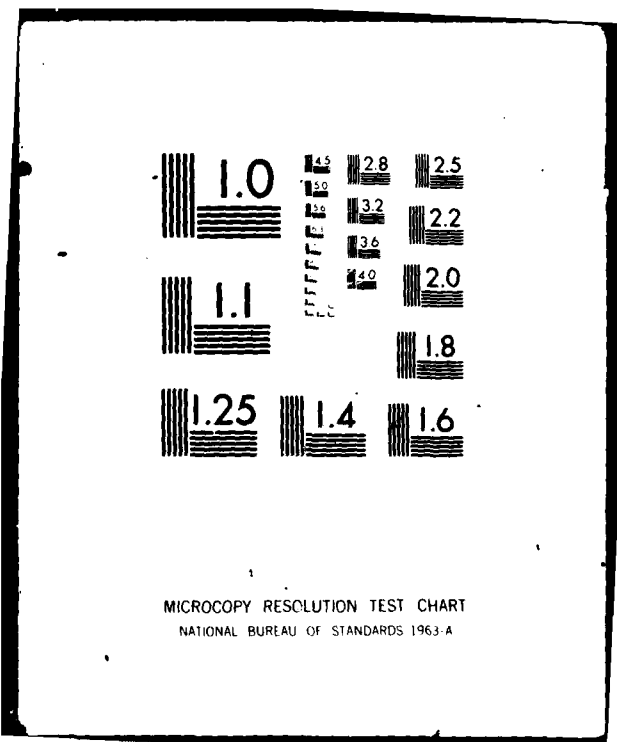
END

DATA

FILED

4-2

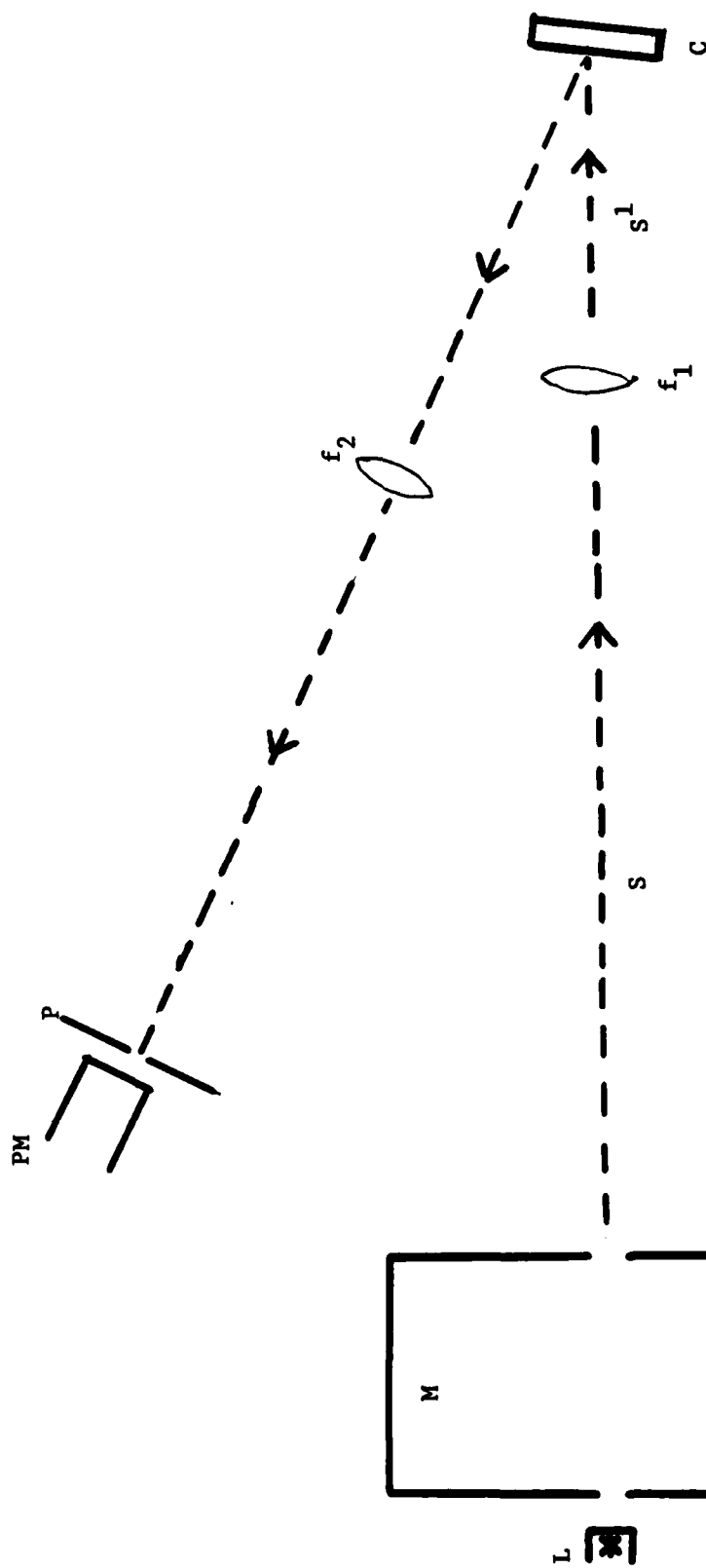
DTIC



proved not usable. However, since this is only a feasibility experiment, we allowed the run to continue so that the effect of noise in the absence of laser pulses can be ascertained. The carrier concentration in relative units has a distribution similar to Figure 56. But more importantly, the comparable three-dimensional representations in the two cases (Figures 57 and 59) establish the feasibility of investigating much smaller spot sizes with laser radiation and appropriate focussing system. Further experiments are continuing to achieve similar results for GaAs.

Two other schemes are also being proposed and planned for our trial runs in our future series of experiments.

The first method is very simple, it merely involves using extremal magnification combinations in the standard optic bench setup, illustrated in Fig. 60. Light is obtained from a tungsten or xenon source (L). The source size however is not the lamp size, but since the light is first collimated and then the wavelength is selected, the source size is determined by the exit aperture of the monochromator (M). This is usually a 1 mm pinhole. The optics with  $f_1$  can reduce this to a source image on the sample of  $S_1/S \approx 1/10$  or  $\approx 100\mu$ . The optics of  $f_2$  refocus this image onto the detector, where the image at the detector will have a size comparable to the original source size (i.e., the incident optics and the reflected light optics are



L-Source, M-Monochromator, C-Sample Cell, P-Pinhole, PM-Detector

FIG. 60

symmetric). The image at the detector is a real image of the sample, as illuminated by the source image. This sample image can be projected on a mask in front of the detector so that the detector can see only part of the illuminated sample area. Resolutions of nearly  $20\mu$  can be achieved. However, the illumination efficiency is significantly reduced by at least a theoretical factor of 25. Either the sample or the detector pinhole may be moved in the experiment to scan the selected sample area.

A more efficient system would be to reduce focal lengths  $f_1$  and  $f_2$  and not mask the sample image. In the standard system, if  $f_1$  or  $f_2$  is reduced, the lens to sample distance imposes severe restrictions on the lens aperture (the two lenses cannot be allowed to block each other). However, supposing the same optics could be used for both incident and reflected light, a different arrangement may be used. This arrangement is represented schematically in Fig. 61 and is suitable for modulation spectroscopy in general (wave length, stress or thermal), particularly for electroreflectance. The design has the following important features:

- (a) high spatial resolution is attainable;
- (b) simultaneously with monitoring reflection, it is possible to visually observe the area under examination;

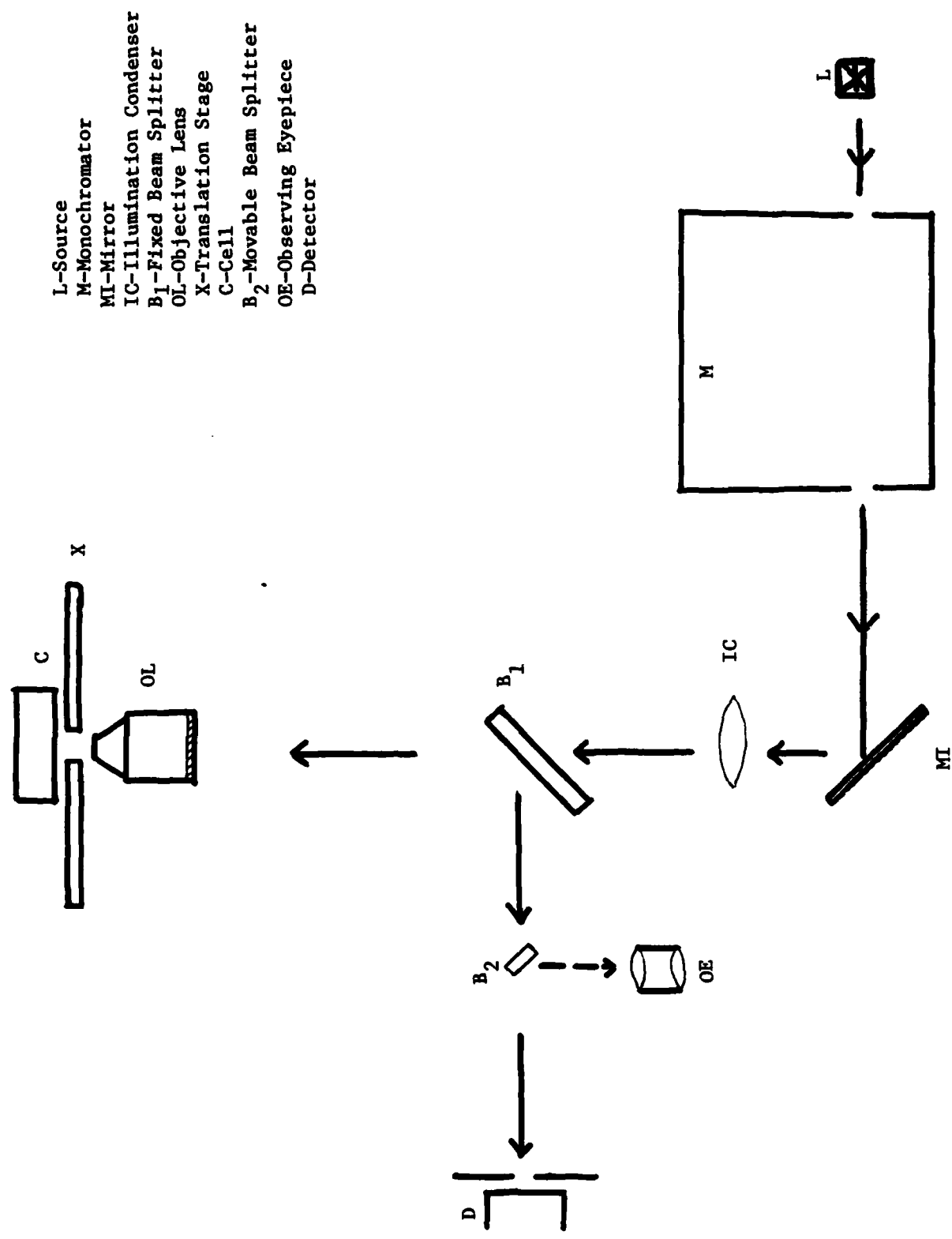


FIG. 61

- (c) it can accept any sample configuration that may be laid upon the translation stage; and
- (d) it can be quite compact.

The system is based on a normal incidence illumination using a metallurgical microscopy objective and directing the light through a beam splitter as shown. The sample stage can be provided with automatic micrometer drives and the sample cell can be held in position with clamps. With a suitable mask in front of the detector and an appropriate diameter for the hole, the needed resolution (of nearly  $5\mu$ ) can be achieved by changing the total optical path of the system (to  $\approx 0.5$  meter). The primary disadvantage of the system is its low f-number. However, this may be offset by choosing a very intense illumination source. It is planned to try this arrangement in our next phase of topographic study on GaAs.

The first method, which has been tested, is to replace the incoherent illumination with a coherent source, a dye laser. In theory this source may be masked to a smaller source size than the incoherent source, primarily as a result of its considerable intensity and also its longer coherence length and collimation. Furthermore, again as a result of the improved source intensity, lower f numbers may be tolerated in the incident beam optics so greater image reduction can be obtained.

In system tested a 1/2 mm pinhole is used to mask the laser beam. A negative lens expands the beam to fill a two lens condenser system which produces a source image of  $\sim 20\mu$ .

## PART V

### CONCLUSIONS

1. Through a systematic study of the electroreflectance of III-V semiconductors of GaAs and InP as well as some other semiconducting materials, we have shown that this modulation technique is a highly sensitive tool for the characterization of the semiconductors.
2. It has been shown that the effects of implantation are strongly related to the implantation energy when annealing is complete and procedures are kept constant.
3. The apparent peak energy shifts in the low field electroreflectance spectra have been interpreted as arising from either the modification of the parabolic band model or due to a definite folding of one of the structures ( $E_1$  or  $E_1 + \Delta_1$ ) with perhaps a third one of probably excitonic origin.
4. The sensitivity of the phase of the electroreflectance spectrum is shown to be most useful for exploring inversion layers.
5. The use of modulation spectroscopy for studies of etched samples and hence for profiling the ion distribution has been established.
6. In addition, the technique is proved to be useful for investigating the quaternary alloys prepared by LPE

and VPE methods and this is significant for further studies of these materials that are of considerable interest for device applications.

#### ACKNOWLEDGMENTS

The authors thank Howard Lessoff and James Comas of the Electronics Technology Division of the Naval Research Laboratory, Washington, D.C. for helpful discussions, for providing all the samples, and for their interest as well as coordination with the present studies. The support of this research by the Naval Research Laboratory under Contracts N00 173-78-C-0437 and N00014-79-C-0809 through the Office of Naval Research is gratefully acknowledged.

TABLE I

Sample Identification	Description	n Values	Max. Shift of $E_1$ (2)
2187	Be $\rightarrow$ GaAs 250 KeV $5 \times 10^{13} \text{ cm}^{-2}$	$n = 7 \times 10^{17} / \text{cm}^3$	+ 20 meV
2186	Be $\rightarrow$ GaAs 250 KeV $2 \times 10^{14} \text{ cm}^{-2}$	$n = 1-2 \times 10^{18} / \text{cm}^3$	+ 30 meV
2185	Be $\rightarrow$ GaAs 250 KeV $1 \times 10^{15} \text{ cm}^{-2}$	$n = 3-4 \times 10^{18} / \text{cm}^3$	+ 80 meV
MBE I <sup>a</sup>	Molecular beam epitaxially		+ 87 meV
MBE II <sup>b,c</sup>	Grown GaAs:Be		+ 60 meV
9127F	Be $\rightarrow$ GaAs 100 KeV $1 \times 10^{13} \text{ cm}^{-2}$		- 20 meV
9127G	Unannealed twin of 9127F		- 20 meV
6-60L Si I	Si $\rightarrow$ GaAs 170 KeV $5 \times 10^{12} \text{ cm}^{-2}$		0 to - 10 meV
6-60L Si II	Si $\rightarrow$ GaAs 170 KeV $5 \times 10^{13} \text{ cm}^{-2}$		+ 64 meV
6-60L Si III	Si $\rightarrow$ GaAs 170 KeV $5 \times 10^{14} \text{ cm}^{-2}$		+ 46 meV
6-60L Be I	Be $\rightarrow$ GaAs 100 KeV $5 \times 10^{12} \text{ cm}^{-2}$	$n = 5 \times 10^{16} / \text{cm}^3$	No shift
6-60L Se I	Se $\rightarrow$ GaAs 400 KeV $5 \times 10^{12} \text{ cm}^{-2}$	$n \sim 10^{16} / \text{cm}^3$	< + 10 meV
6-60L Se II	Se $\rightarrow$ GaAs 400 KeV $5 \times 10^{14} \text{ cm}^{-2}$	$n \sim 10^{18} / \text{cm}^3$	< + 10 meV
LD NCSU	Se $\rightarrow$ GaAs 300 KeV $10^{15} \text{ cm}^{-2}$		+ 64 meV
BC3S	Combination (Be+Se) $\rightarrow$ GaAs; (Se at $1 \times 10^{13} \text{ ions/cm}^2$ Be at $5 \times 10^{12} \text{ ions/cm}^2$ )		+ 10 meV
5 - 9L	Unimplanted reference		No shift
	Sample of GaAs	$n = 5-10 \times 10^{16} / \text{cm}^3$	

<sup>a</sup> Provided by Dr. B. Streetman of University of Illinois

<sup>b</sup> Provided by Dr. D. Covington of Georgia Institute of Technology.

<sup>c</sup> Impurity concentration is  $2.6 \times 10^{18} \text{ cm}^{-3}$ .

Designation	Type	Fluence (cm <sup>-2</sup> )	n (cm <sup>-3</sup> )	E <sub>1</sub> (eV)	Γ <sub>1</sub> (eV)	E <sub>1</sub> + Δ <sub>1</sub>	Γ <sub>Δ</sub>	E <sub>x</sub>	Γ <sub>x</sub>
5-9L	GaAs (Cr T)	-	5 × 10 <sup>16</sup>	2.9261 ±0.0007	0.0806 ±0.0009	3.1632 ±0.0008	0.090 ±0.003	3.025 ±0.003	0.032 ±0.006
2187	GaAs:Be	5 × 10 <sup>13</sup>	7 × 10 <sup>17</sup>	2.9401 ±0.0008	0.103 ±0.002	3.181 ±0.001	0.095 ±0.004	3.05 ±0.01	0.04 ±0.03
2185	GaAs:Be	2 × 10 <sup>14</sup>	1-2 × 10 <sup>18</sup>	2.958 ±0.002	0.102 ±0.002	3.214 ±0.004	0.18 ±0.02	3.02 ±0.01	0.04 ±0.04
2185	GaAs:Be	1 × 10 <sup>15</sup>	3-4 × 10 <sup>18</sup>	2.9665 ±0.0002	0.123 ±0.002	3.199 ±0.002	0.104 ±0.004	2.9723 ±0.0005	0.076 ±0.003
6-60L Be I	GaAs:Be	5 × 10 <sup>12</sup>	5 × 10 <sup>16</sup>	2.9276 ±0.0005	0.061 ±0.001	3.165 ±0.001	0.069 ±0.003	3.1 ±0.2	0.5 ±0.5
6-60L Se I	GaAs:Se	5 × 10 <sup>12</sup>	~10 <sup>16</sup>	2.936 ±0.001	0.097 ±0.002	3.1819 ±0.0009	0.090 ±0.004	3.038 ±0.001	0.056 ±0.004
6-60L Se II	GaAs:Se	5 × 10 <sup>14</sup>	~10 <sup>18</sup>	2.934 ±0.006	0.09 ±0.01	3.160 ±0.006	0.12 ±0.01	3.02 ±0.05	0.09 ±0.09

TABLE II

## REFERENCES

1. M. Cardona, Modulation Spectroscopy, Section III & VII (Supplement II, Solid State Physics, edited by F. Seitz et al., Academic Press, New York, 1969) For electrolyte method see pp. 219-224; for transition energies see p. 244.
2. D.E. Aspnes, Surface Science, 37, 418 (1973).
3. P.E. Vanier, F.H. Pollak, and P.M. Raccah, Applied Optics, 16, 2858 (1977).
4. M. Cardona, K.L. Shaklee, and F.H. Pollak, Phys. Rev. 154, 696 (1967).
5. D.E. Aspnes, Phys. Rev. Letters, 28, 913 (1972).
6. Based on formula for penetration depth  $d = \lambda/2\pi k$ . Values of  $k$  were obtained from B.O. Seraphin and H.E. Bennet, in Semiconductors and Semi-metals. Vol. 3, edited by R.K. Williamson and A.C. Beer, (Academic Press, New York, 1967) Chapter 12. The correct formula  $d = \lambda/2\pi|n + ik|$  will not modify the values appreciably.
7. W.J. Anderson, C.A. Douglas, and Y.S. Park, J. Applied Phys. 46, 3870 (1975).
8. Y.I. Nissim, Stanford University (Private communication).
9. E. Burstein, Phys. Rev. 93, 632 (1954); Ref. 4 pp. 709-10.
10. F. Pollak, (Private communication).
11. D.E. Aspnes and A.A. Studna, Phys. Rev. B, 7, 4605 (1973).
12. K.L. Shaklee, J.E. Rowe, and M. Cardona, Phys. Rev. 174, 828 (1968).
13. M. Chandrapal and F.H. Pollak, Solid State Comm. 18, 1263 (1976).
14. H. Lessoff, (Private communication).
15. T. Nishino, Y. Yamazoe, and Y. Hamakawa, Appl. Phys. Lett. 33, 861 (1978).

#### CAPTIONS FOR FIGURES

Fig. 1. (a) Traditional electrolyte cell arrangement;  
A-quartz cell, B-electrolyte, C-sample, D-wax,  
E-electrode, F-mount, G-platinum electrode.  
(b) Dual cell arrangement; E-hollow palette,  
F-platinum electrode.

Fig. 2. Schematic of Electrolyte Electro Reflectance System.

Fig. 3.  $E_1$  spectrum for an unimplanted sample (5-9L) and an implanted sample (2185).  $E_1$ (1) peak (5-9L) occurs at 2.89 eV,  $E_1$ (2) at 2.96 eV.

Fig. 4.  $\Delta R/R(x,y)$  for unimplanted sample 5-9L. Area scanned is 1 cm x 1 cm. The third axis is the  $\Delta R/R$  amplitude at 2.96 eV, relative units.

Fig. 5.  $\Delta R/R(x,y)$  for sample 2186. Area scanned is 1 cm x 1 cm. The third axis is the  $\Delta R/R$  amplitude in relative units. The sample was not shaped as a square and the flat, zero amplitude regions toward the rear of this plot are regions beyond the edge of the sample.

Fig. 6.  $E(x,y)$  for sample 2186, as described in the text. Base plane is equivalent to 2.90 eV. Scale at  $(x,y = 0,0)$  is approximately 0.1 eV.

Fig. 7.  $E(x,y)$  for sample 2185, as described in the text. Base plane is equivalent to 2.90 eV. Scale at  $(x,y = 0,0)$  is 0.14 eV.

Fig. 8.  $E_1$  spectra of two samples, cut from the same virgin bulk material and implanted with Be in an identical fashion. One sample was subsequently annealed, the other left unannealed.

Fig. 9.  $E_1$  and  $E_1 + \Delta_1$  structure for unimplanted GaAs. The dotted line represents experimental ER data and the solid line is the theoretical fit.

Fig. 10. Modification of "fit" shown in Fig. 9 by incorporating a third lineshape.

Fig. 11. Experimental data (dotted line) and theoretical curve (solid line) for GaAs implanted with Se (fluence  $5 \times 10^{12} \text{ cm}^{-2}$ ).

Fig. 12. The experimental (dotted line) curve of Fig. 11 and theoretical curve (solid line) without the third lineshape, thus displaying the nature of the perturbation.

Fig. 13. Experimental (dotted line) and theoretical curve (solid line) for the sample of GaAs with highest fluence of Be.

Fig. 14. Results for Be implanted GaAs showing energies corresponding to  $E_1$ ,  $E_1 + \Delta_1$ , and the perturbation. Bars are not statistical errors but represent the energy width  $\Gamma$  of the transitions.

Fig. 15.  $\Delta R/R(x,y)$  in relative units for sample 9127G. The amplitude of  $\Delta R/R$  in the center of the crater is inverted to that at the edges.

Fig. 16.  $\Delta R/R(\lambda)$  at three collinear points along the surface of sample 9127F. The amplitude of  $\Delta R/R$  is found to decrease to zero as the examined region is moved along the sample, then increase again reversed in phase. (Phase in this context refers to the phase of  $\Delta R/R$  vs  $\lambda$ , not the phase of the electrical field applied to the surface which is independent of position.)

Fig. 17.  $E_0$  and  $E_1$  spectra of sample BC3S and 5-9L. Note the change in phase between the  $E_1$  signals and the  $E_0$ .

Fig. 18. Topographic scan of unetched GaAs:Be.

Fig. 19.  $\Delta R/R$  for unetched GaAs:Be.

Fig. 20. Contour diagram for GaAs:Be with 1550  $\text{\AA}$  etch step.

Fig. 21.  $\Delta R/R$  for GaAs:Be with 1550  $\text{\AA}$  etch step.

Fig. 22. Contour diagram for GaAs:Be with 4250  $\text{\AA}$  etch step.

Fig. 23.  $\Delta R/R$  for GaAs:Be with 4250  $\text{\AA}$  etch step.

Fig. 24. Contour diagram for GaAs:Be with 6300  $\text{\AA}$  etch step.

Fig. 25.  $\Delta R/R$  for GaAs:Be with 6300  $\text{\AA}$  etch step.

Fig. 26.  $\Delta R/R$  for GaAs:Be with 6300  $\text{\AA}$  etch step (rotated by 90° from Fig. 25).

Fig. 27. Contour diagram for GaAs:Be with 10750  $\text{\AA}$  step.

Fig. 28.  $\Delta R/R$  for GaAs:Be with 10750  $\text{\AA}$  step.

Fig. 29. Contour diagram for GaAs:Be with 13500  $\text{\AA}$  step.

Fig. 30.  $\Delta R/R$  for GaAs:Be with 13500  $\text{\AA}$  step.

Fig. 31.  $\Delta R/R$  for GaAs:Be with 13500  $\text{\AA}$  step (rotated by 180° from Fig. 30).

Fig. 32. Spectrum for Point 1 on GaAs:Be sample with 3000 Å etch step.

Fig. 33. Spectrum for Point 2 on GaAs:Be sample with 3000 Å etch step.

Fig. 34. Topographical scan for GaAs:Be sample with 3000 Å etch step.

Fig. 35.  $E_1$  zero crossing for GaAs:Be sample with 3000 Å etch step.

Fig. 36. Spectrum for Point 1 on GaAs:Be with 8500 Å etch step.

Fig. 37. Spectrum for Point 2 on GaAs:Be with 8500 Å etch step.

Fig. 38.  $E_1$  zero crossing for GaAs:Be with 8500 Å etch step.

Fig. 39. Spectrum for GaAs:Be with 14000 Å etch step.

Fig. 40. Contour diagram for GaAs:Be with 14000 Å etch step.

Fig. 41.  $E_1$  zero crossing for GaAs:Be with 14000 Å etch step.

Fig. 42. Spectrum for GaAs:Se.

Fig. 43. Contour diagram for GaAs:Se.

Fig. 44. Spectrum of InP (1-81-H) for the near IR region, a PbS detector was used with a consequent increase in noise.

Fig. 45. Expanded near UV spectrum of the InP (1-81-H).

Fig. 46.  $\Delta R/R(x,y)$  for InP (1-81-H). X,Y step size was 500 microns.

Fig. 47. Spectrum of InP(Sn,Fe) (2-13-H). Additional filtering

prior to the PbS detector has greatly improved S/N ratio from that of Fig. 44.

Fig. 48. Spectrum of InP:Si implanted and annealed sample ( $5 \times 10^{14}$  ions/cm<sup>2</sup> fluence).

Fig. 49. Topographic scan for InP:Si sample.

Fig. 50. Spectrum of InP:Be annealed sample (2-10-H).

Fig. 51. Contour diagram of InP:Be sample (2-10-H).

Fig. 52. Spectrum of InP:Be annealed sample (2-17-H).

Fig. 53. Contour diagram of InP:Be annealed sample (2-17-H).

Fig. 54. Spectrum of a quaternary sample, InGaAsP (2-229).

Fig. 55. Spectrum of a quaternary sample, InGaAsP (2-235).

Fig. 56. Contour diagram for PbSnTe/PbTe using conventional source.

Fig. 57. Three dimensional representation for PbSnTe/PbTe using conventional source.

Fig. 58. Contour diagram for PbSnTe/PbTe using pulse laser.

Fig. 59. Three dimensional representation for PbSnTe/PbTe using pulse laser.

Fig. 60. Modified optics for increased spatial resolution.

Fig. 61. Modified scheme for modulation spectroscopy in general.

DISTRIBUTION LIST FOR CONTRACTS:

Mr. Hunter Chilton  
RADC/OCTE  
Griffiss AFB  
NY 13441

Mr. Lothar Wandinger  
ECOM/AMSEL/TL/IJ  
Fort Monmouth, NH 07703

Dr. Harry Wieder  
Naval Ocean Systems Center  
Code 922  
271 Catalina Blvd.  
San Diego, CA 92152

Dr. John Kennedy  
RADC/ESM  
Hanscom AFB  
MA 01731

Dr. C. Sabagian  
RADC/ETSP  
Hanscom AFB  
MA 01731

Mr. Don Reynolds  
AFAL/DHR  
Wright-Patterson AFB  
OH 45433

Mr. Max Yoder  
Office of Naval Research  
Code 427  
800 North Quincy St.  
Arlington, VA 22217

Dr. L. Cooper  
Office of Naval Research  
Code 427  
800 North Quincy St.  
Arlington, VA 22217

Mr. J. W. Willis  
Naval Air Systems Command  
Washington, DC 20361

Dr. J. Dimmock  
Office of Naval Research  
Code 427  
800 North Quincy St.  
Arlington, VA 22217

Dr. Y. S. Parks  
AFAL/DHR  
Wright-Patterson AFB  
OH 45433

Dr. George Gamota  
Staff Specialist for Research  
OUSDRE, Room 3D1067  
Pentagon  
Washington, DC 20301

Dr. L. Sumney  
Office of the Director of Defense  
Research & Engineering  
Washington, DC 20301

Dr. R. Reynolds  
Advanced Research Project Agency  
1400 Wilson Blvd.  
Arlington, VA 22209

Dr. L. C. Kravitz  
Director of Electronic & Solid State  
Sciences (223)  
Air Force Office of Scientific Research  
Bldg. 410  
Bolling Air Force Base  
Washington, DC 20332

Mr. Nathan Butler  
Naval Electronic Systems Command  
Washington, DC 20361

Mr. J. Cauffman  
Naval Electronic Systems Command  
Washington, DC 20360

Dr. A. Clista  
Naval Air Systems Command  
Washington, DC 20361

**Dr. A. D. Klein**  
Naval Air Systems Command  
Washington, DC 20361

**Dr. H. J. Mueller**  
Naval Air Systems Command  
Washington, DC 20361

**Dr. Thomas AuCoin**  
USAECOM  
DRSEL-TL-ESG  
Fort Monmouth, NJ 07703

**Dr. H. Whitman**  
U.S. Army Research Office  
P.O. Box 12211  
Research Triangle Park  
Raleigh, NC 27709

**Dr. H. R. Riedl**  
Naval Surface Weapon Center  
Code WR-34  
White Oak, Silver Spring, MD 20910

**Dr. F. Barbe**  
Department of Navy  
Office of ASNRES  
Room 5E787  
Pentagon  
Washington, DC 20350

**Dr. Robert Pohanka**  
Office of Naval Research  
BCT#1 (619)  
800 North Quincy St.  
Arlington, VA 22217

**Dr. E. Teppo**  
Naval Weapons Center  
China Lake, CA 93555

**Dr. Guenther H. Winkler**  
Code 381  
Naval Weapons Center  
China Lake, CA 93555

**Mr. William Gutierrez**  
Night Vision & Electro Optics Lab.  
Fort Belvoir, VA 22060

**Dr. George Wright**  
Office of Naval Research  
Code 427  
Arlington, VA 22217

**Dr. Fred Rothwarf**  
U.S. Army Electronic Technology &  
Devices Lab. ERADCOM  
Ft. Monmouth, NJ 07703

**Advisory Group on Electron Devices**  
201 Varick St.  
New York, NY 10014

**Defense Documentation Center**  
Cameron Station  
Alexandria, VA 22314

**Mr. M. Siegmann**  
Code 6804  
Naval Research Laboratory  
Washington, DC 20375

**NRL: (Standard Distribution List)**  
Code 6800, 6802, 6803, 6810, 6820,  
6850, 6870, 6890

**Distribution List**

**Dr. L. Sumney**  
OUSDR&E 3D1079  
Pentagon  
Washington, DC 20301

**Dr. Andy Glista**  
Naval Air Systems Command  
Washington, DC 20361

**Mr. J.W. Willis**  
Naval Air Systems Command  
Washington, DC 20361

**Dr. A.D. Klein**  
Naval Air Systems Command  
Washington, DC 20361

**Dr. H.J. Mueller**  
Naval Air Systems Command  
Washington, DC 20361

**Dr. Thomas AuCoin**  
USAECOM  
DRSEL-TL-ESG  
Fort Monmouth, NJ 07703

**Dr. H. Whitman**  
U.S. Army Research Office  
PO Box 12211  
Research Triangle Park  
Raleigh, NC 27709

**Mr. M. Siegmann**  
NAVMAT, Code 0343  
Crystal Plaza 5; Room 1044  
Washington, DC 20360

**Dr. H.R. Riedl**  
Naval Surface Weapons Center  
Code WR-34  
White Oak, Silver Spring, MD 20910

**Max Swerdlow (2 copies)**  
AFOSR/NE, Bldg. 410, Rm. C-213  
Bolling Air Force Base  
Washington, DC 20332

**Defense Documentation Center**

**Advisory Group on Electron Devices**

**NRS (standard distribution list) +**  
Code 6800, 6801, 6803, 6000,  
6810,  
6820 (10 copies)  
6830  
6850  
6870  
5280  
6890

Mr. Hunter Chilton  
RADC/OCTE  
Griffiss AFB  
NY 13441

Mr. Lothar Wandinger  
ECOM/AMSEL/TL/IJ  
Fort Monmouth, NJ 07703

Mr. Harry Wieder  
Naval Ocean Systems Center  
Code 922  
271 Catalina Blvd  
San Diego, CA 92152

Mrs. Elizabeth Tarrants  
AFML/LTE  
Wright-Patterson AFB  
OH 45433

Mr. S.A. Roosild  
RADC  
L.G. Hanscom AFB  
Bedford, MA 01731

Dr. John Kennedy  
RADC/ETSP  
Hanscom AFB  
MA 01731

Dr. C. Sahagian  
RADC/ETSP  
Hanscom AFB  
MA 01731

Mr. Don Reynolds  
AFAL/DHR  
Wright-Patterson AFB  
OH 45433

Mr. Max Yoder  
Office of Naval Research  
Code 427  
800 North Quincy St.  
Arlington, VA 22217

Dr. L. Cooper  
Office of Naval Research  
Code 427  
800 North Quincy St.  
Arlington, VA 22217

Dr. J. Dimmock  
Office of Naval Research  
Code 427  
800 North Quincy St.  
Arlington, VA 22217

Dr. Y.S. Parks  
AFAL/DHR  
Wright-Patterson AFB  
OH 45433

Chief of Naval Material  
Code 0343  
Washington, DC 20360

Dr. George Gamota  
Staff Specialist for Research  
OUSDRE, Room 3D1079  
Pentagon  
Washington, DC 20301

Dr. L. Weisberg  
OUSDRE  
Pentagon  
Washington, DC 20301

Dr. R. Reynolds  
Advanced Research Project Agency  
1400 Wilson Blvd  
Arlington, VA 22209

Dr. L.C. Kravitz  
Director of Electronic & Solid  
State Sciences (223)  
Air Force Office of  
Scientific Research, Bldg. 410  
Bolling Air Force Base  
Washington, DC 20332

Mr. Nathan Butler  
Naval Electronic Systems Command  
Washington, DC 20360

DA  
FILM